EXPERIMENTAL AND COMPUTATIONAL INVESTIGATION OF THE CONFORMAL VORTEX GENERATOR

By

GEOFFREY A. KIBBLE

BACHELORS OF SCIENCE IN AEROSPACE ENGINEERING
Oklahoma State University
Stillwater, Ok
2015

BACHELORS OF SCIENCE IN MECHANICAL ENGINEERING
Oklahoma State University
Stillwater, Ok
2015

Submitted to the Faculty of the
Graduate College of
Oklahoma State University
in partial fulfillment of
the requirements for
the Degree of
MASTER OF SCIENCE
AUGUST, 2017

EXPERIMENTAL AND COMPUTATIONAL INVESTIGATION OF THE CONFORMAL VORTEX GENERATOR

Thesis Approved:

Dr. Jamey Jacob

Thesis Advisor

Dr. Brian Elbing

Dr. Arvind Santhanakrishnan

Dedicated to

my beautiful wife Brooke,

whose energy, faith, and sacrificial care

brings forth laughter, rootedness, and love.

ACKNOWLEDGEMENTS

This work was funded in part by Edge Aerodynmix. A significant portion of the computing for this project was performed at the OSU High Performance Computing Center at Oklahoma State University, supported in part through the National Science Foundation grant OCI1126330. I would like to thank the faculty professors Jamey Jacob, Brian Elbing, and Arron Alexander, who guided the direction of the research, discussed results, and always found time to provide instruction on difficult material. I would like to thank Chris Petrin, who was instrumental in conducting and supporting the experimental work presented. I would also like to acknowledge the undergraduate research team members who carried out portions of the required groundwork. I would like to thank my parents, Sean and Kim, who consistently supported my academic endeavors and challenged me to pursue excellence. Also I would like to thank my Grandparents whose prayers and support were required to accomplish the work presented. Finally, I would like to recognize my mentors Emily Snow, Kay Porter, and Fara Williams who genuinely cared about my future and pushed me to succeed.

Name: Geoffrey A. Kibble

Date of Degree: AUGUST, 2017

Title of Study: EXPERIMENTAL AND COMPUTATIONAL INVESTIGATION OF THE CONFORMAL VORTEX GENERATOR

Major Field: Mechanical and Aerospace Engineering

Passive flow control devices, such as vortex generators or riblets, have limited applications and often provide benefits with the expense of drag or increased cost. Many flow control methods have come and gone due to the lack of practical applications. The Edge Aerodynamix Conformal Vortex Generator (CVG) is different than these previous devices because it has been shown to drastically reduce fuel consumption in transport category aircraft without noticeable adverse side effects. Therefore, this investigation of the CVG device, which will lead to future evaluation and characterization of its leveraged drag mechanism, sought to produce an appropriate scaling relationship for the CVG, reproduce experimental flight test results computationally, and study the properties of the flow at the CVG device.

Experimental work was accomplished with water and wind tunnel facilities utilizing flow visualization and particle velocimetry (PIV) flow field measurements. Computational work was accomplished with STAR-CCM+ commercial CFD software and Pointwise grid software. Experimental and computational studies evaluated multiple scaling approaches and found that the CVG device is sensitive to geometrical and boundary layer properties. Computational simulation results reproduced wall shear stress patterns observed in Edge Aerodynamix flight tests. 2D flow simulations over specific airfoil sections, which correspond to Edge Aerodynamix flight test vehicles, were produced to provide flow boundary layer properties at the CVG device. The transonic shock oscillating behavior was investigated through visualization videos during fuel consumption flight tests, which suggested that the CVG device may dampen high-frequency shock oscillations; and therefore, could account for significant drag reduction. This work was limited by the lack of an adequate experimental scaling relationship and subsequent experimental results for CFD validation. However, a scaling approach was identified for future experimental testing. Additionally, the computational work was limited by the turbulence model used and the lower-order discretization schemes employed, and therefore, future work should build upon the recommendations presented. The work accomplished will lead to further scaling development and ultimately the evaluation and characterization of the CVG drag device.

Contents

List of Tables

List of Figures

NOMENCLATURE

Geometric Properties

A	Area
AoA	Angle of Attack
c	Speed of sound
C	Chord
δ or δ_{99}	Boundary layer thickness (99 percent of freestream)
δ^*	Displacement thickness
Δx	Cell length in the x-distance
Δy	Cell length in the y-distance
Δz	Cell length in the z-distance
H	Step height
L	CVG triangular height (or length)
l	Length
V	Cell volume
W	CVG triangular width
x	x-distance or location
X	Distance to CVG
y	y-distance or location
z	z-distance or location

Fluid and Flow Properties

alt.	Altitude
C^+	Law of the wall, log-law y-intercept

dy	Incremental x-distance
dy	Incremental y-distance
dz	Incremental z-distance
Δt	Change in time or time step
e	Internal energy
F_b	Body force
F_L	Lift force
F_D	Drag force
g	Gravity
κ	Von Karman constant
l_ν	Viscous wall-unit
μ	Dynamic viscosity
μ_ν	Bulk viscosity
μ_t	Turbulent viscosity
ν	Kinematic viscosity
ν_t	Turbulent kinematic viscosity
p	Pressure
p_∞	Freestream pressure
q	Heat flow
ρ	Density
S	Strain rate tensor
t	Time
T	Temperature
θ	Momentum thickness
τ	Shear stress
τ_w	Wall shear stress
$\vec{u}$	Velocity vector

u	Velocity in the x-direction
u_τ	Friction velocity
U_∞	Freestream velocity
v	Velocity in the y-direction
ω	Vorticity
Ω	Frequency

Statistics

T_τ	Reynolds stress tensor
u'	Zero mean velocity in the x-direction
U	Average velocity in the x-direction
v'	Zero mean velocity in the y-direction
V	Average velocity in the y-direction
w'	Zero mean velocity in the z-direction

Dimensionless Parameters

C_f	Coefficient of friction
C_D	Coefficient of drag
C_L	Coefficient of lift
C_p	Coefficient of pressure
Fr	Froude number
g^*	Dimensionless gravity
$\nabla*$	Dimensionless gradient, divergence, or curl operator
p^*	Dimensionless pressure
π_n	Pi-term
Re	Reynolds number
Re_x	Reynolds number based on x-distance
Re_X	Reynolds number based on CVG x-location
Re_C	Reynolds number based on chord

Re_H	Reynolds number based on CVG step height
Re_δ	Reynolds number based on boundary layer thickness
Re_{δ^*}	Reynolds number based on displacement thickness
Re_θ	Reynolds number based on momentum thickness
Re_τ	Reynolds number based on friction velocity
St	Strouhal number
t^*	Dimensionless time
u^+	Dimensionless velocity
$\vec{u}^*$	Dimensionless velocity vector
x^+	Dimensionless x-distance scaled to viscous wall-unit
y^+	Dimensionless x-distance scaled to viscous wall-unit
z^+	Dimensionless x-distance scaled to viscous wall-unit

RANS SST K-Omega Model

a	Model coefficient
α^*	Model coefficient
α_1^*	Model coefficient
α_2^*	Model coefficient
β	Coefficient of thermal expansion
β_1	Coefficient of thermal expansion
β_2	Coefficient of thermal expansion
β^*	Model coefficient
β_1^*	Model coefficient
β_2^*	Model coefficient
C_T	Model coefficient
$C_{\epsilon 1}$	Model coefficient
$C_{\epsilon 2}$	Model coefficient
$CD_{k\omega}$	Cross-diffusion coefficient

d	Distance to the wall
D_ω	Cross-diffusion term
f_{β^*}	Free-shear modification factor
f_β	Vortex-stretching modification factor
f_c	Curvature correction factor
F_1	Model blending function
F_1	Model blending function
G_k	Turbulent production
G_{nl}	"Non-linear" production
G_b	Buoyancy production
G_ω	Specific dissipation production
γ	Model coefficient
γ_1	Model coefficient
γ_2	Model coefficient
k	kinetic energy
k_0	Ambient turbulence value that counteracts turbulence decay
κ	Model coefficient
$\overline{p}$	Average pressure
Pr_t	turbulent Prandtl number
P_k	Production term
P_ω	Production term
S_k	User-specified source term
S_ω	User-specified source term
σ_k	Model coefficient
σ_{k1}	Model coefficient
σ_{k2}	Model coefficient
σ_ω	Model coefficient

$\sigma_{\omega 1}$	Model coefficient
$\sigma_{\omega 2}$	Model coefficient
T_τ^{RANS}	Reynolds stress tensor (from reynolds averaging)
T_t	Turbulent time scale
$\overline{T}$	Average temperature
$T_{t,NL}$	Non-linear constitutive relation
$\overline{u}$	Average velocity
ω	specific dissipation rate
ω_0	Ambient turbulence value that counteracts turbulence decay

LES Dynamic Smagorinsky SGS Model

C_s	Model coefficient
Δ	Length scale or grid filter width
G	Filter function
k	Subgrid scale turbulent kinetic energy
$\tilde{L}$	Grid filter length
$\widehat{L}/\tilde{L}$	Model coefficient
L	Model tensor
M	Model tensor
$\tilde{u}$	Filtered velocity
Q	Solution variable
$\tilde{Q}$	Filtered value
Q'	Sub-filtered, or sub-grid, value
$\widehat{\tilde{Q}}$	Test-filtered value
T_τ^{LES}	Filtered Reynolds stress tensor (from LES filtering)
$\tilde{u}$	Filtered velocity
$\widehat{\tilde{u}}$	Test-filtered velocity
x'	Filtered length

IDDES RANS SST K-Omega Model

α	Model coefficient
C_{DES}	Model coefficient
C_{dt}	Model coefficient
C_l	Model coefficient
C_t	Model coefficient
Δ_{IDDES}	Altered mesh length scale
Δ_{min}	Smallest distance between the cell center and neighboring cell centers
f_B	Blending function
$\tilde{f}_d$	Model coefficient
f_{dt}	Model coefficient
f_Δ	damping function
f_e	Elevating function
f_{e1}	Model coefficient
f_{e2}	Model coefficient
f_l	Model coefficient
f_t	Model coefficient
l_{HYBRID}	Hybrid length-scale
l_k	Turbulent length-scale
$\breve{p}$	Blended (filtered to averaged) pressure
ψ	Low-Reynolds number correction function
r_{dt}	Model coefficient
r_{dl}	Model coefficient
$T_\tau^{Modeled}$	Blended Reynolds stress tensor (from DES blending)
$\breve{u}$	Blended (filtered to averaged) velocity
$\tilde{\omega}$	Specific dissipation rate for the IDDES formulation

General Terms

IA_1	Interrogation area 1
IA_2	Interrogation area 2
n	Value of a set
N	Total number of a set
$max()$	Take the largest of the values in the parentheses
$min()$	Take the smallest of the values in the parentheses
$_m$	Modeled value
$_p$	Full scale value
$\phi()$	Function of

Chapter 1

Introduction

Numerous flow control devices have been studied and implemented on wings over a period of years with success due to marginal improvements. Whether active or passive devices are used, their aerodynamic advantages are often comparable to the disadvantages they create. Consequently, control devices are generally of value over a narrow operation range. The classic example is the traditional vortex generator, which increases lift and stall angle-of-attack at the cost of increased parasite drag as shown in 1.3. An active flow control example is wing surface suction, which improves separation characteristics while increasing wing design complexity and ultimately weight [1]. More recent flow control devices, such as riblets, have shown drag reduction without adverse side effects. However, riblets require the entire top surface of the wing to be refinished with micro grooves, and they still have unresolved obstacles to practical application [2]. Consequently, devices like these have come and gone because of small profit margins in cost-to-benefit analyses when all additional costs are considered. In contrast, a thin device that may be readily applied to any flight surface without modification, may significantly reduce fuel costs, and thus provide a noticeable aerodynamic advantage.

1.1 Background

Edge Aerodynamix's Conformal Vortex Generators, or CVG, are a new passive drag reduction technology currently available for the Boeing 737 aircraft, with more applications in development. The CVG is essentially a small scale geometrical modification

to the flow's boundary surface, which interacts with the boundary layer to reduce drag. This CVG technology was originally developed as an attempt to reduce efficiency losses associated with applying protective leading edge tape to helicopter rotor blades. Erosion of helicopter blades has been studied extensively by the military ([3], [4], and [5]), and protection methods such as sacrificial tapes and coatings have been considered as possible solutions [6]. Protective tapes, coatings, or sacrificial layers do present a significant issue where the protective material and the airfoil surface meet, which produces a relatively small step between them. For example, the backward-facing step produced by a 0.36 mm protective rubber tape on the EC135 rotor blade resulted in early transition, as shown in Figure 1.1, which is not ideal for the airfoil design [7]. A computational study [8] found that helicopter erosion coatings can cause a significant increase to the profile drag. Therefore, the CVG was originally designed as a helicopter blade erosion protection tape that did not result in significant losses, as seen with other erosion protection methods. The difference between the CVG and traditional leading edge protection was the trailing edge of the tape, which had a unique serrated pattern instead of a conventional backward-facing step. This new design provided a leading edge protection without the losses and opened the door to fixed-wing aircraft application.

1.2 Motivation

Field tests have shown that CVG have been shown to increase the efficiency of the Robinson R-22 helicopter, Lear 24B, and Boing 737-500 flight test platforms. Specifically, the Boeing 737-500 saw fuel savings of as much as 6 percent with the CVG applied [9]. This is incredibly significant because, at six percent fuel savings, a single airline utilizing the CVG technology could save hundreds of millions of gallons of fuel and reduce carbon dioxide emissions on the same order each year, which amounts to roughly two million dollars per day. Therefore, thoroughly understanding the drag

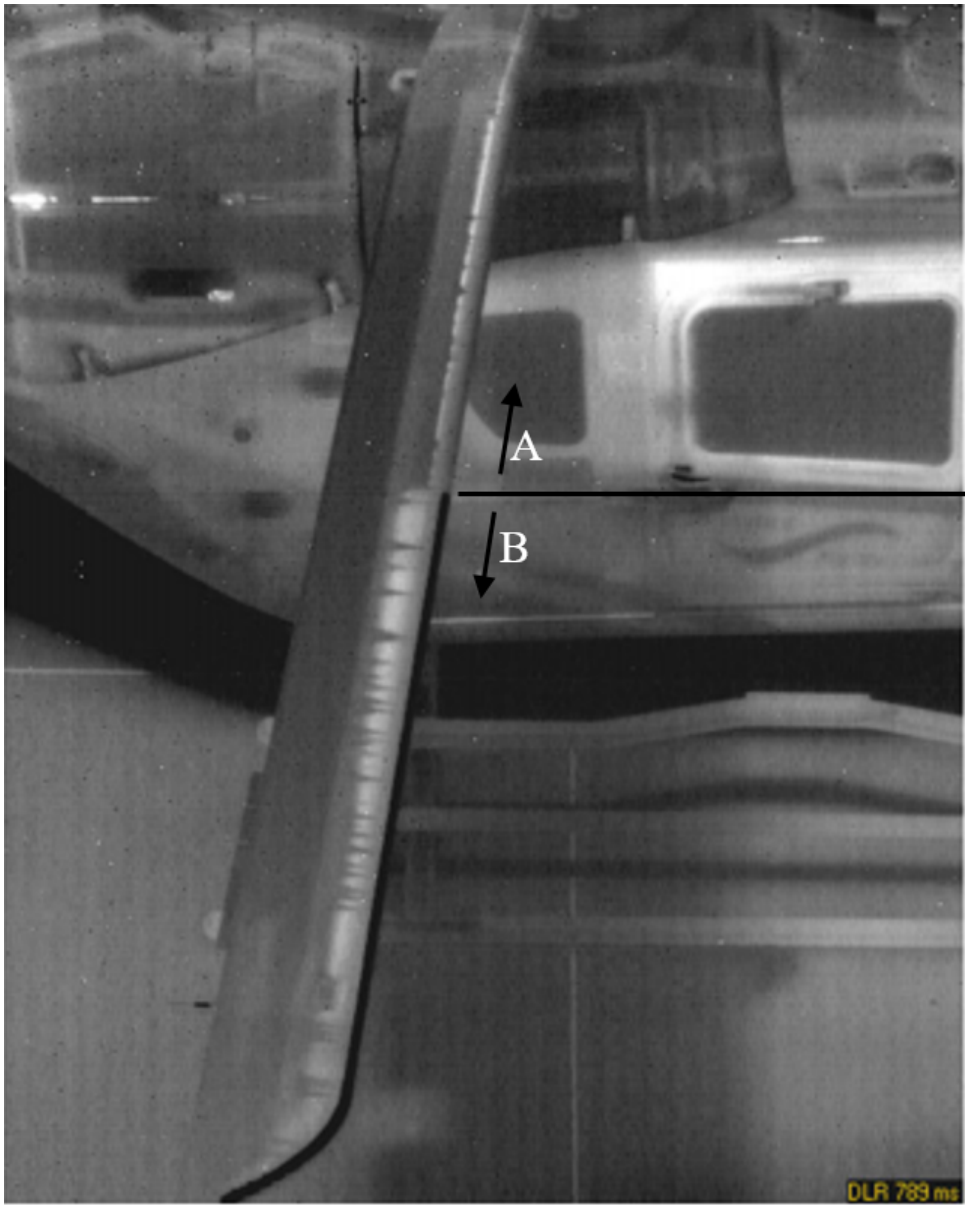

Figure 1.1: Transition on inboard section of rotor blade ("A"), where 0.367 mm protective tape is applied, is shown to occur prior to thirty percent chord. This early transition is not ideal, and highlights the drawback to leading edge protective tapes and to backward-facing steps in aerodynamic flows. The outboard section of the rotor blade ("B") is utilizing an embedded leading edge protection, which produces a smaller step height [7].

reduction mechanism leveraged by the CVG technology is incredibly valuable. The CVG specifically designed for the Boeing 737 are similar to those used on the helicopter application; however, the design of the tape's leading and trailing edges were modified to account for the leading edge slat and the swept wing planform. This version of the CVG is a thin strip of adhesive-backed thermoplastic polyurethane (TPU) which is placed behind the leading edge slat [10]. The sheet is less than a millimeter thick and extremely flexible which allows it to conform to the wing surface, and the general design has a serrated pattern on trailing edge as shown in Figure 1.2. CVG tape is applied outboard of the engine pylon and runs span-wise for the length of the leading edge slat.

Characterization of the CVGs drag reduction mechanism would allow the technology to be applied to many different flows. An obvious application would be to wind turbine blades, which have shown a 6-500 percent drag increased from various levels of erosion [11]. Protective tapes are a possible solution but have been shown to increase drag by 5-15 percent [12]. Therefore, the CVG technology could provide an efficient solution, which would drastically increase the viability of wind turbine power. This is only one of the possible future applications of this drag reduction technology. Others include, but are not limited to, turbomachinery, marine, biological, and thermal applications. However, in order to understand the limitations of the CVG technology and the applicable flow regimes, the drag reduction mechanism must be investigated and characterized, to better understand the physical mechanism involved.

1.3 Objectives

The objective of this study, to begin the investigation of the CVG device, was required prior to evaluating its effect on the flow field and characterizing the drag reduction mechanism. This entailed attempting to answer the following key questions regarding the CVG device and its applications:

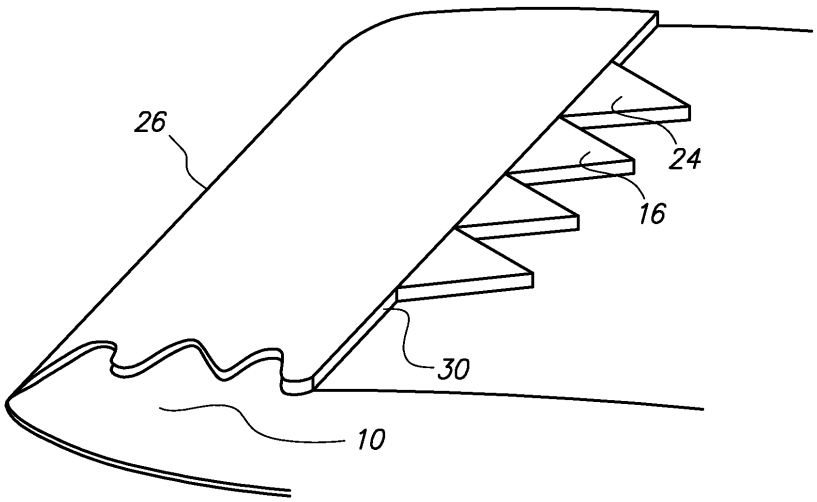

Figure 1.2: CVG tape applied to wing surface [13].

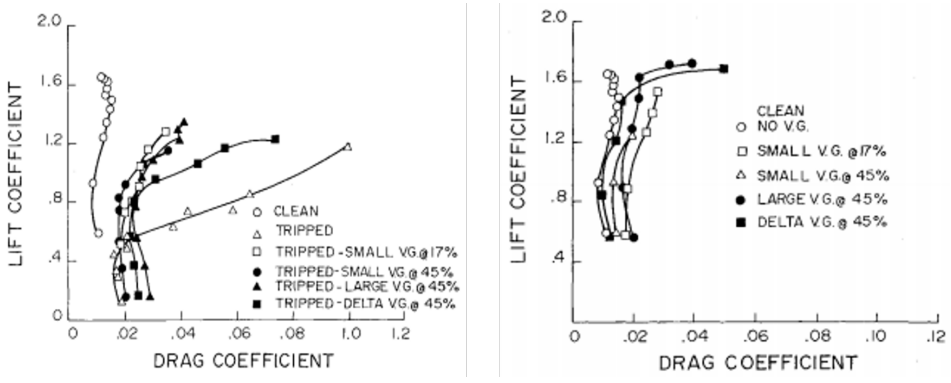

Figure 1.3: Lift and drag coeffiencts of flow over an airfoil. (left) Traditional Vortex Generator performance in tripped flow compared to clean configuration. (right) Traditional Vortex Generator performance in untripped flow compared to clean configuration [14].

- *How does the CVG device scale in different flow regimes?* The answer to this experimental question is required to begin thoroughly testing the CVG device and evaluating its effect on the flow. Until a known scaling relationship exists, it is impossible to evaluate the effect of the CVG without knowing that the same physical relationships produced in flight are being reproduced in the testing environment.

- *Is it possible to reproduce experimental results of flow around the CVG computationally?* Answering this question will determine if computational methods are a feasible option for evaluating the CVG flow interaction and characterizing the drag reduction mechanism. However, properly answering this question requires adequate experimental results, from either flight tests or accurately scaled tunnel tests using a proven scaling law, as mentioned in the previous research question. The only experimental results readily available to compare against are the flight test wall shear stress patterns obtained by Edge Aerodynamix. These qualitative results act as a pass-fail type of evaluation of computational results until additional experimental results become available from answering the first question.

- *What are the specific conditions and flow physics directly interacting with the CVG device?* Understanding the flow parameters at the location of the CVG for a given application is necessary to accurately scale or simulate the flow associated with the CVG. Various applications and flight test platforms exist for the CVG, and investigating their flow fields will provide the information needed to support answering the previous questions and develop a set of known boundary layer conditions in which the CVG device operates.

These questions guided the research and their answers were required to proceed from the initial investigation of the CVG device to evaluating the effect it had on the

surrounding flow field. Therefore, the work presented here lays the foundation for future work in attempting to characterize CVG drag reduction technology.

1.4 Outline

In Chapter 2, a thorough review of previous work related to turbulent boundary layers, backward-facing step flows, vortex generators, and drag reduction devices is provided. Chapter 3 contains the theory used to evaluate fluid flows. This chapter reviews relevant dimensionless parameters, the governing equations, analytical and approximate solutions of boundary layer properties, and Reynolds decomposition. Chapter 3 includes a general explanation of the particle images velocity (PIV) measurement method, Reynolds averaged Navier-Stokes (RANS) SST K-Omega turbulence model, large eddy simulation (LES) with the dynamic Smagorisky subgrid scale model, and improved delayed detached eddy simulation (IDDES) with RANS SST K-Omega wall treatment. Additionally, this chapter provides the five-scaled approaches evaluated in the work presented. Chapter 4 details experimental work accomplished by Edge Aerodynamix and Oklahoma State University. This includes various flight tests which evaluated fuel consumption, visualized transonic shock behavior, and subsonic wall shear stress patterns. Also presented is water tunnel testing of four-scaled approaches. Chapter 5 details the computational work accomplished by Oklahoma State University which includes two simulations that mirrored experimentally scaled approaches, two airfoil simulations (subsonic and transonic), and a large-scale simulation that reproduced subsonic flight test wall shear stress patterns. Chapter 6 summarizes the work accomplished, explores a proposed drag reduction mechanism, and provides recommendations for future work. Finally, Figure 1.4 provides a detailed illustration of the chronological research path, distinguishing between computational and experimental studies.

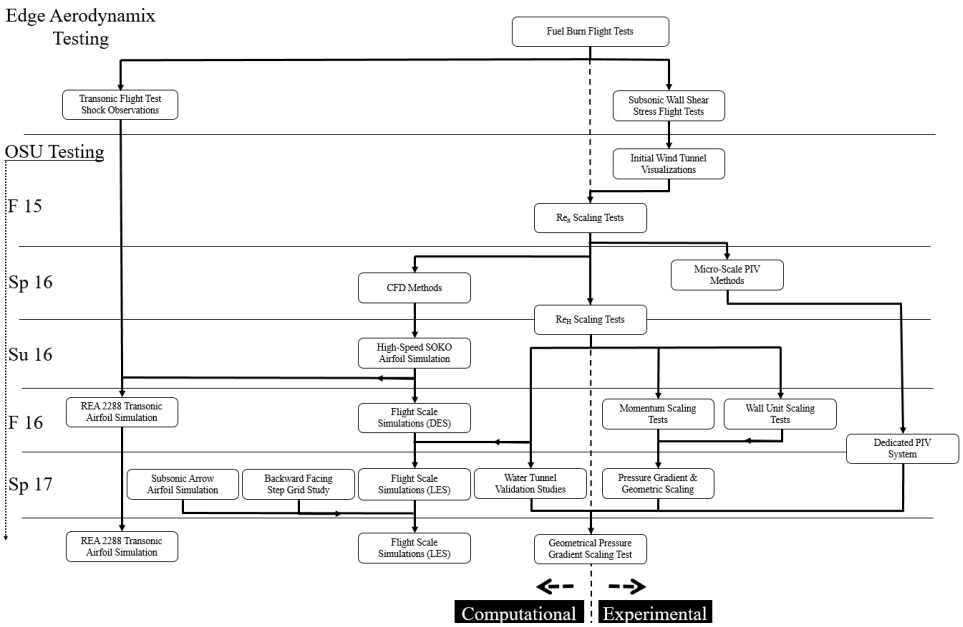

Figure 1.4: Illustration of research direction from Edge Aerodynamix test results into testing at Oklahoma State University.

Chapter 2

Previous Work

The majority of natural fluid flows present in the world are inherently turbulent. A few examples of naturally occurring turbulence are atmospheric boundary layers, magma flows, and ocean currents. Great effort is often required to maintain laminar flow for practical applications, such as airfoil design. The transition from laminar to turbulent flow is caused by instability in the laminar boundary layer, which can be triggered by geometrical inconsistencies at the boundary surface, external vibrations, or the natural destabilization of the laminar boundary layer with increasing Reynolds number. Engineered fluid-body interaction is often designed to either delay or force this transition in order to benefit from prolonged low wall shear stress that is associated with laminar flow, or the enhanced mixing and separation characteristics of turbulent flow. Perhaps the most well-known example of this is the dimpling of the golf ball. These spherical indentions were added to the surface of the golf ball in order to force the boundary layer to transition to turbulence earlier, as shown in Figure 2.1. The turbulent boundary layer has a greater resistance to separation, which results in devastating pressure drag. Forcing the golf ball's boundary layer to transition to turbulence earlier kept the boundary layer attached farther back around the ball, thus reducing the amount of pressure drag and increasing the distance the ball can travel. However, one of the major drawbacks associated with turbulence is the increased shear stress at the boundary, which is a direct product of better mixing and separation qualities. Therefore, drag reduction for turbulent flow is in high demand by civil transportation, military logistics, and other industries in which a relatively

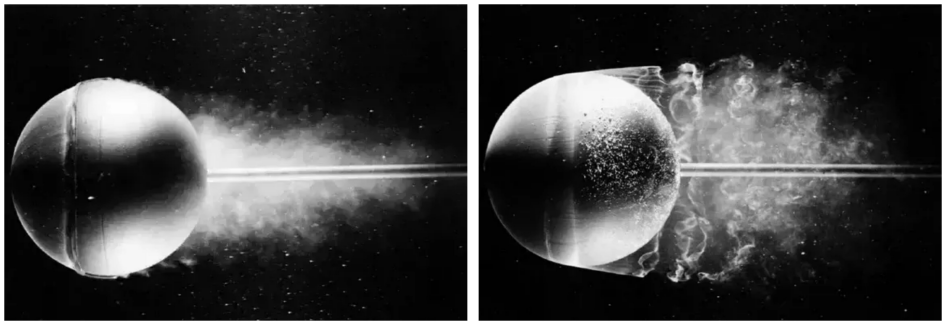

Figure 2.1: Flow visualizations over a sphere. (left) Tripped flow forcing early transition, resulting in better attachment around backside of sphere. (right) Natural transition further back on sphere, resulting in large separation region [15].

small increases in efficiency can have significant impacts. The turbulent boundary layer is the only method through which the boundary surface can influence the flow as a whole. This interaction is critical in the design of efficient aircraft, boat hulls, transport piping, and other surface-to-fluid interactions, and thus has large-scale applications.

This chapter briefly reviews previous work regarding turbulent boundary layer structures, flow past a backward-facing step, and flow control devices, which directly pertains to the research presented in this thesis. Many of the results from the papers mentioned in this chapter were used for comparison but are mentioned briefly here in order to explain their findings and provide context for later comparisons of results. The studies presented in this review have various limitations. The majority of the coherent structure research accomplished thus far has been based on flow visualization observations, which, at times, are misleading. Additionally, the statistical analysis of turbulent flow presents its own limitations. When using statistics to characterize turbulent flow, important aspects of the physics are lost. Furthermore, the majority of the CFD results presented here were all accomplished at low Reynolds numbers, which means that these results cannot be verified to scale at higher Reynolds number flows. However, the studies outlined in this review adequately support the ability to drastically influence the drag characteristics of turbulent flows from extremely

small-scale interactions.

2.1 The Turbulent Boundary Layer and Coherent Structures

Coherent motions and structures exist within a turbulent boundary layer, even though at first glance the flow behaviors seem to be completely random. Many experimental results and numerical simulations support the idea of self-sustaining motion present within the wall-region of the boundary layer ([16] [17] [18] [19]). The wall-region, $y^+ < 100$, contains the viscous sublayer, the buffer layer, and a small portion of the inertial sublayer; the rest of the boundary layer, $y^+ > 100$, is the outer-region. To further evaluate these structures a definition of coherent motion within a boundary layer is needed. Robinson defined these, in his thorough review of coherent motions in the turbulent boundary layer, as "a three-dimensional region of the flow over which at least one fundamental flow variable (velocity component, density, temperature, etc.) exhibits significant correlation with itself or with another variable over a range of space and/or time that is significantly larger than the smallest local scales of the flow" [20]. This definition is slightly ambiguous because the motions themselves are not well understood, which made it difficult to concisely define them. Many coherent motions have been identified within the wall-region of the turbulent boundary layer, some of which have surprisingly long lifetimes [21]. These coherent motions range from structures described as streaks, bursts, bulges, sweeps, ejections, and vortices. Perhaps the most interesting aspect of these coherent motions is that they occur within and originate from the wall-region. This is significant because of the drastically different length and velocity scales within the wall-region compared to those of the boundary layer as a whole. In experimental studies published by Lu and Willmarth (1973), the wall-region is shown to produce 77 percent of the average Reynolds stress turbulent energy [22]. This is more evident in Figure 2.2, which is a plot of the fraction of total production of turbulent energy as a function of the fraction of boundary

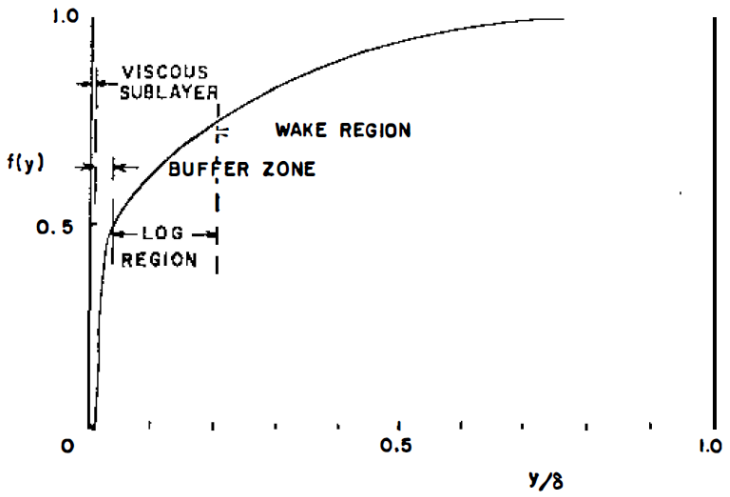

Figure 2.2: Plot of the fraction of total turbulent energy production as a function of fractional boundary layer location [24].

layer height. If the turbulent boundary layer and its containing structures are fully understood, then methods of controlling turbulence can be radically improved [23].

Streaks, which occur within the viscous sublayer, are among some of first observed structures. These are regions where higher and lower speed flows are in an alternating configuration, which result in organized streaks that typically have a span-wise spacing of 100 l_ν [25], which are shown in Figure 2.3. Streaks were first discovered using hydrogen bubble flow visualization in the late 1950s, and were considered to be the first part of a process described as bursting [26]. Observing the behavior of these streaks led to the development of a turbulent process known as bursting. In the original flow visualization experiments, the process was described as: streaks forming within the viscous sublayer, progressing downstream, moving slighting further away from the wall, and as they approached the buffer layer beginning to oscillate with growing amplitude until they broke up around the beginning of the inertial layer; as depicted in Figure 2.4. These results have been reprodcued, and it is now widely excepted that nearly all the net production of turbulent energy occurs in the wall-region [27]. Another coherent motion is the ejection, which consisted of faster moving fluid traveling upward from the wall and being ejected further outward from within the

wall-region [28]. Additionally, these ejections seemed to be linked to or even producers of another coherent motion called a sweep, which is the streamwise movement of fluid upstream that sweeps out fluid from the previous ejection event. Sweeps and ejections were measured and shown to produce approximately 70 percent of the Reynolds stress [29] within the boundary layer. These events were also described through flow visualization as a periodic fluid ejection from a thin region adjacent to the sublayer and are believed to be a factor in generating and maintaining turbulence [30]. CFD simulation, specifically DNS, has allowed researches to identify complex looped or ring-shaped vortices known as horseshoe and hairpin vortex formations. The distinction between these are based on the actual shape of the vortex loop. Wider loops, which occur at lower Reynolds numbers, are horseshoe-shaped, and thinner, narrow loops, which occur at higher Reynold numbers are hairpin-shaped, as seen in Figure 2.5. DNS has allowed these structures to be studied and visualized in great detail and has produced complex visualizations of these vortex formations as shown in Figure 2.6. The DNS work of Chog et al. (1998), found that these looped vortex structures are linked to Reynolds stress generation, and more recent DNS, performed by Lee et al (2011), focused on evaluating the hairpin vortex structures and, more specifically, the packets in which hairpin vortices tend to form [31] [32]. Hairpin packets are groups or families of hairpin structures, as shown in Figure 2.7, and have been shown to auto generate, even for high Reynolds number flows, which were evaluated numerically and experimentally through DNS and PIV by Adrian (2007) [33].

These coherent motions, have been studied over the last fifty years and are still in question. Specifically, the bursting process is not yet uniformly agreed upon. Bursting has been compared to the transition from laminar to turbulent flow, which suggested that the inner portions of the wall region remained in a state of continuous transition; still, some studies completely dismissed this comparison. [34]. The relatively accepted understanding of bursting, taken from flow visualization, describes bursting as sudden

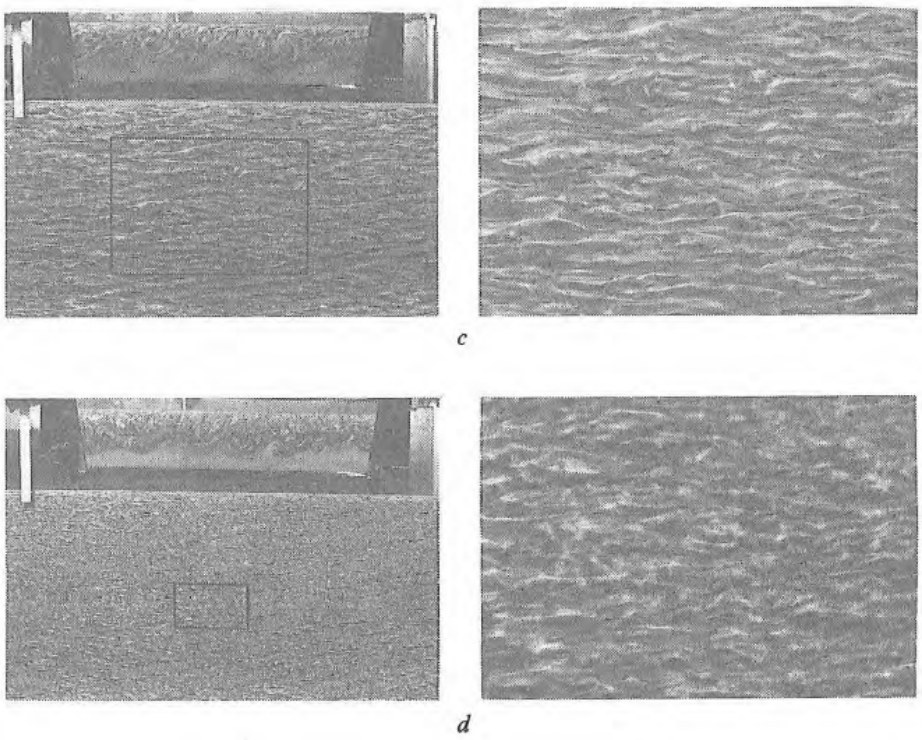

Figure 2.3: Low-speed streak formations [34].

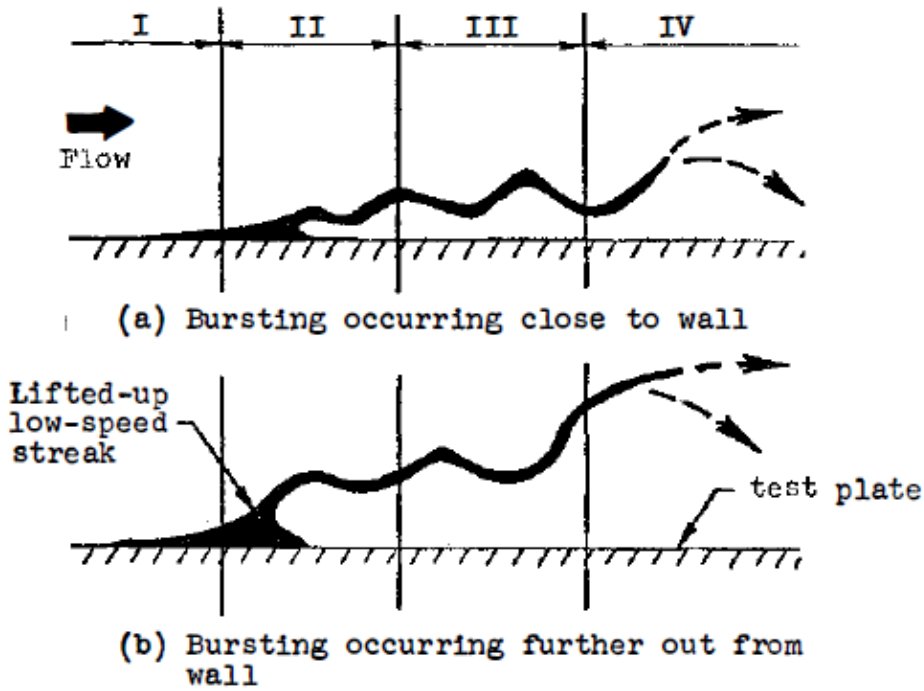

Figure 2.4: Illustration of the coherent motions of the bursting process as identified from hydrogen bubble visualization [35].

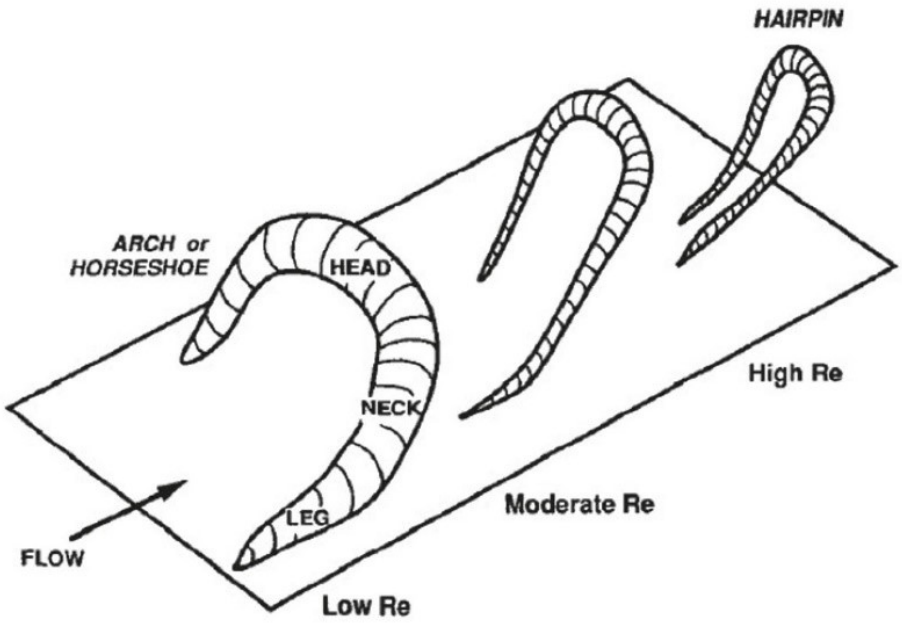

Figure 2.5: Depiction of loop vortex formations (arches and hairpins) [20] [36].

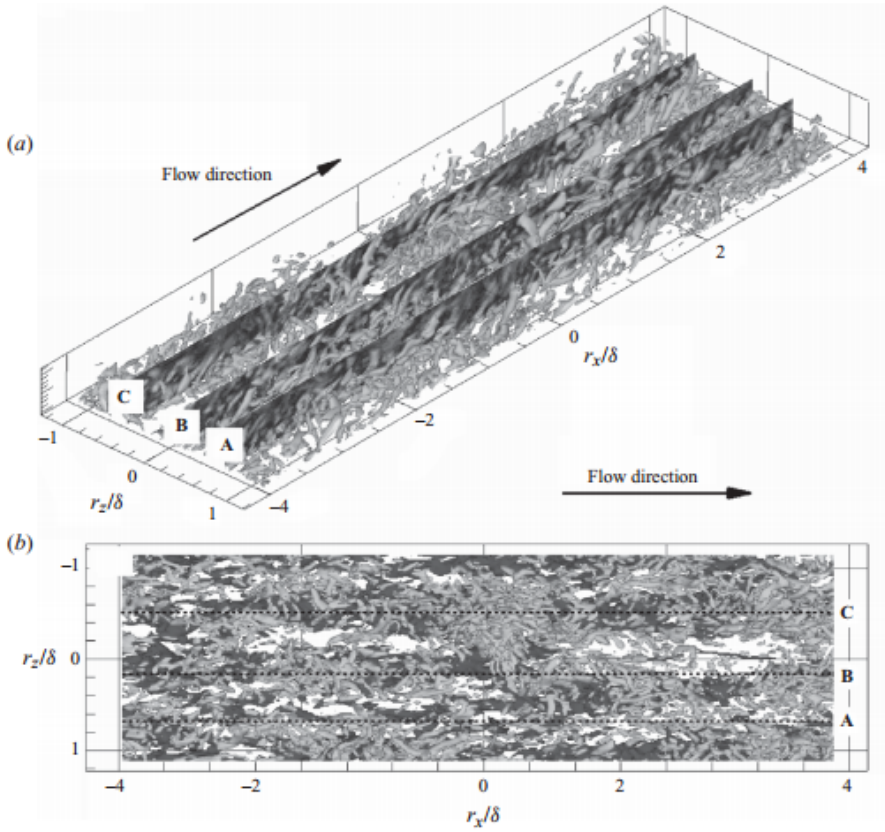

Figure 2.6: Hairpin structure visualizations from DNS simulation [32].

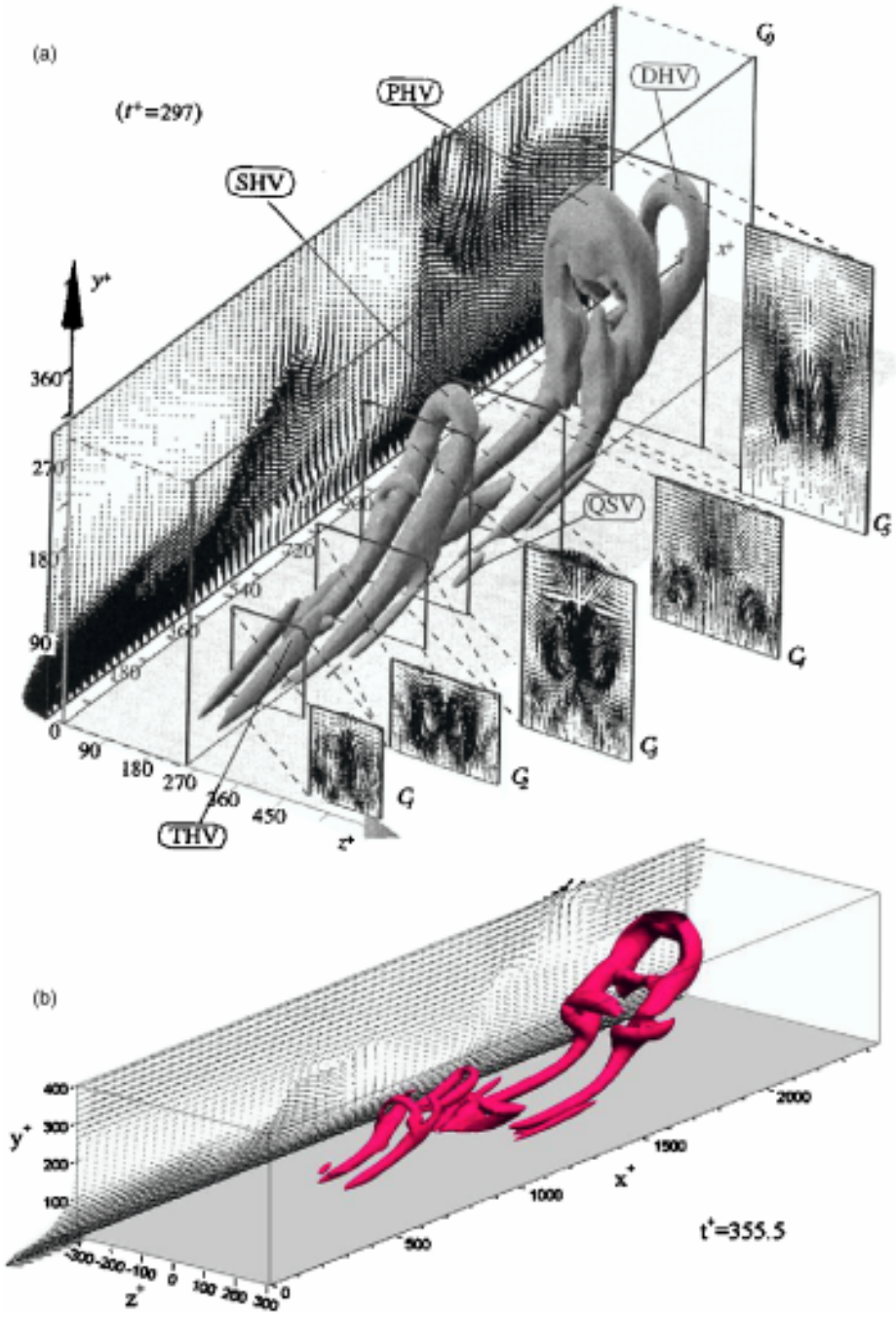

Figure 2.7: Visualization of hairpin packet formation [33].

eruptions that move slower fluid from the viscous sublayer toward the outer-region [35]. However, In one study, utilizing direct numerical simulation, tilted streamwise vortices dominated the wall-region in low Reynolds number flow [20]. This brings forth a slightly different theory that suggests the bursts are a result of localized ejections coming from these quasi-streamwise vortices, which persist for longer time scales than the ejections, have a radius of $R = 10\text{-}15\ l_\nu$, and a streamwise length of $x = 1000\ l_\nu$ [37]. This explanation contradicts the abrupt and explosive nature which previously described the bursting process. This indicates that the current explanations regarding the behavior of turbulent energy producing structures will most likely continue to adapt to new findings. However, the coherent motions that are currently known to exist within the wall-region are elongated streaks of regions with high and low velocity within the viscous sublayer [30]. Outward ejections of high-speed fluid exist intermittently throughout the wall-region beyond $y^+ = 12$ and inward sweeps of low-speed fluid exist within the wall-region below $y^+ = 12$ [38]. The wall-region is well populated with quasi-streamwise vortices that have a slight upward tilt as they move downstream [39]. These vortices are considered to have an association with the sweeps and ejections, and therefore could be major contributors to the production of Reynolds stresses [40]. Assuming that strong streamwise vortex structures are common in the wall-region [24] and using them to relate all of the turbulence events together, a rough model of turbulent production has been produced. The low and high speed streaks are a product of the quasi-streamwise vortices as shown in Figure 2.8. As the streamwise vortex begins to move away from the wall, it causes the low-speed and high-speed streaks to become unsteady and generate the sweeps and ejections Figure 2.9. The streamwise vortex then moves further away from the wall and rolls-up with an adjacent vortex creating a hairpin or horseshoe vortex structure (depending on the Reynolds number). This entire process is depicted in Figure 2.10. The majority of researchers agree that all the motions are interconnected, but they

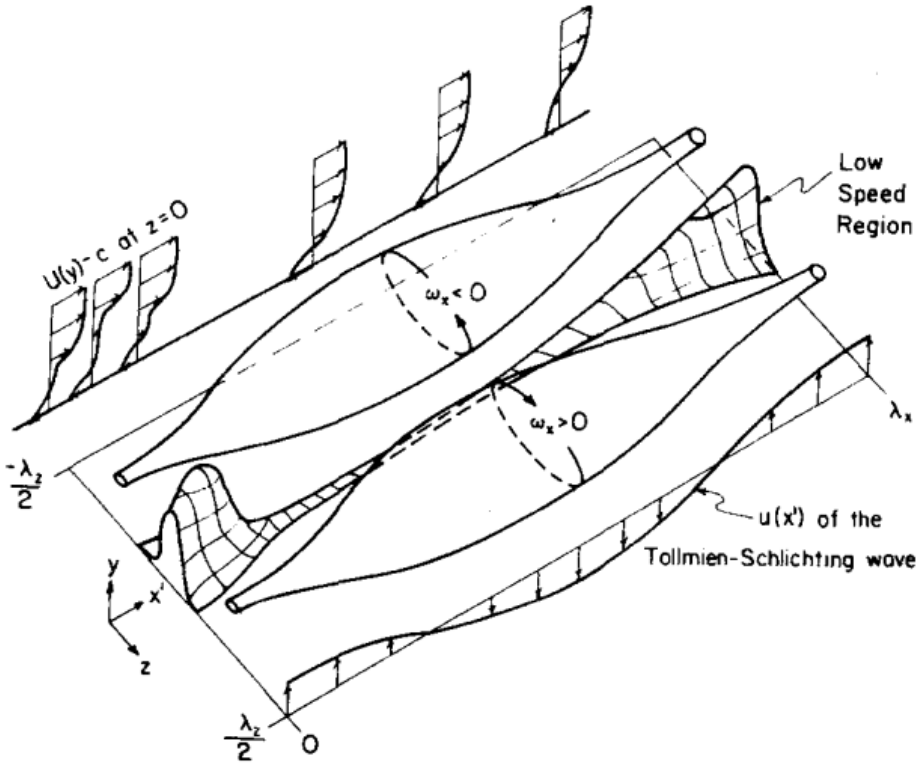

Figure 2.8: Model of near-wall boundary layer streamwise vortices and their relationship to streaks [34] [41].

often disagree on how they relate to each other or which coherent structures dominate. Regardless of the exact methods by which the production of turbulent energy occurs, it is generally accepted that the wall-region contains the various coherent structures that are responsible regenerating turbulent motion.

2.2 Backward-Facing Step Flows

Flow over a backward-facing step is a classical fluids problem. The main characteristics of backward-facing step flows are the incoming boundary layer, shear layer, primary recirculation region, secondary recirculation region, reattachment zone, recovery region, and coherent hairpin vortex formations. Figure 2.11 provides a illustration of these flow features and their relationships to each other. The boundary layer thickness prior to the step, which could be laminar or turbulent, defines how the step scales with the flow. Adams, (1988) found that reattachment of laminar inlet

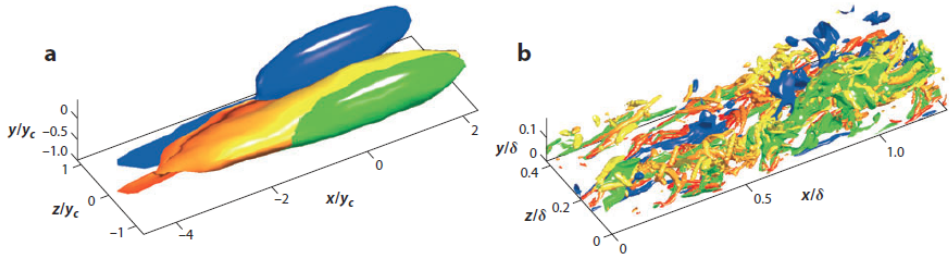

Figure 2.9: (a) The averaged Reynolds stress structure with a sweep (blue, farthest into page) next to an ejection (green, closest into page) around the central streamwise vorticity. (b) The instantaneous realization of the same structure [21].

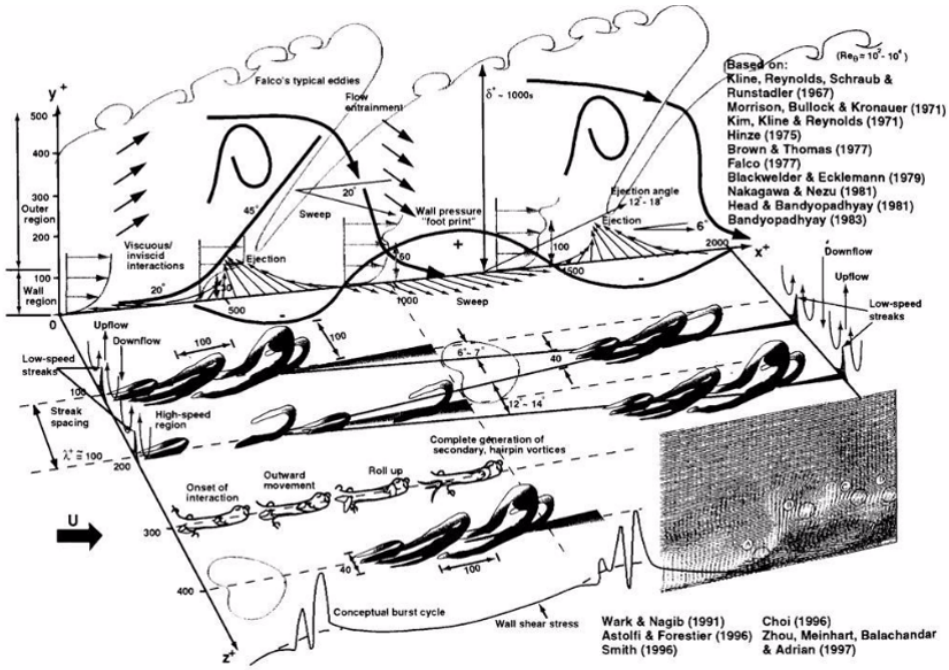

Figure 2.10: Illustration of the turbulence production process taking into account many combined souces descpritions [42].

boundary layers occur in 30 percent shorter distance than those of initially turbulent flow [43]. The inlet length for numerically simulated flow is significant, and Erturk (2008) found that an inlet length of at least 5 step-heights was required to produce an accurate solution for backward-facing step flows[44]. The shear layer is the portion of the flow that "falls" over the step and produces a shear interaction with the high-speed flow above the step hight and the recirculating flow below the step. This shear layer is directly related to the reattachment location and has been shown to fluctuate, or flap, causing the reattachment length to vary with time [45]. Reattachment is the location where the separated flow reattaches to the bottom wall and is identified by a zero wall shear stress. The reattachment length is the subject of many exponential and computational experiments and has been shown to occur between 4.9 to 8.2 step-heights depending on initial boundary layer height, level of freestream turbulence, aspect ratio of the step to test width, pressure gradient, and whether the boundary layer is initially laminar or turbulent. [46]. Some DNS showed that reattachment occurred at 6.28 step-heights and, also, that the reattachment length behaved quasi-periodically with at Strouhal number of 0.06 [47]. Additionally, it was noted that, in the recovery region, a downward shift existed in the log-region of the law of the wall velocity profile. This is consistent with Jovic and Driver (1995) as shown in Figure 2.12. Additionally, the point of reattachement has been modified or controlled through various means of oscillating geometry [48], or through speaker induced pressure waves [49]. Reattachment length was also shown to be sensitive to the three-dimensionality of a flow and the presence of sidewalls, which has been explored experimentally and computationally [50] [51]. The primary recirculation region is a product of the shear layers viscous effect on the otherwise stationary flow immediately behind the step. A secondary recirculation bubble, or corner vortex also exists, which appears to play a significant role in the flapping behavior [52] [53]. The recovery region is immediately downstream of the reattachment point, where the flow

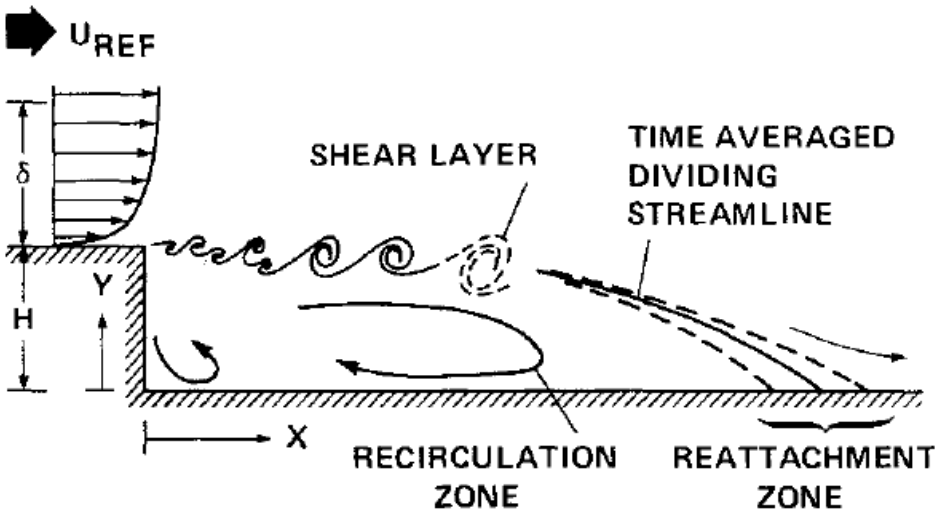

Figure 2.11: Illustration of flow over a backward-facing step [45].

has reattached to the surface, begun to reorganize, and recovered a turbulent velocity profile. Hairpin structures downstream of backward-facing step geometry have been identified with PIV measurements, which were shown to be an adequate method for evaluating and analyzing these coherent motions [54] [55]. A swept backward-facing step was experimentally studied by Weber (1992) which found that the primary effect was a faster recovery as the sweep angle increased [56]. In addition, transonic flow over backward-facing steps was shown to produce an expansion shock that increased in width and length as step height increased [57].

The backward-facing step flow proves difficult to accurately simulate not only because it is wall-bounded, but also because it is separated past the step. Thangam (1992) states that properly calibrated two-equation RANS models may obtain reasonable results in backward-facing step flows; although they did not discount the deficiencies of the model [59]. Various LES sub-grid scale models have been evaluated using the backward-facing step as a test condition. The structure-function sub-grid scale LES model compared favorably with experimental results for flows over a backward-facing step [60]. In a similar study, the Smagorinsky, dynamic Smagorinsky, and structure function sub-grid scale models showed overall satisfactory results

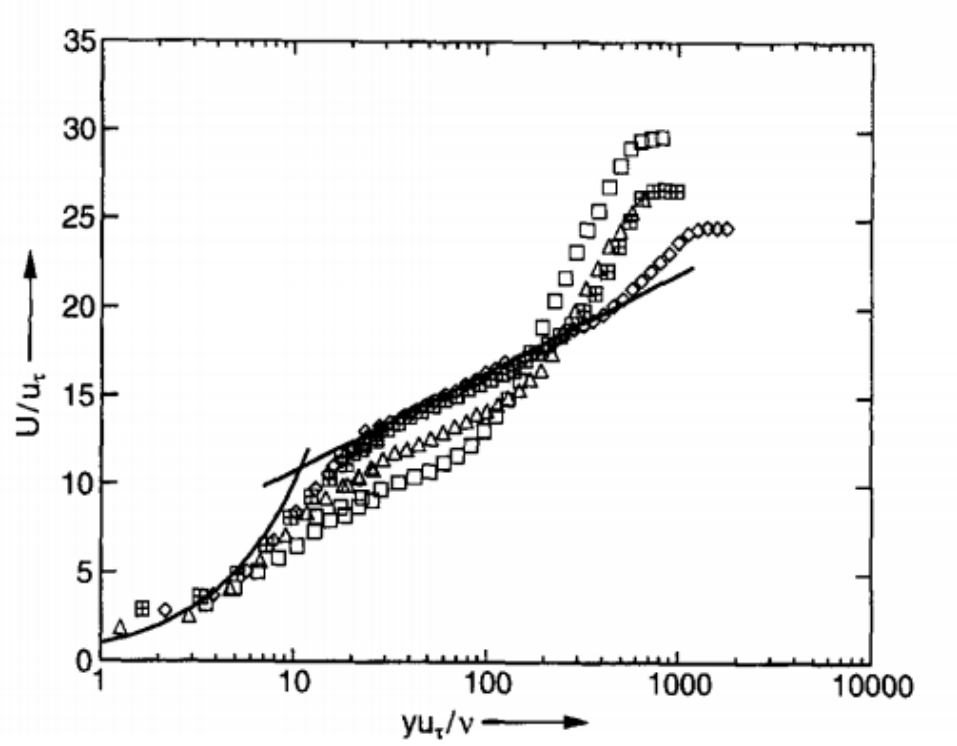

Figure 2.12: Mean velocity profiles indicate log-region shift near backward-facing step [58].

in comparison to DNS results; however, the lengths of recirculation zones were over predicted by all of the LES models [61]. Another LES investigation of unsteady flow over backward-facing steps found that a proper upstream definition of the flow is crucial for accurate simulation of the structure and dynamics of the flow [62]. Fureby (1999), concluded that in backward-facing step flows the LES model is not particularly sensitive to the sub-grid scale model if grid resolution is sufficiently fine for the type of flow being modeled [63]. These results build confidence in the LES model for backward-facing step flows; however, they also indicated that special care was required to properly design an accurate simulation.

2.3 Flow Control

2.3.1 Vortex Generators

Vortex generators are traditionally associated with separation control and not specifically drag reduction. While improving separation characteristics drastically reduces the effects of pressure drag, vortex generators often provide this benefit at the cost of additional parasite drag. However, depending on the specific application the positive effects of mitigating separation may drastically outweigh the drag penalty. An example of this is vortex generators applied to high lift devices which are at extreme angles of attack. Lin (2002) found that micro-vortex generators can be applied to high-lift flap devices and that they drastically improve separation [64]. Many variations of vortex generators exist for specific applications, and they often produce unique vortex formations as shown in Figure 2.13. Some vortex generator designs outperform others in specific flow regimes. For instance, Yao (2002) found that low profile vortex generators perform better at high angles of attack than do traditional vortex generators [65]. Supersonic applications have shown that mirco-ramp type vortex generators can significantly improve shockwave induced boundary layer separation but at the expense of drag [66]. The Gurny flap has been shown to significantly increase lift, with a minimal increase in drag at low angles of attack, by prolonging attachment [67]. Vortex generator application to flows that are prone to large separation regions is ideal, even ground vehicles can benefit. Aider (2010) found that a line of vortex generators for ground vehicle applications can reduce drag and increase downward force by 12 and 60 percent respectively [68]. CFD simulation around these devices can be difficult due to the high Reynolds number ranges, separated regions, and near-wall effects from there associated flow fields. However, some successes have occurred when using the RANS SST K-Omega turbulence model, which sufficiently modeled the vortex path and circulation but over-predicted maximum vorticity and

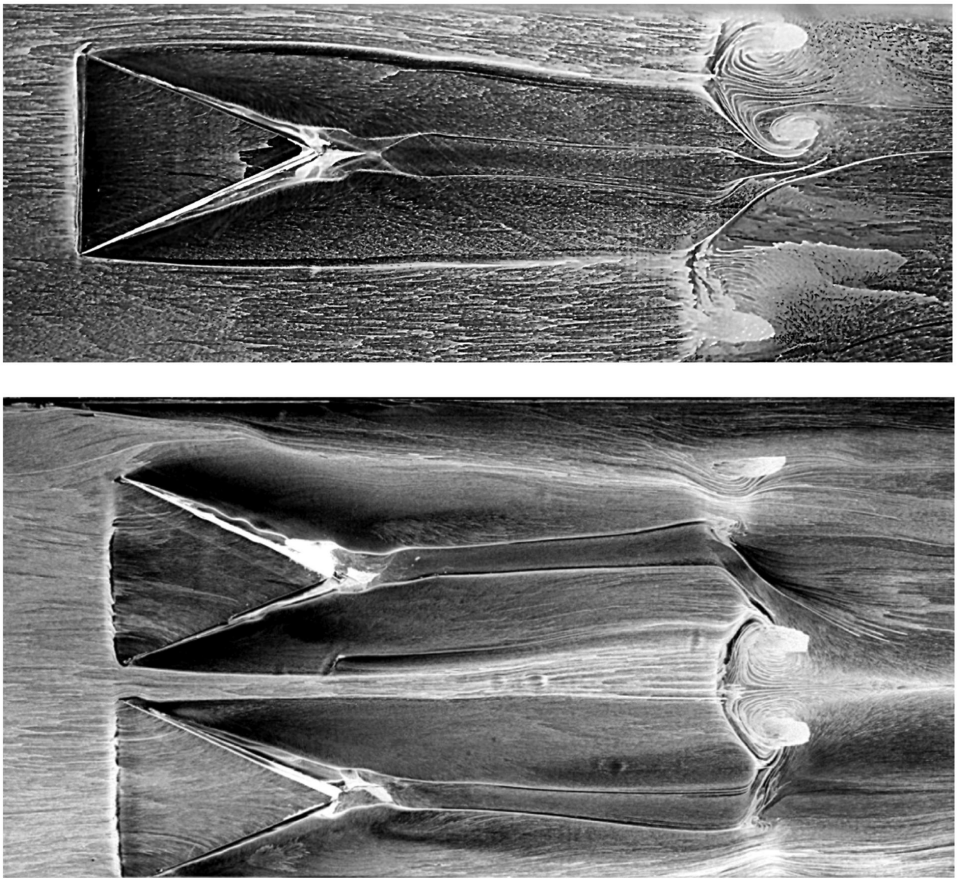

Figure 2.13: Unique vortex formations downstream of supersonic microramp vortex generator [66].

radius [65]. This suggests that modeling flow around control devices could require multiple design iterations and special attention to detail.

2.3.2 Drag Reduction Devices

In section 2.1, the coherent motions of the turbulent boundary layer were discussed, and it was noted that the majority of turbulent kinetic energy production occurs within the near wall-region. Therefore, attempts to control turbulent boundary layer behavior with small-scale geometry, on the same order of height as the wall-region, is a topic of interest. It has been shown that even elements of surface roughness larger than a few wall units can interfere with the buffer layer viscous cycle [69]. This means that the smallest of surface geometry could have a noticeable effect on the coherent

Observed Phenomena	Microturbulent Activities	Fluid Dynamic Mechanisms	Drag Reduction Strategies
Burst ↓	Near-wall burst deforms a spanwise vortex element		
Streaks ↓	Legs of counterrotating, streamwise vortices form low-speed streaks between the legs	Nonlinear self-interaction	Riblets impede spanwise movement of longitudinal vortices, reduce momentum flux within riblet valley, impede energy redistribution from u' to w', and reduce near-wall burst duration and intensity (Choi, 1996). Spanwise movement of $\Delta z^+ \cong 50$ disrupts formation of longitudinal vortices and reduces turbulence production (Akhavan et al., 1991)
Liftup ↓	Stretched vortex evolves into a hairpin vortex loop		Lorentz pressure gradient suppresses amplification of streamwise vorticity (Nosenchuck and Brown, 1993)
Ejections ↓	Ejection of low-momentum fluid away from wall	Nonlinear vortex mutual induction	Polymer injection damps vortical motions, increases spacing of streaks, and reduces ejection and sweep frequencies and intensities (Tiederman and Luchik, 1982). Suction-blowing out of phase with sweep and ejection inhibits longitudinal vortex interaction with wall (Kim et al., 1990)
Breakup ↓		$U(y,z)$ inflectional profile leads to instability	Microbubble splitting in turbulence provides an additional energy dissipation in small scale activities (Meng, 1985)
Sweeps ↓	Sweep of high-momentum fluid toward wall	Large-scale outer structure and advection of mean shear	Compliant coating motion counters local fluid motion and interrupts the turbulence production cycle (Choi, 1996). Deferring the sweep without modifying the streamwise vortices (Choi et al., 1994)
Renewals	Near-wall bursts renew under the vortices, forming a staggered pattern relative to the previous near-wall burst and completing the cycle	Viscous-inviscid interaction	Randomization of largest length scale (Handler et al., 1993)

Figure 2.14: Outline of various drag reduction methods and the associated turbulent boundary layer interaction [42].

motions within the wall-region. An overview of known drag reduction devices and their interaction with the turbulent structures is provided in Figure 2.14. However, a brief review provided here focuses on drag reduction devices which operate in the near-wall region, like the CVG.

Riblets are an excellent example of a passive drag reduction device. These micro-ridged surfaces have been shown to reduce drag by as much as 10 percent through experimentation, and a 2 percent in total drag was achieved in an Airbus aircraft flight tests [70]. LES results presented by Peet (2010), support a theorized riblet drag reduction mechanism of displacing streamwise vorticies further from the wall [71]. The displacement causes the riblet peaks to have a higher shear stress than what is normally experienced at a flat boundary wall under the same flow conditions. However, because the vortices cannot make direct contact with the valleys of the riblets, the shear stress within the riblet geometry is greatly reduced. The final drag reduction would then be produced because the peaks have much smaller surface areas compared to the interior of the riblet geometry. Therefore, when the total wall shear is considered, the total drag is reduced. This theory is further supported by the computational study conducted by Tullis (1994), which focused on modeling the

streamwise vortices interaction with the riblet geometry [72]. The computed cross-stream results given in Figure 2.15, in which the vectors represent the cross-stream velocities (the contours are static pressure and the flow direction is into the page) provide a clear picture of this vorticity displacement phenomena. In the top image of a flat wall boundary, the streamwise vortices are obvious and their effect on the pressure field is clearly depicted with respect to the upward and downward rotation of the vortices. In the middle image of the V-groove riblets, the vortices are displaced from the wall (along with the pressure field disruption) and riding on the top of the riblet peaks. In the bottom image the U-groove riblets produce a similar effect of displacing the streamwise vortices from the wall. These results support the theorized riblet drag reduction mechanism and reinforce the importance of scaling. If the riblet geometry is not scaled within the acceptable range, then the riblets will be too small and physically represent a surface roughness on a flat boundary, or if they are too large, then the vortices could easily fit within the riblet valleys and greatly increase the total wall shear stress.

In a study by Sandborn (1981), in which the control of surface shear stress was investigated, vane-type geometries spaced closely together in an array-like pattern resulted in significant drag reductions [73]. The resulting characteristics of the reduction of shear stress was quite similar to riblets. The significant difference was that the height of the vanes was larger than riblet micro-peaks, and the vanes had a short longitudinal length, as opposed to the riblets longitudinal structure. The conclusion was that the closely spaced vanes were most effective at reducing shear stress but only for a short distance behind the vane structures [73]. A remarkably similar investigation by Rao (1983), found no significant reduction in shear stress. The closing statements suggest that the scaling of the tested geometries may not have been appropriate [74]. The inconsistences between these two studies make it difficult to draw conclusions from either one.

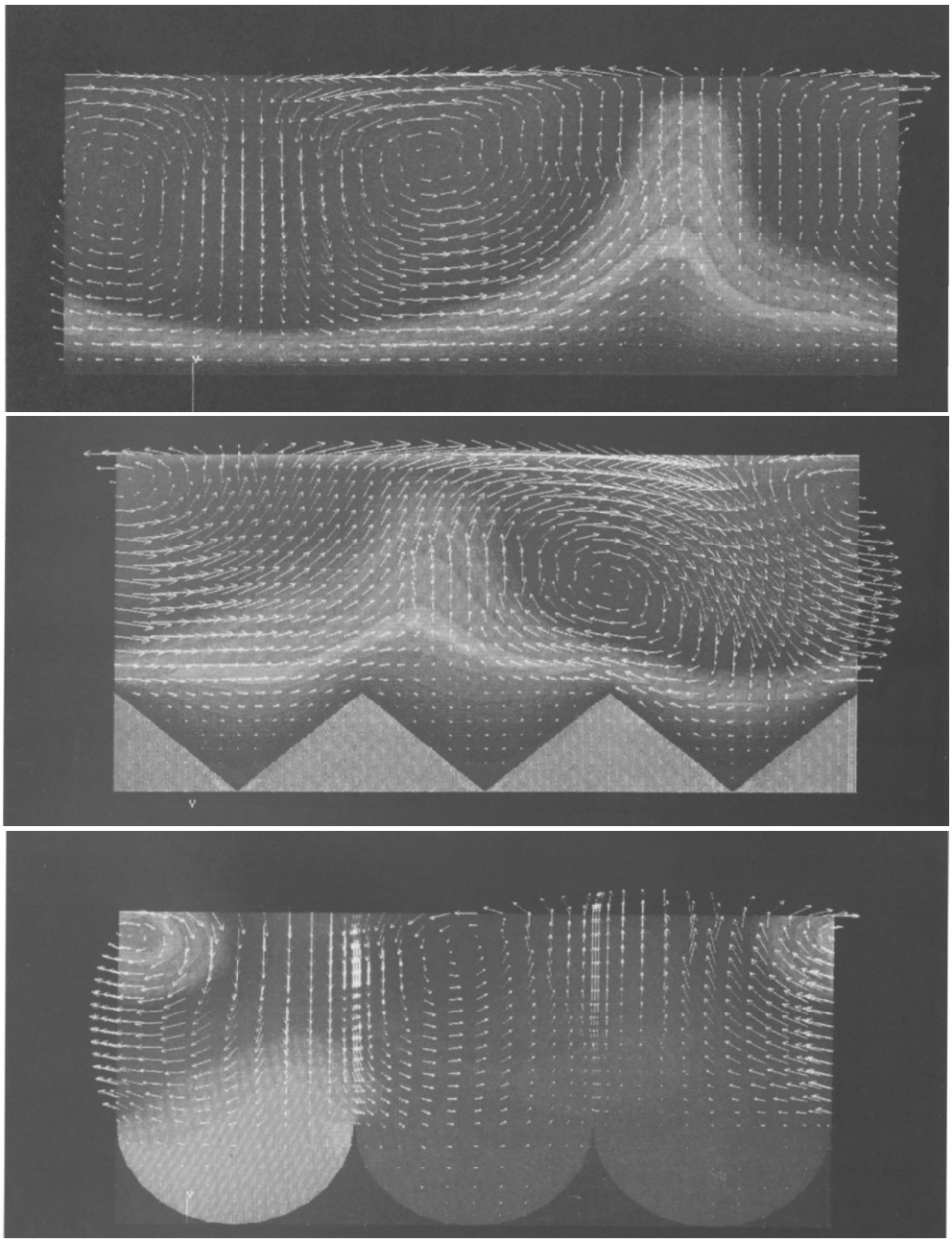

Figure 2.15: (top) Calculated flow over plain wall, (middle) V-groove, and (bottom) U-groove. The vectors represent cross-stream velocities, and the contours of static pressure [72].

The computational study of sinusoidal geometry presented by Peet (2010) found that the riblet structure could be further optimized over the traditional V-groove design. Drag reduction was reported as high as 7.4 percent for the larger wavelength sinusoidal geometry [71]. However, this is contradictory to Walsh's (1983) study, which found that a drag reduction as high as 8 percent could be achieved with the V-groove riblet geometry [75]. Therefore, the results of both studies leave room for questions and provide reasons to attempt to replicate the results. Yet, what can be agreed upon about the two studies is that a significant drag reduction occurs when using riblets of the proper scaling size and that the exact scaling is fairly sensitive to the geometry and scale of the riblet. This is significant because, as more studies like these are carried out, the known boundaries of the geometrical scaling for efficient riblets will be further constrained until a well-defined scaling law emerges.

Simular types of drag reduction have been therorized and compared to riblet drag reduction. In Bushnell's (1991) review of drag reduction in nature, a ridge feature found on shark dermal denticles was noted as having similar geometry and orientation compared to riblets [76]. The study presented by Tani (1988), revealed that the riblet drag reduction mechanism seems to scale similarly to sand grain roughness [77]. It was shown that for small values of wall-unit scaling, both sand-grain roughness and riblet micro-grooves reduced drag. However, as the wall-unit sizing of the roughness scale feature increased, the effect was reversed, and drag actually increased. These results implied that the cutoff geometry scaling for drag reduction in sand-grain roughness is approximately $y^+ = 6$, where anything higher than 6 increased the drag force. Similarly, an effective cutoff range could be applicable to any device with a similar drag mechanism.

Chapter 3

Background Theory

3.1 Dimensionless Parameters

There are a number of different known dimensionless parameters which directly pertain to this area of research. A brief description of each is given below for reference when they appear throughout this thesis. The first is Reynolds number (Equation 3.1), which is the ratio of inertial forces to viscous forces in a flow. This parameter is especially valuable in determining the likely state of a wall-bounded flow where laminar flows generally occur below a Reynolds number of five hundred thousand and above that transition to turbulence occurs. However, this is dependent on many different factors such as surface roughness or turbulent intensity of the freestream. The general form of Reynolds number is given below, but other existing definitions vary slightly and become pertinent when different dominant length scales are used. For example, a flat plate boundary layer is usually defined by the downstream distance, but in pipe-flow. the diameter of the pipe is used since it is the dominant length scale. These variations are used to describe different aspects of flow for different flow types. The Reynolds number based on step height H (Equation 3.2), relates the inertial forces to the viscous forces relative to the step height and characterizes how influential the step is to the flow. It is important to note that this relationship does not give any indication of boundary layer development; therefore, additional variations of Reynolds number are often used in conjunction with each other. It is common for a Reynolds number based on different boundary layer definitions to be used, such as the generic boundary layer Reynolds number (Equation 3.3), the displacement thick-

ness Reynolds number (Equation 3.4), or the momentum thickness Reynolds number (Equation 3.5). A form of Reynolds number commonly used in CFD is the Friction velocity Reynolds number (Equation 3.6), which provides information on how well-developed the flow is by relating the boundary layer thickness and friction velocity to the viscous effects.

$$Re_x = \frac{\rho U x}{\mu} \tag{3.1}$$

$$Re_H = \frac{\rho U H}{\mu} \tag{3.2}$$

$$Re_\delta = \frac{\rho U \delta}{\mu} \tag{3.3}$$

$$Re^*_\delta = \frac{\rho U \delta^*}{\mu} \tag{3.4}$$

$$Re_\theta = \frac{\rho U \theta}{\mu} \tag{3.5}$$

$$Re_\tau = \frac{\delta u_\tau}{\mu} \tag{3.6}$$

The Strouhal number (Equation 3.7) relates the viscosity to velocity for shedding phenomena. Large Strouhal numbers indicate that the flow is viscous dominate and that vorticity in the flow is a dominate effect. Small Strouhal numbers indicate that the velocity dominates and that the effect of the vorticity is not large relative to fluid speed. Strouhal number is often used to compare shedding frequencies behind airfoils, cylinders, or backward-facing steps. Froude number (Equation 3.8) provides information regarding the effects of gravity on a flow. Mach number (Equation 3.9) relates

the characteristic velocity to the sound and provides insight on the compressibility of the flow. Generally, compressibility effects are neglected for flows with Mach numbers of less than 0.3. The coefficient of friction (Equation 3.10) relates the wall shear to the kinetic energy. Large coefficient of friction indicates that the flow is dominated by wall shear stress. Similarly, the coefficients of drag (Equation 3.11), lift (Equation 3.12), and pressure (Equation 3.13) all relate a force or pressure to the energy in flow.

$$St = \frac{\Omega l}{U} \tag{3.7}$$

$$Fr = \frac{U}{\sqrt{gl}} \tag{3.8}$$

$$Mach = \frac{U}{c} \tag{3.9}$$

$$C_f = \frac{\tau_w}{\frac{1}{2}\rho U^2} \tag{3.10}$$

$$C_D = \frac{F_D}{\frac{1}{2}\rho U^2 A} \tag{3.11}$$

$$C_L = \frac{F_L}{\frac{1}{2}\rho U^2 A} \tag{3.12}$$

$$Cp = \frac{p - p_\infty}{\frac{1}{2}\rho U^2} \tag{3.13}$$

3.2 Governing Equations

The governing equations for this work were the continuity equation, conservation of momentum, Naiver-Stokes momentum equations, and the conservation of energy,

shown in Equations 3.14, 3.15, 3.16, and 3.17 respectively. A dimensional analysis of the incompressible Naiver-Stokes equation produces a dimensionless form of the momentum equation as shown below (Equation 3.18) [78]. Within this equation, dimensionless terms previously discussed are easily identifiable, and for the work presented here, gravity effects were always assumed to be negligible. This form of the equation suggests that, for high Reynolds numbers, the viscous effects are negligible; therefore, a further reduced form of the Naiver-Stokes equation, the Euler equation, may be used. However, this is counter intuitive when considering the problem at hand. The CVG technology is applied to extremely high Reynolds number flows, but based on its thickness compared to the boundary layer height, the viscosity effects must have a meaningful interaction with the device. This illustrates the profound difficulty of studying the CVG device, as it requires both inertial and viscous effects to be considered.

$$\frac{1}{\rho}\frac{D}{Dt}\rho + \nabla \cdot \vec{u} = 0 \tag{3.14}$$

$$\rho\frac{Du_j}{Dt} = \rho g_j + \frac{\partial}{\partial x_i}(\tau_{ij}) \tag{3.15}$$

$$\rho\frac{Du_j}{Dt} = -\frac{\partial p}{\partial x_j} + \rho g_j + \mu\frac{\partial^2 u_j}{\partial x_i^2} + \left(\mu_\nu + \frac{1}{3}\mu\right)\frac{\partial}{\partial x_j}\frac{\partial u_m}{\partial x_m} \tag{3.16}$$

$$\frac{\partial}{\partial t}\left(\rho\left[e + \frac{1}{2}u_j^2\right]\right) + \frac{\partial}{\partial x_i}\left(\rho\left[e + \frac{1}{2}u_j^2\right]u_i\right) = \rho g_i u_i + \frac{\partial}{\partial x_i}\left(\tau_{ij}u_{ij}\right) - \frac{\partial q_i}{\partial x_i} \tag{3.17}$$

$$\left[\frac{\Omega l}{U}\right]\frac{\partial \vec{u}^*}{\partial t^*} + (\vec{u}^* \cdot \nabla^*)\vec{u}^* = -\nabla^* p^* + \left[\frac{gl}{U^2}\right]\vec{g}^* + \left[\frac{\mu}{\rho U l}\right]\nabla^{*2}\vec{u}^* \tag{3.18}$$

3.3 Boundary Layer Theory

3.3.1 Laminar

The laminar boundary layer is well defined for flat plate boundaries. For a zero pressure gradient, the Blasius solution may be used to produce Reynolds number-dependant boundary layer thicknesses (Equations 3.19, 3.20, 3.21, and 3.22) [79]. With a pressure gradient, the Von Karman momentum integral formulation may be used with momentum thickness, displacement thickness, and wall shear as unknowns. Additionally, Thwaites method may be used to evaluate whether or not the flow will separate, but it cannot predict separation location. These relationships are useful, but have extensive limitations that restrict the applicable applications. Therefore, in most cases, designing a flat-plate zero-pressure-gradient test condition is the preferred method in order to make use of these techniques. An additional limitation of these relationships is the obvious requirement that the flow be laminar, whereas most commonly encountered flows are turbulent. However, the flow over an airfoil operating ideally in cruise conditions is laminar for a period of time and then transitions to turbulence.

$$\delta_{99} = 4.93\sqrt{\frac{\nu x}{U}} \implies \frac{\delta_{99}}{x} = \frac{4.93}{\sqrt{Re_x}} \tag{3.19}$$

$$\delta^* = 1.721\sqrt{\frac{\nu x}{U}} \implies \frac{\delta^*}{x} = \frac{1.721}{\sqrt{Re_x}} \tag{3.20}$$

$$\theta = 0.664\sqrt{\frac{\nu x}{U}} \implies \frac{\theta}{x} = \frac{0.664}{\sqrt{Re_x}} \tag{3.21}$$

$$\tau_w = 0.332U^{3/2}\sqrt{\frac{\rho\mu}{x}} \implies C_f = \frac{0.664}{\sqrt{Re_x}} \implies F_D = \frac{0.664\rho U^2 l}{\sqrt{Re_l}} \tag{3.22}$$

3.3.2 Transition

Transition from laminar to turbulence may be caused by various forcing mechanisms or naturally as the laminar boundary layer becomes unstable. However, the location of the transition from turbulent to laminar is incredibly important for many flow applications, such as an airfoil. Since laminar flow has low shear characteristics, it is preferred in the favorable pressure gradient region of an airfoil; however, in the adverse pressure gradient region, turbulent flow, which opposes separation, is preferred in order to reduce devastating pressure drag. Therefore, the best drag characteristics occur when the flow transitions farther back on the airfoil. Transition can be trigged due to surface inconstancies such as surface roughness; change in surface geometry; vibrations; and other mechanisms, or as Reynolds number increases, the flow will become unsteady and transition naturally, which is dependent on the flow itself. Experimental flows are often tripped to turbulence by using a small wire or sandpaper grit to force the turbulent flow required in the experimental study.

3.3.3 Turbulent boundary layer

Leonardo De Vinci was one of the first to attempt to visualize and study turbulent flow, which is documented by his drawing of water pouring from a square channel (shown in Figure 3.1). This drawing and the observations made to produce it are still valid representations of what we know about turbulent flow today. De Vinci's drawing illustrates a chaotic swirl and the mixing of fluid with a structure consisting of consecutively smaller swirling structures. This drawing, from over 500 years ago, is a shockingly accurate representation of turbulent behavior that is defined today as a dissipative irregular diffusive flow which occurs in a continuum at high Reynolds numbers with three-dimensionally fluctuating vorticity elements [80]. The dissipative nature of turbulence is caused by viscous deformation and requires energy to resupply and support the flow. Without the ability to retain and increase energy

levels, turbulent flows would completely dissipate and re-laminarize. The irregularity in turbulent flows is one of the reasons that no straightforward turbulence solution exists. One of the most useful features of turbulence is its diffusiveness, which quickly mixes and can increase momentum, heat, and mass transfer in a flow. Flows are often designed to be turbulent for the purpose of utilizing this diffusive property. An important note to make is that turbulence is not a fluid property, but is a property of a flow; therefore, a fluid cannot be turbulent, but a flow can be. This is because the behavior of turbulent flows are not controlled by the molecular properties of a fluid. Flows of different fluids at high Reynolds numbers produce nearly identical turbulent behaviors despite having different molecular properties. Continuum physics is valid for turbulent flow conditions because all of the length scales involved are much larger than the molecular length scale. High Reynolds numbers are often required to produce turbulent flows. A laminar flow will transition to turbulent if a disturbance is present or if the Reynolds number is increased to the point of causing a flow disturbance. Large Reynolds numbers further complicate turbulence by introducing nonlinearities into the problem. The nature of turbulence is three-dimensional and made up of vortical features that fluctuate randomly - large vorticity elements mixing with small vorticity elements in all directions. It is important to understand that turbulence is not a complicated math problem that requires solely extensive arithmetic, but rather a mathematical understanding combined with an extensive understanding of a specific turbulent flow case that may lead to a necessary assumption. This fact is the reason multiple analysis methods exist and why different approaches are often used for different turbulence scenarios, such as the turbulent boundary layer, further complicating the problem by adding the viscous interaction with the wall.

The turbulent boundary layer is thicker and produces higher wall shear than that of a laminar boundary layer. However, the turbulent boundary layer can still be described in terms of the generic 99-percent of freestream velocity (Equation 3.23),

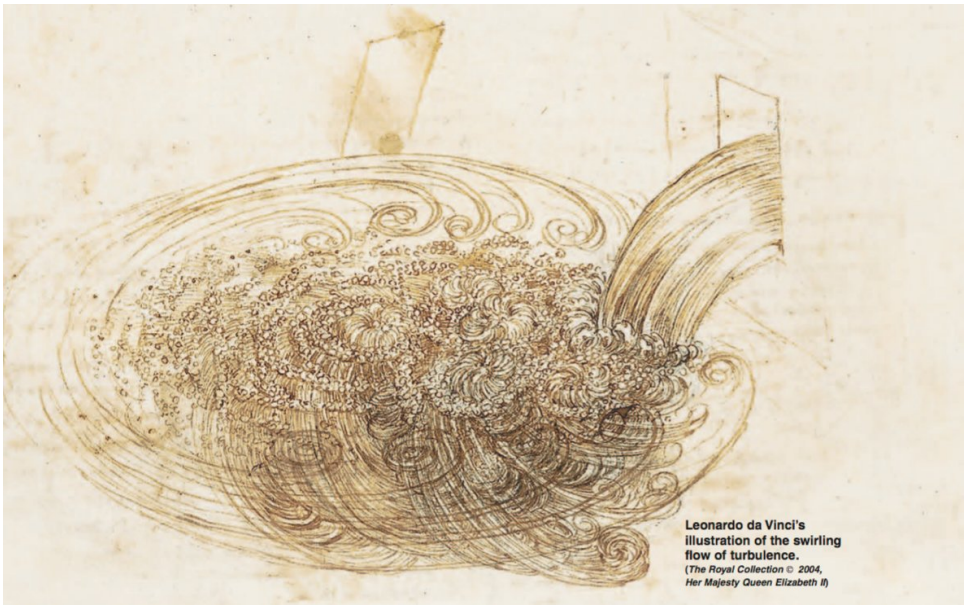

Figure 3.1: Leonardo da Vinci's illistration of the swirling flow of turbulence [81].

displacement (Equation 3.24), and momentum thicknesses (Equation 3.25) using their actual definitions, instead of the approximations for a laminar boundary layer discussed in Section 3.3.1. Additionally, the turbulent boundary layer has been experimentally shown to roughly scale in accordance with Equation 3.26 [82]. These equations can describe the boundary layer thickness, but a more useful parameter to evaluate the scales within the turbulent boundary layer is provided by the Law of the wall shown in Figure 3.2. This relationship compares a dimensionless velocity (Equation 3.27) as a function of the dimensionless wall-unit (Equation 3.28). The dimensionless velocity relates the local velocity as a function of "y" to friction velocity (Equation 3.29) or the shear stress at the wall. The wall-unit (Equation 3.28) is a function of distance from the wall scaled to wall shear divided by viscosity and represents a viscous length. For large Reynolds numbers, the Law of the wall has been reproduced experimentally and computationally with DNS results. The relationship is linear for wall-unit of less than five, which is known as the viscous sublayer, where the flow is dominated by viscous forces and behaves similarly to laminar flow. For wall-unit larger than thirty, the relationship follows a logarithmic law (Equation 3.31)

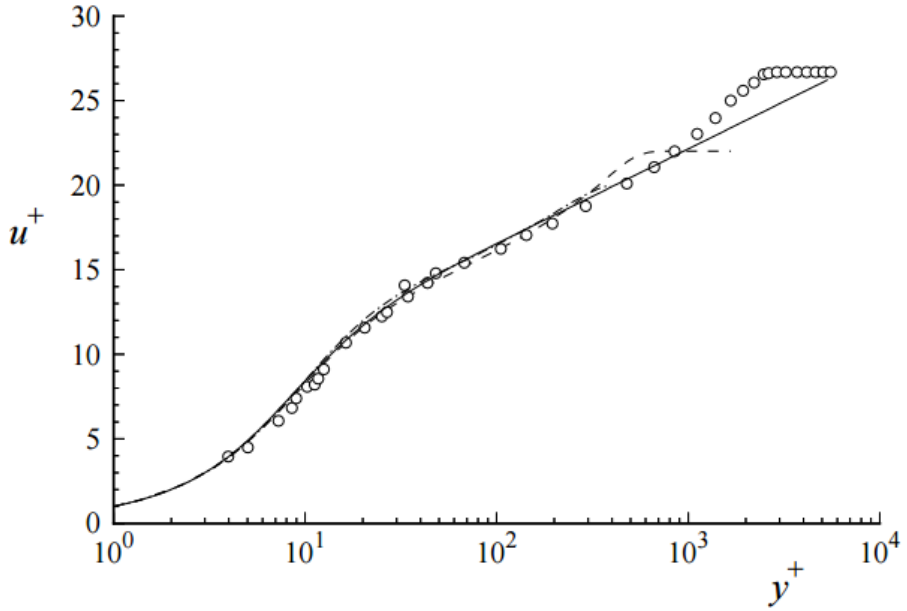

Figure 3.2: The Law-of-the-Wall (solid line) plotted with experimental results of Klebanoff (1955) [84] and DNS results of Spalart (1986) [85] and Kim et al. (1987) [86]; circles, dashed line, and dot-dashed line respectively [87].

for which the constants "k" and "C^+" are known for a smooth wall [83]. The log-law region represents where inertial forces and viscous forces are balanced. Outside of the log-law region, as wall-unit approaches 1000, the viscous effects become negligible. In the region between the viscous sublayer and the log-law region exists the buffer-layer (between five and thirty wall-unit), where the linear relationship (Equation 3.30) transitions to the log-law relationship.

$$\delta_{99} = \frac{u}{U} \tag{3.23}$$

$$\delta^* = \int_0^\infty \left(1 - \frac{u}{U}\right) dy \tag{3.24}$$

$$\theta = \int_0^\infty \frac{u}{U}\left(1 - \frac{u}{U}\right) dy \tag{3.25}$$

$$\delta = 0.37\frac{x}{Re_x^{1/5}} \tag{3.26}$$

$$u^+ = \frac{u}{u_\tau} \tag{3.27}$$

$$y^+ = \frac{yu_\tau}{\nu} \tag{3.28}$$

$$u_\tau = \sqrt{\frac{\tau_w}{\rho}} \tag{3.29}$$

$$u^+ = y^+ \tag{3.30}$$

$$u^+ = \frac{1}{k} * ln * y^+ + C^+ \tag{3.31}$$

3.4 Turbulent Statistics

A brief introduction to general turbulent statistics is provided based on the turbulent statistics presented and discussed in this work. The Reynolds decomposition breaks the instantaneous velocity component into two parts, the average velocity and the deviation from the average, known as the fluctuating term, as shown in Equation 3.32. This is the basis of the decomposition which leads to the Reynolds averaged Naiver-Stokes equation, and the average of the fluctuating velocity term is zero by definition. It is often useful to evaluate the variance (Equation 3.33) and covariance (Equation 3.34) of the velocity field to compare with previous experimental and computational work. These terms are the Reynolds stresses which make up the Reynolds stress tensor (Equation 3.35) in the RANS equations, and they correlate with turbulent production in the boundary layer. Many additional turbulent statistical parameters

exist, such as skewness, kurtosis, probability density, or correlation functions, which are not discussed in this paper but may be of future value to the work presented here.

$$u = U + u' \tag{3.32}$$

$$u'u' = \frac{\Sigma(u-U)^2}{N} \tag{3.33}$$

$$u'v' = \frac{\Sigma(u-U)(v-V)}{N} \tag{3.34}$$

$$T = \begin{bmatrix} u'u' & u'v' & u'w' \\ v'u' & v'v' & v'w' \\ w'u' & w'v' & w'w' \end{bmatrix} \tag{3.35}$$

3.5 Partical Image Velocimetry

Particle image velocimetry (PIV) is an experimental technique which provides instantaneous velocity data of the flow field within the illuminated region and camera frame. This is a powerful technique in comparison to dye flow visualization which produce only qualitative results and then requires extensive labor or intensive modeling to pull out quantitative data form images. The PIV experimental system captures flow field image pairs of illuminated particles in the test section. This is accomplished with the use of a high-powered laser capable of producing at least two high-intensity pulses in succession in order to capture two images within a relatively small prescribe time. The camera and the laser must be timed accordingly, and the laser beam must be focused and manipulated with optics to produce a thin 2D sheet, which will become the velocity vector field plane. For time resolved instantaneous PIV measurements, the image pairs are taken at higher-speed intervals relative to the fluid velocity. Time

resolved PIV requires a high-speed laser and a high-speed camera, but produces a time-resolved flow field that provides information about how the flow evolves with time. Non-time resolved PIV measurements still take an image pair in rapid succession, but have a longer wait time in-between capturing the next sequential image pair. This increased time between collecting the sequential image pairs limits the PIV measurements to instantaneous velocity field snap shots that are not directly comparable without averaging over many instances. This distinction is important for the work presented here because PIV measurements were taken with two different PIV systems, high-resolution and high-speed, capable of taking higher spatially resolved but non-time resolved or lower spatially resolved but time resolved PIV measurements respectively.

After the image pairs are taken, they are processed by interrogating small portions, or windows, of the image pairs. The algorithm attempts to identify the most probable displacement of the interrogation window, rather than the individual particles. This requires that the camera be calibrated prior to capturing the image pairs to provide a pixel-to-length scale calibration, which is used to convert the interrogation widow displacement in terms of the physical length traversed within the illuminated laser plane. Additionally, the time between capturing the image pairs is used to define the time required for the window displacement to occur. Evaluating numerous windows with a prescribed amount of overlap within a single image pair and combining the most likely displacement over the known time, produces a velocity vector field for a single instance in time. Figure 3.3 illustrates a simplistic example of the interrogation between the two image pairs, in which the first image is evaluated with a smaller window and identifies a grouping of particles and then locates the most similar grouping of particles in the second image using a larger interrogation window. It should be noted that this example is simplified to only translational motion, but this method also identifies rotational motion. Spatial cross-correlation algorithms

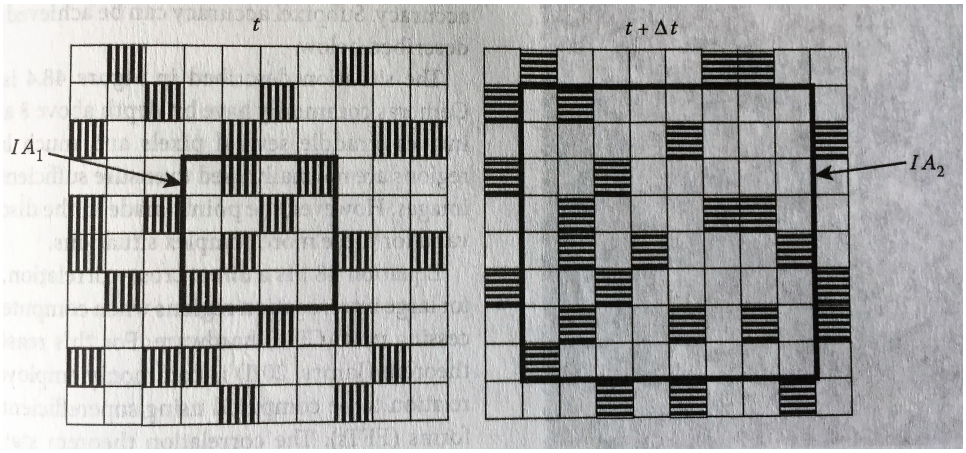

Figure 3.3: Example of the interrogation of an image pair. The squares represent pixels, darkened squares are particles, and the thick boarded boxes represent the interrogation window sizes ("IA_1" and "IA_2"). Note that the flow for this example image pair is shown to traverse two pixels down and two pixels to the left from time "t" to time "$t + \Delta t$" [90].

are used to determine the most probable displacement between image pairs and are discussed in detail by Westerweel, (1997) and Raffel et al. (2007) [88] [89].

3.6 RANS, SST K-Omega Model

The Reynolds averaged Naiver-Stokes (RANS) equations are the basis for many of the simulations presented in this study. Therefore, a brief explanation and mathematical description of the RANS K-Omega turbulence model is provided. Starting from the Naiver-Stokes Momentum equation (3.16), applying the Reynolds decomposition (Equation 3.32), and averaging the entire equation results in the RANS momentum equation (Equation 3.36). The decomposition and averaging produced a nearly identical equation, with one additional term, the Reynold stress tensor (Equation 3.35). This tensor adds additional unknowns to the system of equations and prohibits their closure; therefore, the Reynolds stress tensor is often modeled. RANS turbulence models solve this closure problem by modeling the Reynolds stress tensor with the Boussinesq approximation (Equation 3.37), which attempts to model the momentum transfer from turbulent eddies by invoking an eddy viscosity (also referred to as turbulent viscosity) term. This approach is similar to the method of modeling momentum

transfer with dynamic viscosity. The difference being that the viscosity of a fluid is a molecular property of a fluid, mostly a function of temperature, as opposed to the turbulent viscosity, which is a property of a turbulent flow phenomena that is a function of many different flow properties and can vary between types of flow (i.e. wall-bounded, compressible, free shear, etc.).

$$\frac{\partial}{\partial t}\left(\rho\overline{u}\right) + \nabla \cdot [\rho\overline{u}(\bar{u})] = -\nabla \cdot \overline{p} + \nabla \cdot (T_t) + F_b \tag{3.36}$$

$$T_t = 2\mu_t S - \frac{2}{3}(\mu_t \nabla \cdot \overline{u}) \tag{3.37}$$

The mathematical description of the turbulent viscosity is where RANS turbulent models differentiate themselves from one another. The K-Omega variant is a two equation model, which defines the turbulent viscously with turbulent kinetic energy and specific dissipation rate (Equation 3.38). This model therefore adds two additional equations to the system, the kinetic energy transport equation (Equation 3.39) and the specific dissipation rate transport equation (Equation 3.40). Additionally, the SST variant of the K-Omega model, which incorporates a set of model coefficients, corrections for sensitivity to inlet and freestream conditions, a correction for free shear flows, a correction for compressibility effect, and a correction of low Reynolds number flows, utilizing two blending functions (Equation 3.41) and (Equation 3.42). This function allows the model to benefit from the improved accuracy of the K-Omega definition of turbulent viscosity in the boundary layer while effectively reverting to a k-epsilon definition of turbulent viscosity (Equation 3.43) in the freestream, where the K-Omega model performance diminishes [91]. The production terms in these two additional equations are defined in (Equation 3.44), where turbulent, buoyancy, nonlinear, and specific dissipation production terms are defined in equations 3.45, 3.46, 3.47, and 3.48 respectively, and the cross-diffusion term is given as Equation 3.49. All

of these equations include various correction factors and coefficients which are identified in Table 3.1. This turbulence model's mathematical description was included in this section to ensure that the model is understood, since it will be referenced in the additional turbulence model sections which build upon the concepts presented here and in order to highlight the complexity of the models and the constants required to close the system of equations, which are intended to be tuned for specific flow applications. The mathematical explanations presented here were in reference to Star-CCM+ documentation [92].

$$\mu_t = \rho k T \tag{3.38}$$

$$\frac{\partial}{\partial t}(\rho k) + \nabla \cdot (\rho k \overline{u}) = \nabla \cdot [(\mu + \sigma_k \mu_t)\nabla k] + P_k - \rho \beta^* f_{\beta^*}(\omega k - \omega_0 k_0) + S_k \tag{3.39}$$

$$\frac{\partial}{\partial t}(\rho \omega) + \nabla \cdot (\rho \omega \overline{u}) = \nabla \cdot [(\mu + \sigma_\omega \mu_t)\nabla \omega] + P_\omega - \rho \beta f_\beta(\omega^2 - \omega_0^2) + S_\omega \tag{3.40}$$

$$F_1 = tanh\Bigg(\Big[min\Big(max\Big(\frac{\sqrt{k}}{0.09\omega d}, \frac{500\nu}{d^2\omega}\Big), \frac{2k}{d^2 C D_{k\omega}}\Big)\Big]^4\Bigg) \tag{3.41}$$

$$F_2 = tanh\Bigg(\Big(max\Big(\frac{2\sqrt{k}}{\beta^*\omega d}, \frac{500\nu}{d^2\omega}\Big)\Big)^2\Bigg) \tag{3.42}$$

$$1 \tag{3.43}$$

$$P_k = G_k + G_{nl} + G_b, P_\omega = G_\omega + D_\omega \tag{3.44}$$

$$G_k = \mu_t f_c S^2 - \frac{2}{3}\rho k \nabla \cdot \overline{u} - \frac{2}{3}\mu_t (\nabla \cdot \overline{u})^2 \tag{3.45}$$

$$G_b = \beta \frac{\mu_t}{Pr_t} (\nabla \overline{T} \cdot g) \tag{3.46}$$

$$G_{nl} = \nabla \cdot \overline{u} : (T_{t,NL}) \tag{3.47}$$

$$G_\omega = \rho\gamma \left[\left(S^2 - \frac{2}{3} \left(\nabla \cdot \overline{u} \right)^2 - \frac{2}{3}\omega \nabla \cdot \overline{u} \right] \tag{3.48}$$

$$D_\omega = 2\rho(1 - F_1)\sigma_{\omega_2} \frac{1}{\omega} \nabla k \cdot \nabla \omega \tag{3.49}$$

3.7 LES, Dynamic Smagorinsky SGS Model

The large eddy simulation (LES) momentum equation is very similar to the previously discussed RANS equation, However, the key difference in the derivation is that, instead of performing the Reynold decomposition and averaging, filtering is accomplished in terms of Equation 3.50. The filtered parameters are defined by a function of cell size as shown in Equation 3.51, which is either determined by a prescribed constant or in the case of the dynamic Smagorinsky subgrid scale (SGS) model, computed dynamically depending upon the local size of the grid compared to the local scale of the motion. The filtering results in a nearly identical final Equation 3.52, where, instead of averaged, terms there are filtered terms. It is important to note that a new stress tensor is also produced, similar to the RANS decomposition, but now representing the subgrid scale stresses. The LES method uses the same Boussineq approximation discussed previously with a similar form of the equation for the stress tensor, but substitutes the filtered velocity for the averaged velocity (Equation 3.53).

Parameter	Value or Description
α_1	0.31
α^*	$F_1\alpha_1^* + (1 - F_1)\alpha_2^*$
α_1^*	1
α_2^*	1
β	$F_1\beta_1 + (1 - F_1)\beta_2$
β_1	0.075
β_2	0.0828
β^*	$F_1\beta_1^* + (1 - F_1)\beta_2^*$
β_1^*	0.09
β_2^*	0.09
γ	$F_1\gamma_1 + (1 - F_1)\gamma_2$
γ_1	$\frac{\beta_1}{\beta^*} - \sigma_{\omega_1}\frac{k^2}{\sqrt{\beta^*}}$
γ_2	$\frac{\beta_2}{\beta^*} - \sigma_{\omega_2}\frac{k^2}{\sqrt{\beta^*}}$
k	0.41
σ_k	$F_1\sigma_{k_1} + (1 - F_1)\sigma_{k_2}$
σ_{k_1}	0.85
σ_{k_2}	1
σ_ω	$F_1\sigma_{\omega_1} + (1 - F_1)\sigma_{\omega_2}$
σ_{ω_1}	0.5
σ_{ω_2}	0.856
C_T	0.6

Table 3.1: RANS SST K-Omega correction factors and coefficients

The Boussineq approximation introduces the turbulent viscosity term, which is defined based on the subgrid scale turbulence model implemented.

The dynamic Smagorinsky subgrid scale model defines the turbulent viscosity (Equation 3.54) and the previously mentioned filtering applied to the momentum equation in terms of the dynamically computed grid-filter-width (Equation3.55). This is accomplished with the test-filtered parameter (Equation 3.56), for which "n" is the cell number with 0 being the current (or center) cell and cells 1 to "N" are its boundary sharing cells, as depicted in Figure 3.4. The grid filter length "L_{ij}" (Equation 3.57) and the tensor "M_{ij}" (Equation 3.58) define the model coefficient "C_s" (Equation 3.59), which is used to compute the grid filter width, "Δ" (Equation 3.55). The grid filter width defines the local dynamically filtered flow properties (Equation 3.50) in the LES momentum Equation 3.51 and defines the local dynamically calculated turbulent viscosity value (Equation 3.54). The user must define the filter width ratio and can define minimum and maximum values of the model coefficient as listed in table 3.2. Proper configuration of the dynamic Smagorinsky model can yield results that approach those obtained from DNS and experimental work; however, the configuration is heavily dependent upon the grid size, application, and discretization. Ideally, if the grid resolution is adequately increased to fully resolve all the turbulent scales, then the dynamic model reverts to a DNS, or unfiltered Naiver-Stokes, solution [87]. However, lower-order discretization schemes result in a "numericall-filter", which was encountered in the work presented here and is discussed in detail by Denaro (2011) [93]. It is important to note that, without experimental data to compare with simulation results, it is impossible to evaluate the effect of filter width, turbulent viscosity, or discretization scheme on the computational solution. The mathematical explanations presented here were in reference to Star-CCM+ documentation [92].

$$Q = \tilde{Q} + Q' \tag{3.50}$$

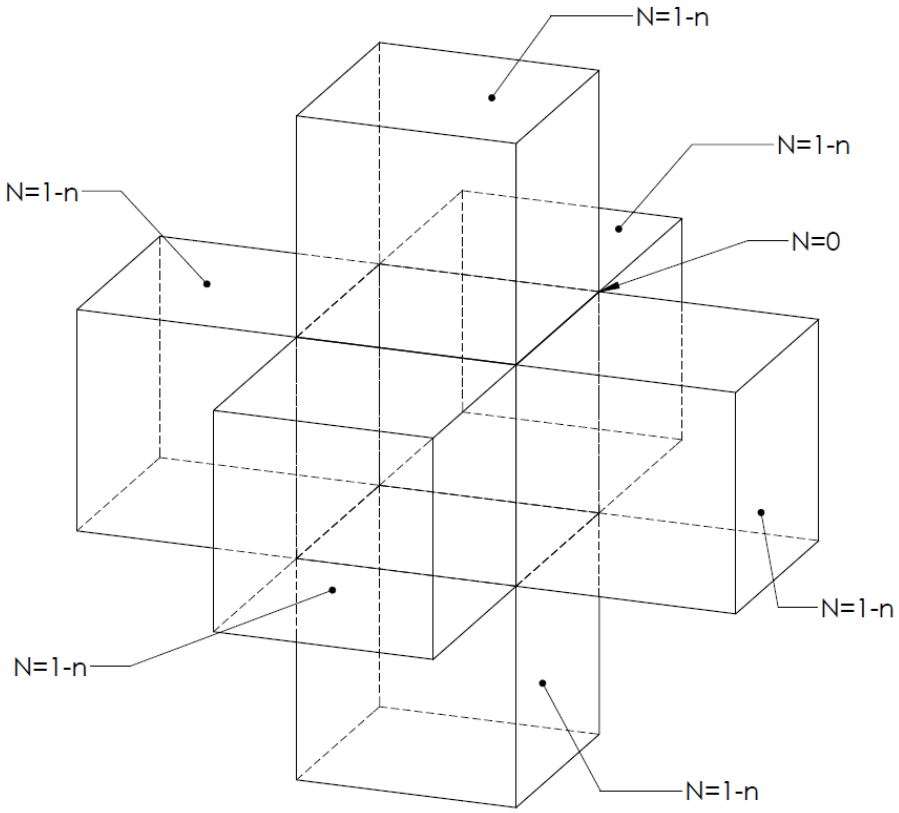

Figure 3.4: Illustration of test filter equation reference values of "N" ("N" is equal to six for this simple case).

Parameter	Value or Description
$\widehat{L}/\tilde{L}$	2

Table 3.2: LES, dynamic Samgorinsky SGS correction factors and coefficients

$$\tilde{Q} = \int\int\int_{-\infty}^{+\infty} G(x - x', \Delta) Q dx \tag{3.51}$$

$$\frac{\partial}{\partial t}\Big(\rho\tilde{u}\Big) + \nabla \cdot [\rho\tilde{u}(\tilde{u})] = -\nabla \cdot \tilde{p} + \nabla \cdot (T_t) + F_b \tag{3.52}$$

$$T_t = 2\mu_t S - \frac{2}{3}(\mu_t \nabla \cdot \tilde{u} + \rho k) \tag{3.53}$$

$$\mu_t = \rho \Delta^2 S \tag{3.54}$$

$$\Delta^2 = C_s^2 \, V^{\frac{2}{3}} \tag{3.55}$$

$$\widehat{\tilde{Q}} = \frac{1}{\Sigma_{n=0}^{N} V_n} \sum_{n=1}^{N} \tilde{Q}_n \, V_n \tag{3.56}$$

$$L_{ij} = \tilde{u_i}\widehat{\tilde{u}_j} - \widehat{\tilde{u}_i}\widehat{\tilde{u}_j} \tag{3.57}$$

$$M_{ij} = 2\tilde{L}^2(|\tilde{S}|\widehat{\tilde{S}_{ij}} - \frac{\widehat{L}^2}{\tilde{L}^2}|\widehat{\tilde{S}}|\widehat{\tilde{S}_{ij}}) \tag{3.58}$$

$$C_S^2 = \frac{L_{ij}M_{ij}}{M_{ij}M_{ij}} \tag{3.59}$$

3.8 IDDES, RANS SST K-Omega Model

The detached eddy simulation (DES) model attempts to find balance between the LES model, which excels in separated, free shear, or jet type flows, and the RANS model, which excels in steady flows. The RANS and LES formulations, which were previously discussed in Sections 3.6 and 3.7, will tie directly into the DES model formulation. As mentioned previously, the form of the LES and RANS momentum equations are similar in nature; Equations 3.60 and 3.61 show the two for comparison, highlighting the differences and similarities between them. The two can be combined into one momentum equation (Equation 3.62), where the modeled stress term is defined in Equation 3.63. Note that as damping function and the ratio of local grid size to turbulent length scale trend toward one, the stress term approached the RANS Reynold stress definition. The damping function is defined by the improved delayed detached eddy simulation (IDDES) variant formulation of the DES model [94]. The IDDES formulation modifies the RANS SST K-Omega definition of spacific dissipation rate by defining it by Equation 3.64 and substituting it into Equation 3.40, where the hybrid length scale is defined by Equation 3.65. This model then incorporates a blending function (Equation 3.66), an elevating function (Equation 3.67), and an alternate mesh length scale (Equation 3.68). All of the user defined model coefficients are given in table 3.3. The final result is a model which blends between a wall-modeled LES model and the RANS SST K-Omega model depending on the local grid scale compared to the local scale of the motion. If the cell refinement was increased to the point of computing the LES simulation result over the domain, then this would effectively be a wall-modeled LES simulation. However, the IDDES model is intended to be used to resolve the larger scale turbulent motion and blend down to a non-eddy resolving RANS type solution near the wall. This approach attempts to reduce cell refinement requirements associated with the wall-model LES approach, but still give accurate resolved flow results away from the wall. The mathematical

explanations presented here were in reference to Star-CCM+ documentation [92].

$$\frac{\partial}{\partial t}\Big(\rho\overline{u}\Big) + \nabla \cdot [\rho\overline{u}(\overline{u})] = -\nabla \cdot \overline{p} + \nabla \cdot (T_t^{RANS}) + F_b \tag{3.60}$$

$$\frac{\partial}{\partial t}\Big(\rho\tilde{u}\Big) + \nabla \cdot [\rho\tilde{u}(\tilde{u})] = -\nabla \cdot \tilde{p} + \nabla \cdot (T_t^{LES}) + F_b \tag{3.61}$$

$$\frac{\partial}{\partial t}\Big(\rho\breve{u}\Big) + \nabla \cdot [\rho\breve{u}(\breve{u})] = -\nabla \cdot \breve{p} + \nabla \cdot (T_t^{model}) + F_b \tag{3.62}$$

$$T_t^{model} = f_\Delta \frac{\Delta}{l_k} T_t^{RANS} \tag{3.63}$$

$$\tilde{\omega} = \frac{\sqrt{k}}{l_{HYBRID}\beta^* f_{b^*}} \tag{3.64}$$

$$l_{HYBRID} = \tilde{f}_d(1 + f_e)l_t + (1 - \tilde{f}_d)C_{DES}\Delta_{IDDES} \tag{3.65}$$

$$f_B = min[2e^{-9\alpha^2}, 1] \tag{3.66}$$

$$f_e = max[(f_{e1} - 1), 0]\psi f_{e2} \tag{3.67}$$

$$\Delta_{IDDES} = min(max(0.15d, 0.15\Delta, \Delta_{min}), \Delta) \tag{3.68}$$

3.9 CFD Simulation Solution Evaluation

A simulation is considered stable if the iterative results either produce less error, on average, over the course of many iterations or if the error is consist as iterations are

Parameter	Value or Description
α	$0.25 - \frac{d}{\Delta}$
f_{e1}	$2e^{-11.09\alpha^2}$ if $\alpha \geq 0$, or $2e^{-9\alpha^2}$ if $\alpha < 0$
f_{e2}	$1 - max(f_t, f_l)$
f_t	$tanh[(C_t^2 r_{dt})^3]$
f_l	$tanh[(C_l^2 r_{dl})^{10}]$
r_{dt}	$\frac{\nu_t}{\sqrt{\nabla v : \nabla v^T k^2 d^2}}$
r_{dl}	$\frac{\nu}{\sqrt{\nabla v : \nabla v^T k^2 d^2}}$
$\tilde{f}_d$	$max((1 - f_{dt}), f_B)$
f_{dt}	$1 - tanh[(C_{dt} r_{dt})^3]$
C_{DES}	0.78
C_{dt}	20
C_l	5
C_t	1.87

Table 3.3: IDDES, RANS SST K-Omega correction factors and coefficients

computed. The simulation is unstable if the error increases as iterations are computed. This is the same as stating that a stable solution is one that does not diverge from a solution, where convergence is the tendency of the simulation to approach the exact solution as the differential volume of integral equation approaches zero [95]. This is often difficult to evaluate, and the general method requires simulating the flow over successively finer grids and evaluating the value that the result approaches. Once the result is invariant to further grid refinements, it is said to be grid-independent. The distinction is made between a stable and a converged solution because an iterative method can be stable but not converge. This points to the accuracy of the stable numerical simulation. If a simulation's result is not physically grounded, then no level of grid independence or stability will justify its result. Therefore, the simulation's results cannot be evaluated solely on the stability of the method or even the convergence to a solution, if the approached solution is not known to be accurate, physically. There are three categories of simulation error; model error, iterative error, discretization error, which is the difference between the modeled equation results, discretized temporal or spatial equation results, and iterative results and the exact

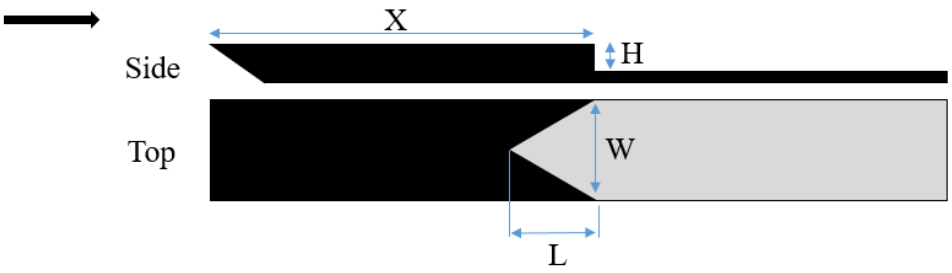

Figure 3.5: Illustration of "X", "H", "W", and "H" geometric variables for CVG scaling

equation results respectively, assuming that no other error exists between them [95]. Note that all of the simulation solution properties presented here assume that the exact solution is known and available for comparison with the simulation results. This is an important realization regarding CFD simulation work, without an adequate means of evaluating the simulation results in comparison to the exact physical result, the quality or accuracy of the simulation is in question. Validation is the process of quantifying the accuracy of the simulation solution by comparing it to experimental, or in simplistic cases, the analytical solution, which is a critical aspect of any CFD simulation strategy.

3.10 Scaling Approaches

The scaling options used in this invesitgation are based on re-evaluating the various parameters deemed dominate or important, those which produced different sets of scaling laws depending on the assumptions made to reduce the total set of parameters given in Table 3.4 (geometric variables are shown in Figure 3.5).

3.10.1 Reynolds Number Based on Downstream Distance Scaling

This scaling assumes that the local balance between inertial and viscous effects are dominant, and as such, ignores all of the geometric parameters of the CVG, pressure gradient, boundary layer parameters, and wall shear stress, only considering the parameters in Table 3.5. The process of producing the scaling law is shown below

Parameter	Description
X	distance in the x-direction from the leading edge to the step
H	Step height
L	CVG triangular height (in the x-direction)
W	CVG triangular width)(in the z-direction)
U	Freestream velocity
ρ	density
ν	Kinematic viscosity
μ	Dynamic viscosity
τ_w	Wall shear stress
δ	Generic boundary layer
δ^*	Boundary layer displacement thickness
θ	Boundary layer momentum thickness
ω	Vorticity
dp/dx	Pressure gradient in the x-direction

Table 3.4: Parameters for scaling

	X $[m]$	U $[\frac{m}{s}]$	ρ $[\frac{kg}{m^3}]$	μ $[\frac{kg}{sm}]$
M	0	0	1	1
L	1	1	-3	-1
T	0	-1	0	-1

Table 3.5: Dimensional analysis for Re_X scaling approach

(Equation 3.69, 3.70, and 3.71).

$$\pi_1 = \frac{\rho X U}{\mu} \tag{3.69}$$

$$\frac{\rho X U}{\mu} = \phi = constant \tag{3.70}$$

$$\frac{\rho_p X_p U_p}{\mu_p} = \frac{\rho_m X_m U_m}{\mu_m} \tag{3.71}$$

3.10.2 Reynolds Number Based Step Height Scaling

This scaling assumes that the balance inertial and viscous effects relative to the step height are dominant, and therefore, neglects the CVG triangular dimensions, pressure

	$H\ [m]$	$U\ [\frac{m}{s}]$	$\rho\ [\frac{kg}{m^3}]$	$\mu\ [\frac{kg}{sm}]$
M	0	0	1	1
L	1	1	-3	-1
T	0	-1	0	-1

Table 3.6: Dimensional analysis for Re_H scaling approach

	$H\ [m]$	$U\ [\frac{m}{s}]$	$\rho\ [\frac{kg}{m^3}]$	$\mu\ [\frac{kg}{sm}]$	$\tau_w\ [\frac{N}{m^2}]$
M	0	0	1	1	1
L	1	1	-3	-1	-2
T	0	-1	0	-1	1

Table 3.7: Dimensional analysis for τ_w scaling approach

gradient, boundary layer parameters, and wall shear stress and only considers the parameters in Table 3.6. The process of producing the scaling law is shown below (Equation 3.72, 3.73, and 3.74).

$$\pi_1 = \frac{\rho H U}{\mu} \tag{3.72}$$

$$\frac{\rho H U}{\mu} = \phi = constant \tag{3.73}$$

$$\frac{\rho_p H_p U_p}{\mu_p} = \frac{\rho_m H_m U_m}{\mu_m} \tag{3.74}$$

3.10.3 Wall Shear Stress Scaling

This scaling assumes that both the wall shear stress and CVG height are dominate, and therefore, neglects the CVG triangular dimensions, pressure gradient, and boundary layer parameters and only considers the parameters in Table 3.7. The process of producing the scaling law is shown below (Equation 3.75, 3.76, 3.77, 3.78, and 3.79).

$$\pi_1 = \frac{H\rho}{\mu}\sqrt{\frac{\rho}{\tau_w}}, \pi_2 = \frac{\tau_w}{\rho U^2} \tag{3.75}$$

	H $[m]$	X $[m]$	U $[\frac{m}{s}]$	ρ $[\frac{kg}{m^3}]$	μ $[\frac{kg}{sm}]$	θ $[m]$
M	0	0	0	1	1	0
L	1	1	1	-3	-1	1
T	0	0	-1	0	-1	0

Table 3.8: Dimensional analysis for θ scaling approach

$$\frac{H\rho}{\mu}\sqrt{\frac{\rho}{\tau_w}} = \phi\left(\frac{\tau_w}{\rho U^2}\right) \tag{3.76}$$

$$C_f = \frac{\tau_w}{\frac{1}{2}\rho U^2} \tag{3.77}$$

$$\frac{H\rho}{\mu}\sqrt{\frac{\rho}{\tau_w}} = \frac{H}{l_\nu} = y^+ = constant \tag{3.78}$$

$$\frac{H_p\rho_p}{\mu_p U_p}\sqrt{\frac{1}{C_{f_p}}} = \frac{H_m\rho_m}{\mu_m U_m}\sqrt{\frac{1}{C_{f_m}}} \tag{3.79}$$

3.10.4 Momentum Thickness Scaling

This scaling assumes that the CVG height relative to the boundary layer thickness is dominate, and therefore, neglects the CVG triangular dimensions, pressure gradient, and wall shear stress and only considers the parameters in Table 3.8. The process of producing the scaling law is shown below (Equation 3.80, 3.81, 3.82, 3.83, and 3.84).

$$\pi_1 = \frac{H}{\theta}, \pi_2 = \frac{\theta}{X}, \pi_3 = \frac{\rho XU}{\mu} \tag{3.80}$$

$$\frac{H}{\theta} = \phi\left(\frac{\theta}{X}, \frac{\rho XU}{\mu}\right) \tag{3.81}$$

$$\theta = \frac{0.664X}{\sqrt{Re_X}} = \frac{0.664X}{\sqrt{\frac{\rho XU}{\mu}}} \tag{3.82}$$

	ω $[/s]$	H $[m]$	W $[m]$	L $[m]$	δ $[m]$	U $[\frac{m}{s}]$	ρ $[\frac{kg}{m^3}]$	ν $[\frac{m^2}{s}]$	$\frac{dp}{dx}$ $[\frac{kg}{s^2m^2}]$
M	0	0	0	0	0	0	1	0	1
L	0	1	1	1	1	1	-3	2	-2
T	-1	0	0	0	0	-1	0	-1	-2

Table 3.9: Dimensional analysis for Geometric and dp/dx scaling approach

$$\frac{H}{\theta} = constant \tag{3.83}$$

$$\frac{H_p\sqrt{\frac{\rho_p X_p U_p}{\mu_p}}}{X_p} = \frac{H_m\sqrt{\frac{\rho_m X_m U_m}{\mu_m}}}{X_m} \tag{3.84}$$

3.10.5 Geometric Pressure Gradient Scaling

This scaling assumes both that the CVG geometry (width and length) scales with step height and that the step heigth is related to the boundary layer thickness, viscous to inertial effects, and pressure gradient, and therefore, neglects the wall shear stress and only considers the parameters in Table 3.9. The process of producing the scaling law is shown below (Equation 3.85, 3.86, 3.87, 3.88, 3.89, 3.90, and 3.91).

$$\pi_1 = \frac{\omega H}{U}, \pi_2 = \frac{\delta}{H}, \pi_3 = \frac{UH}{\nu}, \pi_4 = \frac{dp}{dx}\frac{H}{\rho U^2}, \pi_5 = \frac{W}{H}, \pi_6 = \frac{L}{H} \tag{3.85}$$

$$\frac{\omega H}{U} = \phi\left(\frac{\delta}{H}, \frac{UH}{\nu}, \frac{dp}{dx}\frac{H}{\rho U^2}, \frac{W}{H}, \frac{L}{H}\right) \tag{3.86}$$

$$\frac{L}{H} = constant \tag{3.87}$$

$$\frac{W}{H} = constant \tag{3.88}$$

$$\frac{dp}{dx} \implies \delta^* = C_1 \frac{\nu X}{U} = C_2 \delta \tag{3.89}$$

$$C_2 = \frac{U\delta^*}{\nu}\frac{1}{\pi_2\pi_3} = \frac{Re_{\delta^*}}{\pi_2\pi_3} \implies \frac{Re_{\delta^*}}{Re_H}\frac{H}{\delta} = constant \tag{3.90}$$

$$\frac{Re_{\delta^* p}}{Re_{H_p}}\frac{H_p}{\delta_p} = \frac{Re_{\delta^* m}}{Re_{H_m}}\frac{H_m}{\delta_m}, \frac{W_p}{H_p} = \frac{W_m}{H_m}, \frac{L_p}{H_p} = \frac{L_m}{H_m} \tag{3.91}$$

Chapter 4

Experimental

4.1 Edge Aerodynamix Data and Previous Work

4.1.1 Flight Test Platforms

Edge Aerodynamix has a fleet of aircraft specifically for flight tests purposes, of which only three will be included here. The first is the Boeing 737-500 Aircraft, which is used for fuel efficiency testing with and without the CVG device applied. This is a transonic transport category aircraft powered by two turbofan engines and operates under the conditions listed in Table 4.1. The second is a Piper Cherokee, Arrow model, which provides a subsonic test platform for wall shear testing. This aircraft seats four, is powered by a single reciprocating prop engine, and operates under the conditions listed in Table 4.2. The third is a SOKO G-2 Galeb, which is a higher-speed wall shear stress test platform. The Soko G-2 Galeb is a two-seat Yugoslavian trainer jet powered by a single turbojet engine, for which properties are provided in Table 4.3.

4.1.2 Fuel Efficiency and Shock Stability

Results from Edge Aerodynamix fuel efficiency testing are key to insuring that the CVG device is worth investigating all together. The fuel efficiency testing is accomplished with the Boeing 737-500 flight test platform because this was the initial aircraft of interest and the first CVG application to be approved by multiple regulatory agencies. Therefore, the 737-500 flight test data is the most established fuel

Parameter	Value	Unit
H	~ 0.367	mm
X	~ 800 *to* 400	mm
$alt.$	$\sim 10,000$	m
ρ	~ 0.414	kg/m^3
μ	$\sim 1.46 \times 10^{-5}$	$Pa\text{-}s$
ν	$\sim 3.53 \times 10^{-5}$	m^2/s
U	~ 230	m/s
Re_H	$\sim 2,400$	
Re_X	~ 2.5 *to* 5.0×10^6	
$Mach$	~ 0.74 *to* 0.78	

Table 4.1: Boeing 737-500 flight properties.

Parameter	Value	Unit
H	~ 0.367	mm
L	~ 20 *to* 45	mm
W	~ 10 *to* 30	mm
X	~ 125 *to* 250	mm
$alt.$	$\sim 1,000$	m
ρ	~ 1.17	kg/m^3
μ	$\sim 1.77 \times 10^{-5}$	$Pa\text{-}s$
ν	$\sim 1.51 \times 10^{-5}$	m^2/s
U	~ 60	m/s
Re_H	$\sim 1,454$	
Re_X	~ 5.0 *to* 10.0×10^5	
$Mach$	~ 0.18	

Table 4.2: Piper Cherokee flight properties.

Parameter	Value	Unit
H	~ 0.367	mm
L	$\sim 20\ to\ 45$	mm
W	$\sim 10\ to\ 30$	mm
X	$\sim 125\ to\ 250$	mm
$alt.$	$\sim 4,000$	m
ρ	~ 0.819	kg/m^3
μ	$\sim 1.66 \times 10^{-5}$	$Pa\text{-}s$
ν	$\sim 2.03 \times 10^{-5}$	m^2/s
U	~ 200	m/s
Re_H	$\sim 3,621$	
Re_X	$\sim 1.3\ to\ 2.5 \times 10^6$	
$Mach$	~ 0.62	

Table 4.3: SOKO G-2 Galeb flight properties.

efficiency data for the CVG device. Extreme care is taken by Edge Aerodynamix to account for every factor that may effect or skew the results of fuel consumption testing, including center of gravity loading, quality of freestream flow, and constancy of air properties between tests. Numerous fuel efficiency tests have been conducted very late in the evening and into the early morning to mitigate poor flow quality. Fuel efficiency comparisons consist of carrying out multiple flights with the CVG and without the CVG equipped. Results from these tests are provided in Figure 4.1. These flight test results indicate a significant reduction in fuel consumption, which suggests that something significant occurs when aircraft are equipped with the CVG.

During these fuel consumption tests, the behavior of the shock was observed by taking video of the shock wave from inside the cabin, when lighting conditions permitted. The observed behavior of the shock suggested that the CVG have a noticeable effect on shock stability. Figure 4.2 is an example of shock visualizations during baseline fuel flights and Figure 4.3 shows instantaneous frames (0.1s between them) taken from the videos without CVG equipped. These results, compared to observations with the CVG device installed, indicated that the shock is more stable with the CVG than without. This is a significant observation because it offers a possible explana-

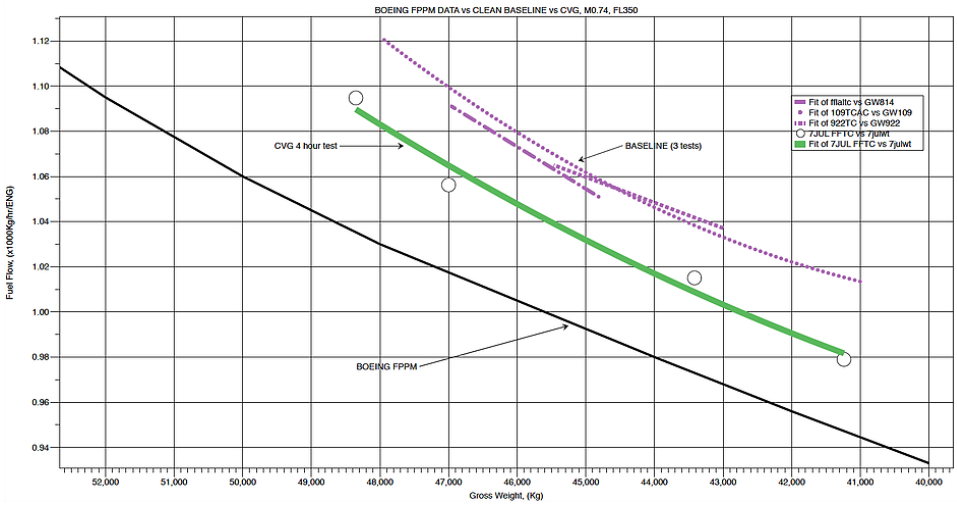

Figure 4.1: Results of fuel consumption flight testing by Edge Aerodynamix (Flight Planning and Performance Manual (FPPM))[9].

tion for the drag reduction mechanism. If the transonic shock oscillates during normal operation, then stabilizing it would have an effect on the wake drag. However, without more testing it is not possible to draw any conclusions about whether the shock stability is the source of the drag reduction or simply an added benefit of the drag reduction mechanism. A brief exploration of this proposed mechanism is discussed further in the Section 6.2

4.1.3 Wall Shear Testing

Wall shear visualizations of the CVG equipped Piper Cherokee, Arrow model, were used as comparison when evaluating the results of the work done at Oklahoma State University. These flight test results were of interest because the OSU wind and water tunnel facilities could reach similar Reynolds numbers. Therefore, these shear patterns could be used as an indication of whether or not the experimental or computational results were reproducing flow structures similar to those recorded during flight testing. Similar wall shear patterns were also produced with Edge Aerodynamix's higher-speed test platform, the SOKO G-2 Galeb, which strengthens the argument that similar flow patterns are produced during the flight tests in which fuel savings

Figure 4.2: Example of shock wave visualization over wing during baseline fuel consumption flights.

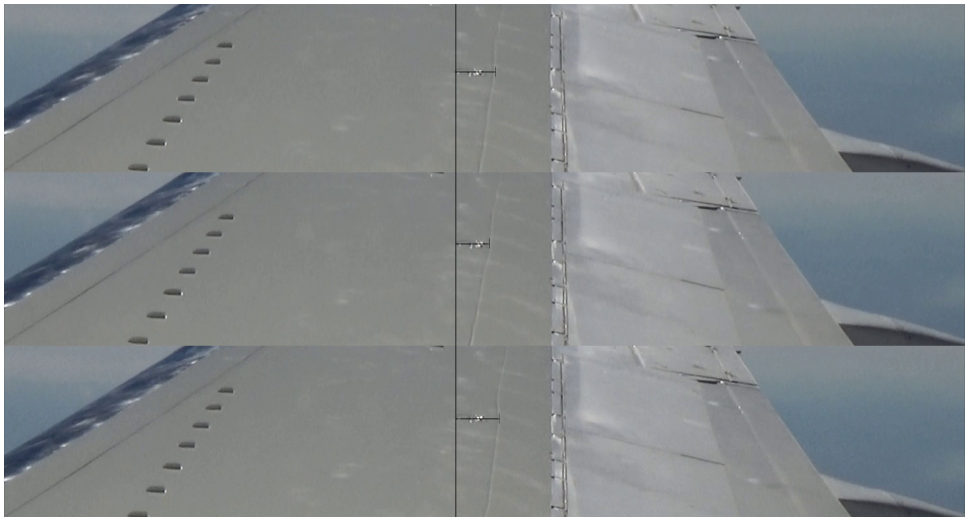

Figure 4.3: Example of shock instability over 0.3 seconds during baseline fuel consumption flights without the CVG installed.

were evaluated (the Boeing 737 and the Lear 24B). It should be noted that the Boeing 737 and the Lear 24B, which are the flight test platforms that saw an increase in fuel efficiency with the use of CVG, both operate in the transonic flight regime and that no wall shear evaluations were performed on these flight test platforms.

The wall shear testing performed by Edge Aerodynamix was done in accordance with Obara (1986) and utilized biphenyl as the sublimating chemical. The chemical is taken from a crystal state and dissolved in acetone, 8 parts solvent to 1 parts biphenyl. This solution is then spayed onto the surface with a compressed air paint sprayer. The goal is to coat the test surface in a soft powder, which is accomplished when the acetone evaporates out of the solution just prior to its contact with the surface; this is known as "dry-spraying" [96]. If the acetone is not fully evaporated prior to contact with the test surface, the solution will re-crystalize on the surface and perform improperly. Therefore, much care must be taken during the application process. Additionally, flakes, or small crystalized particles, may be produced during the process and contaminate an otherwise good application by producing a singular obstacle on the surface. An example of the results of these wall shear tests is provided in Figure 4.4.

4.2 Oklahoma State University Experimental Facilities and Equipment

The university has state of the art experimental equipment and facilities which enhanced the quality and capabilities of the research effort. The specific experimental systems used to conduct the experimental work discussed in this chapter is provided in this section for convenience and in order to avoid unnecessary repetition of the specifications of a given system.

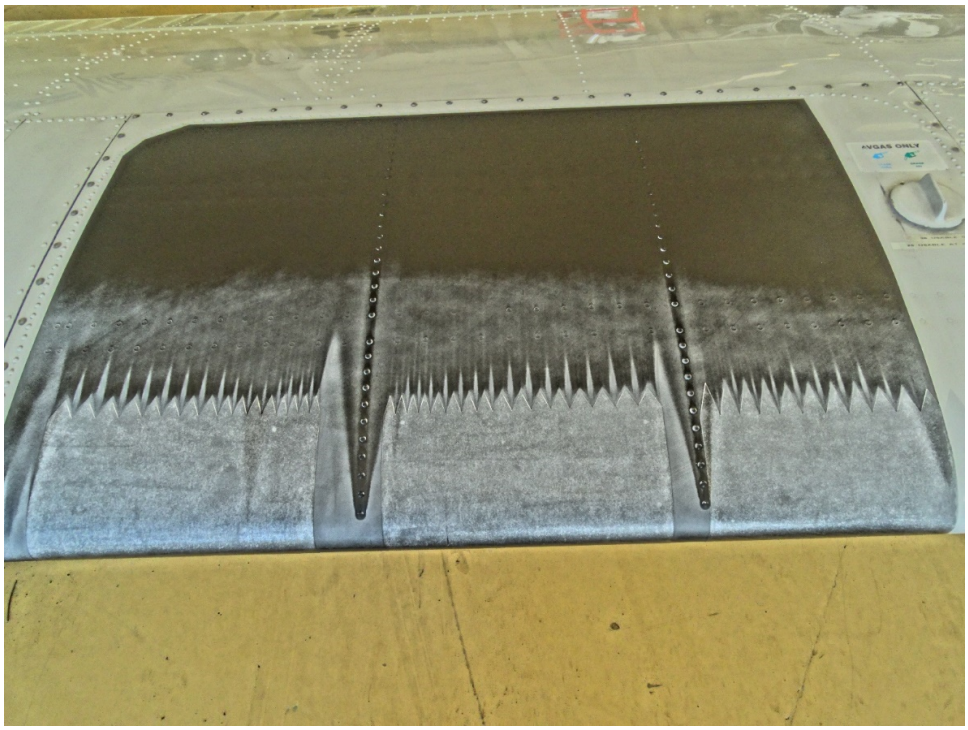

Figure 4.4: Results of wall shear stress flight testing by Edge Aerodynamix.

4.2.1 Small Wind Tunnel System

The small scale wind tunnel with a smoke wire visualization system is located in ATRC 052. This open wind tunnel utilized a Dayton Model 3HMJ8, 0.1 horsepower, centrifugal blower to pull air through the system. The inlet contraction had a 9:1 ratio and PVC pipe flow straightener to reduce turbulence in the test section. The test section had a 6 by 6 inch cross section with 2 feet of usable length and was constructed of clear polycarbonate in order to provide clear visibility from any angle. The diffuser section was not an ideal design, being constructed of a constant diameter circular cylinder, which contracted down from the 6 by 6 inch square cross section of the test section to the 4 inch diameter diffuser section over only 4 inches. This tunnel was mounted to a cart as shown in 4.5 . A simple smoke wire system was mounted to the tunnel with 5 nickel-chromium wires stretched horizontally across the upstream entrance to the test section. The system was powered with a conventional AC power adapter (previously used to charge a laptop battery) with 19 volts at 3.42 amps

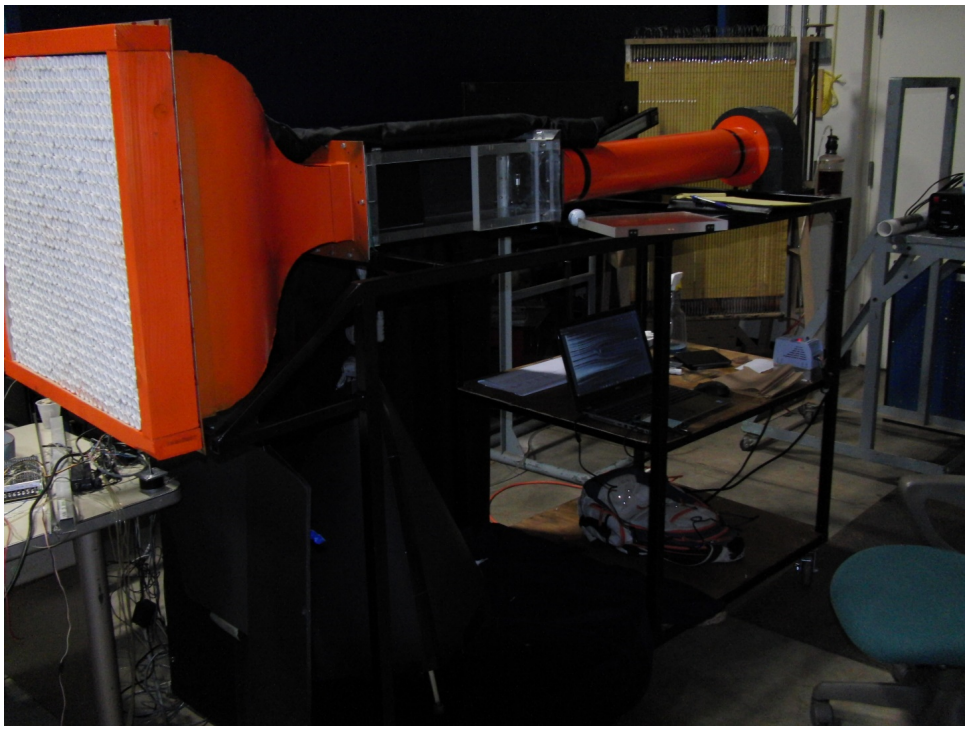

Figure 4.5: Small wind tunnel system.

Parameter	Value	Unit
Test Section Length	~ 60	cm
Test Section Width and Height	~ 15	cm
Max Velocity	~ 1.2	m/s
Re_{Max}	$\sim 50,000$	

Table 4.4: Small wind tunnel parameters.

output, and a switch completed the circuit for easy activation. The user would apply glycerin to whichever wires were intended to produce smoke lines, then close the test section, turn on the tunnel, and active the smoke wire switch. The wires heated and caused glycerin to organize into small droplets along the wire and to eventually smoke, producing an organized smoke line within the test section. The model being test could be oriented vertically or horizontally depending upon which orientation was preferred for smoke visualization was preferred. The wind tunnel specifications are also listed in table 4.4.

4.2.2 Medium Water Tunnel System

The Oklahoma State University Advanced Technology Research Center basement water tunnel lab facility houses a medium-sized Engineering Laboratory Design Model 503 30 cm recirculating water tunnel capable of obtaining Reynolds numbers up to one million. This facility provided adequate space for instrumentation and testing procedures to take place. The water tunnel was powered by two WEG Model 00718ET3E213T-W22 7.5 horsepower pumps, which could be controlled independently. A control panel allowed the operator to vary the test section velocity by specifying each pump frequency from zero to seventy in one-tenth increments. Figure 4.6 shows the frequency to velocity calibration data for this system, which shows the velocities obtainable for various pump frequencies on either pump. The test section could be operated with a closed or open test section top; the open configuration was usually preferred for dye testing. This tunnel's test section was 30 cm by 30 cm by 1 m as shown below in Figure 4.7. The contraction section of the tunnel had a ratio of 4 to 1 with flow straightener screens to reduce the turbulence in the test section. The diffuser used vanes to direct the flow and reduce swirling in the recirculating system. This tunnel was also equipped with a chlorine filtration system, which reduced coloration in the water from dye testing. However, the filtration system had limitations, and if the water was drastically discolored, draining and refilling the tunnel was the preferred method for correcting the problem. Yet, draining the water tunnel took roughly seven hours, and therefore, was avoided until the end of the data collection session as often as possible. This drain time could be drastically reduced if the tunnel's main drain was properly connected to the building plumbing. The water tunnel specifications are also listed below in Table 4.5.

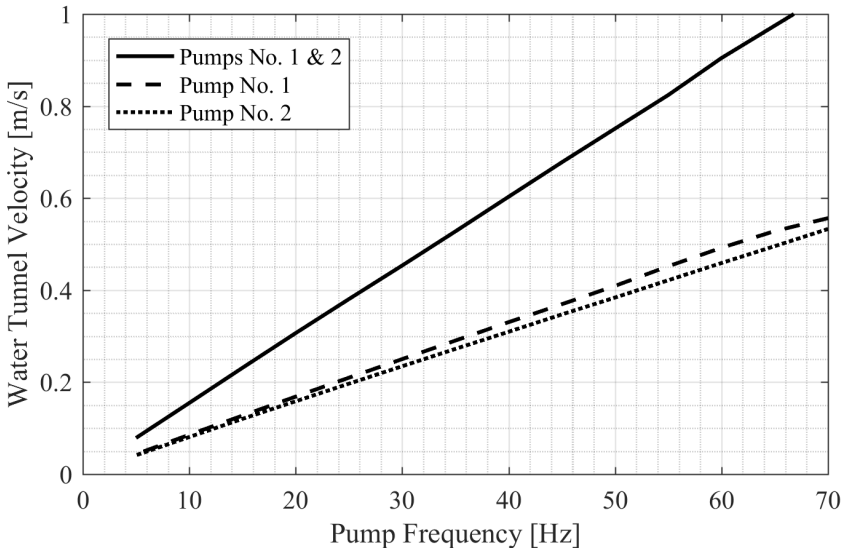

Figure 4.6: Medium water tunnel pump-to-velocity calibration plot.

Figure 4.7: Medium water tunnel system.

Parameter	Value	Unit
Test Section Length	~ 1	m
Test Section Width and Height	~ 30	cm
Max Velocity	~ 1	m/s
Re_{Max}	$\sim 1,000,000$	

Table 4.5: Medium water tunnel parameters.

4.2.3 Particle Image Velocimetry Systems

There are three entirely independent PIV systems provided by the associated research labs at Oklahoma State University.

High-Resolution Particle Image Velocimetry System

This systemincluded two high-resolution Imager sCMOS LaVision, which were 5.5 megapixel with a 2,560 x 2,160 resolution. These cameras shot 5.5 megapixel images at 50 frames per second or 1 megapixel images at 275 frames per second. It used a Gemini 200-15 Nd:YAG laser with a maximum pulse rate of 15 Hz, and could produce 200 mJ/pulse. The high-resolution PIV system provided more detail and better resolution at the expense of sample rate, and as such, could not take time resolved data.

High-Speed Particle Image Velocimetry System

This system included two high-speed phantom M110 CMOS cameras, which were 1 megapixel with a 1,280 x 800 resolution. These cameras shot 1 megapixel images at 1,630 frames per second or 0.07 megapixel (256 x 256 resolution) images at 19,800 frames per second. It used a Photonics DM30-527 Nd:YLF high-speed diod pumped laser with a maximum pulse rate of 10 kHz, and could produce 30 mJ/pulse, but only a 1 kHz pulse rate at max intensity. The high-Speed PIV system time resolved flow field measurements at the expense of resolution, and as such, could not resolve smaller scale motions.

Exploratory Particle Image Velocimetry System

This system included a single MotionPro X3M-G-4 high-speed camera, which were 1.3 megapixel with a 1,280 x 1,024 resolution. This camera could shoot 1.3 megapixel images at 1,000 frames per second or 0.05 megapixel images at 4,000 frames per sec-

ond. It used a Twins Big Sky Laser (BSL) 230 double-pulse Nd:YAG laser with a maximum pulse rate of 15 Hz, and could produce 230 mJ/pulse. Although this PIV system may not provide the highest resolution or utilize a high speed laser, it was perfectly adequate for taking flow field measurements in the expected experimental flow regime, and it allows for continuous testing and experimental design modifications because this system is not in high demand.

4.2.4 Gravity-Fed Dye Injection System

The gravity-fed dye injection system consisted of a vertical linear traverse attached to the side of the water tunnel with a shelf that supported three dye bottles, as shown in Figure 4.8. The dye bottles were open to the atmosphere and had ports on the bottom which connected to thin Tygon tubing that transported the dye from the reservoir bottles to the dye ports within the water tunnel test section. 0.05 inch diameter needles were used to inject dye into the test section. Dye port holes were normally drilled into the model to allow the dye to be injected through and to the desired location of release. The pressure of the dye injection could be precisely tuned by adjusting the vertical traverse until the desired dye pressure was obtained. However, the dye pressure decreased overtime as the dye was ejected and the reservoir head was reduced.

4.2.5 Hydrogen Bubble Flow Visualization System

The hydrogen bubble system consisted of an anode (platinum wire 25 μm and 50 μm) placed upstream of the test model that dictated the size of the bubbles produced. This wire was the bubble seeding location and could be modified per application; for example the wire could be insulated at constant intervals along the length to produce streamline-like formations. A cathode (1/4 inch steel bar 1 foot long and 1 inch wide) was placed downstream of the test model and could be positioned so that it

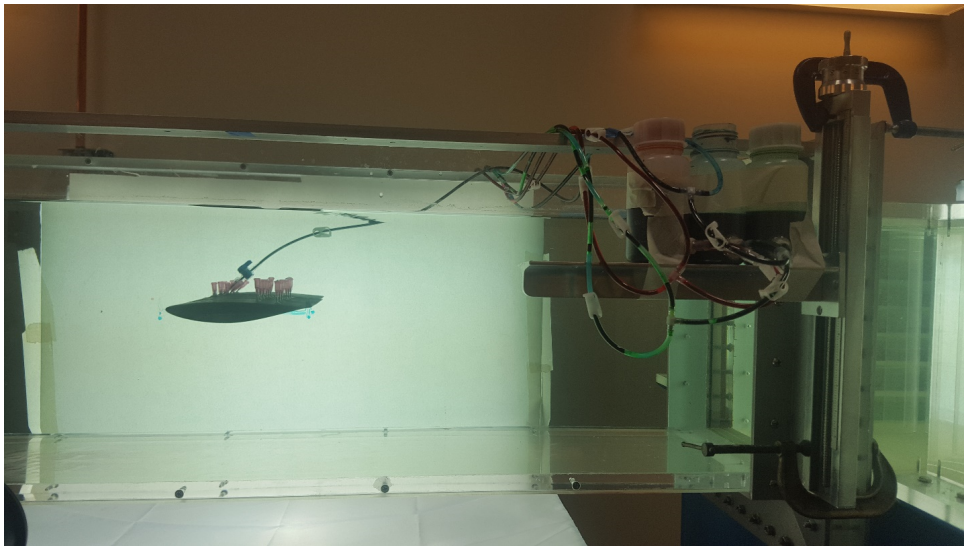

Figure 4.8: Gravity-fed dye injection system.

obstructed the flow. A variable power supply (P/N: CSI12001X, 0-120VDC and 0-1 AMP) powered the system with between 50 and 75 volts depending on the tunnel velocity. Additionally, the hydrogen bubble production could be further enhanced by adding salt to the water in the tunnel.

4.2.6 Cannon EOS 70D Camera

The Canon EOS 70D DLSR was a 20 megapixel camera with 5,472 x 3,648 resolution and an EFS 18-55 mm lens. It was capable of shooting 20.2 megapixel images at 7 frames per second. Additionally the EOS 70D was capable of recording 1,920 x 1,080 pixel video at 30 frames per second or 1,280 x 720 pixel video at 60 frames per second. This camera's frame rate and aperture was adjustable to better capture flows of different speeds.

4.2.7 Casio Exilim EX-F1 Camera

The Casio Exilim EX-F1 digital camera was a 6 megapixel camera with 2,816 x 2,112 resolution. It was capable of shooting 6 megapixel images at 60 frames per second for 1 seconds or 5 frames per second for 12 second. Additionally the Exilim EX-F1 was

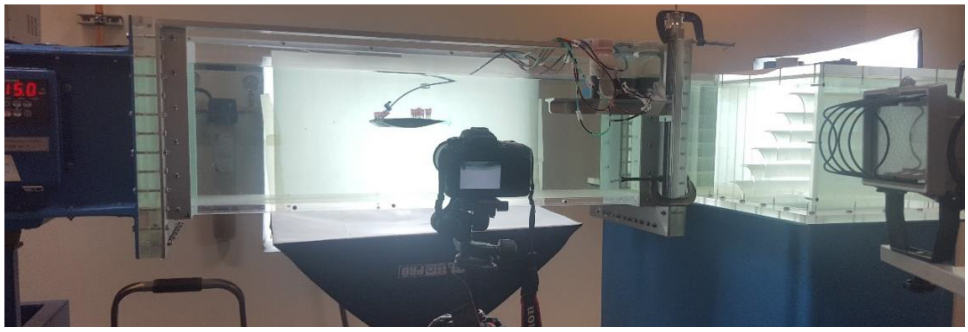

Figure 4.9: Lighting systems in place around medium water tunnel.

capable of recording 1,920 x 1,080 pixel video at 60 frames per second. This camera's frame rate and aperture was adjustable to better capture flows of different speeds.

4.2.8 Photography Lighting System

The professional lighting system allowed the use of higher frame rates and enhances the quality of video or images taken. The lighting system consisted of two one-thousand att photo boxes and one two-hundred watt photo box. These lights may be used in any configuration; although the preferred configuration was to use two lights for off axis lighting, perpendicular to the camera lens and using a flat white backdrop illuminating the form behind the image as shown in Figure 4.9. An additional light source added to systems would further improve the quality of the flow visualization images by allowing every side of the model to be highly illuminated (from downstream, bakground, top, and bottom).

4.3 Initial Low-Speed CVG Visualization Attempt

Initial testing of the CVG geometry performed at Oklahoma State University was a simplistic approach to visualizing the flow field around the CVG technology. The goal of this preliminary test was to attempt to visualize unique flow patterns without an extensive experimental design. These results would then guide the future, more complex, experimental approaches aimed at understanding how the CVG device can

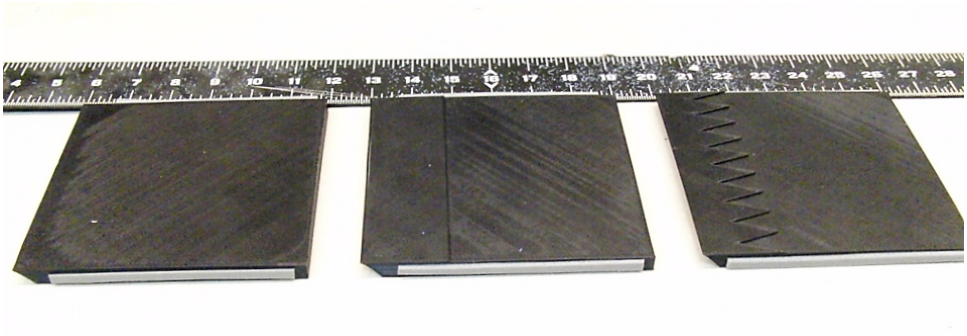

Figure 4.10: All three flat-plate models for comparison.

be scaled.

3D printed 6 in by 5.75 in by 1 cm, flat-plate models were constructed with ABS (acrylonitrile butadiene styrene) material. The models had a 45 degree leading edge and each contained a specific geometry; idealistic flat-plate, backward-facing step, and the CVG pattern. The step height was 1 mm, roughly three times the actual CVG tape height. The CVG pattern consisted of triangles with a height of 1 inch and a base length of 0.5 inch. Figure 4.10 shows the three flat-plate models for comparison. These models were not as smooth as originally intended, and had a nominal surface roughness due to the printing material; however, for this initial test it was not considered a critical issue. Each flat-plate model had a felt gasket material applied to the side in order to secure it between the test section walls. Models were placed vertically (perpendicular to the horizontal smoke wires) in the test section so that the smoke lines would produce trails similar to streamlines. Figure 4.11 shows the orientation and location of the flat-plates in the test section. A wooden block was used to consistently place and orientate each model in the tunnel.

The experimental setup was built around the wind tunnel cart discussed in Section 4.2.1. A construction style light with two horizontally mounted independent flood lights was placed upstream of the inlet contraction. It was found that using only one of the flood lights positioned directly down the middle of the tunnel produced the best lighting and reduced reflections. The Casio Exilim camera was mounted to small

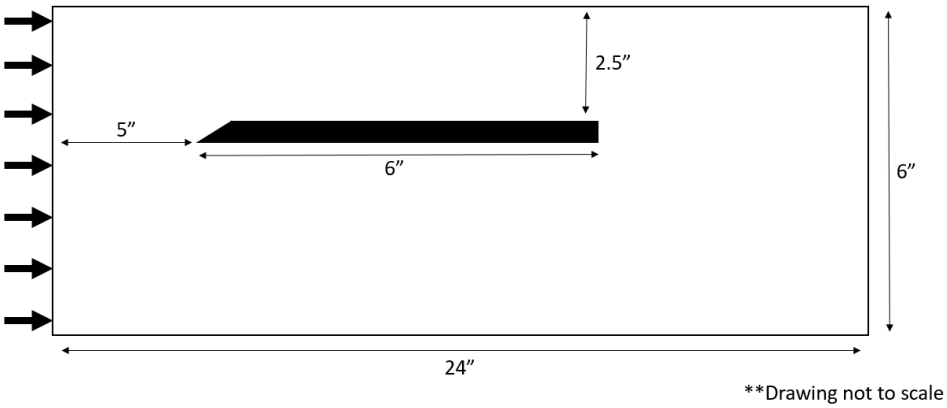

Figure 4.11: Depiction of flat-plate model in test section.

tripod and placed underneath the test section and orientated upward to produce a profile image of the flat-plate model. A black background was placed inside the wind tunnel test section on the top wall, opposite of the camera and a flat black sheet was used to cover the entire cart while taking images to minimize external lighting effects. This lighting and camera configuration allowed the images to be taken with minimal reflections; however, reflective surfaces behind the camera could still be seen in the frame. This was corrected by covering the camera tripod and other metallic surfaces with a flat black sheet. All of the tests were performed at the same tunnel velocity of 1 m/s, which was chosen based on the behavior test sections flow and the visibility of the smoke lines. During testing, the images were taken in succession (10 images per second). The test properties are given in Table 4.6.

Afterward, images were modified to enhance the visibility of the smoke lines. These images were then qualitatively compared between the tree configurations. An example of the images compared are shown in Figure 4.12. Several sets of images were compared; however, inconsistencies in the wind tunnel flow, poor downstream lighting, and the existence of a leading edge separation bubble made it difficult to evaluate the results. The flow in the test section was not consistent and appeared to fluctuate randomly, which can be seen in Figure 4.13. These fluctuations were attributed to the thick PVC pipe flow straighteners, poor diffuser design, and hot

Parameter	Value	Unit
H	~ 1	mm
L	~ 25	mm
W	~ 12	mm
X	~ 40	mm
ρ	~ 1.23	kg/m^3
μ	$\sim 1.88 \times 10^{-5}$	$Pa\text{-}s$
ν	$\sim 1.23 \times 10^{-5}$	m^2/s
T	~ 273	K
U	~ 1	m/s
Re_H	~ 65	
Re_X	$\sim 2,600$	

Table 4.6: Initial low-speed experimental flow properties (all properties which are a function of x-distance are given at the step location).

light source upstream of the wind tunnel inlet. Downstream lighting in the wind tunnel was not possible due to the centrifugal pump design, and the upstream light source (only 500 W) was not bright enough to properly light the aft portion of the flat-plate models. This produced exposure issues in the images and often caused the smoke lines to fade out of the image downstream. The 45 degree angle integrated into the leading edge of the flat-plate models produced a leading edge separation bubble, which influenced the flow, and therefore, modified the flow behavior over the geometry.

The initial set test did not show any constantly noticeable differences in the flow field around any of the three geometries. This was most likely due to the inconstancies in the flow field and the presence of the leading edge separation bubble, because a backward-facing step is known to have drastically different flow structure as compared to a flat-plate. Therefore, no comparative conclusions could be made from the results of this test. However, this set of tests demonstrated the sensitivity to inlet flow conditions, difficulty in properly visualizing flow over the small-scale geometry, and leading edge effects. New experimental designs required higher quality inlet flow to adequately evaluate the flow around small scale geometry. Additionally, the speed

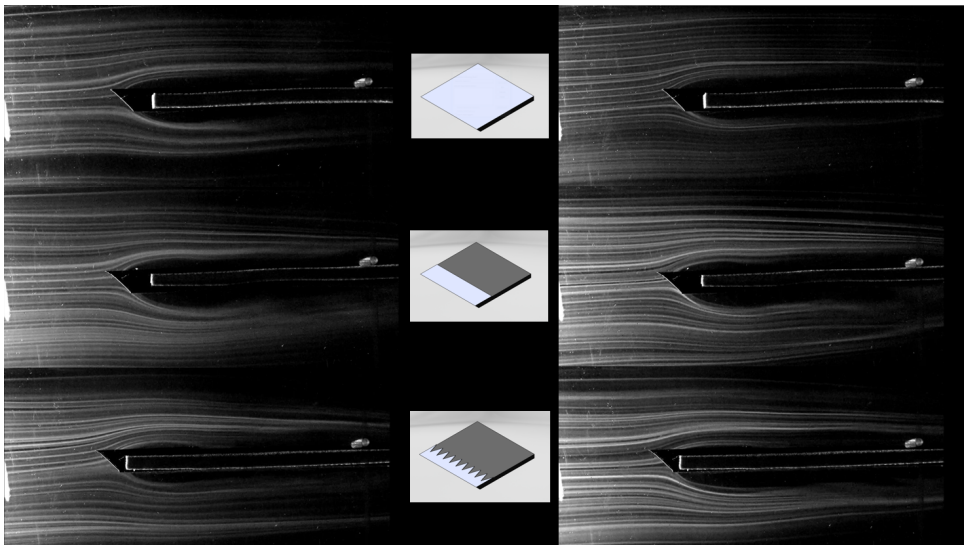

Figure 4.12: Example of image comparison from wind tunnel tests.

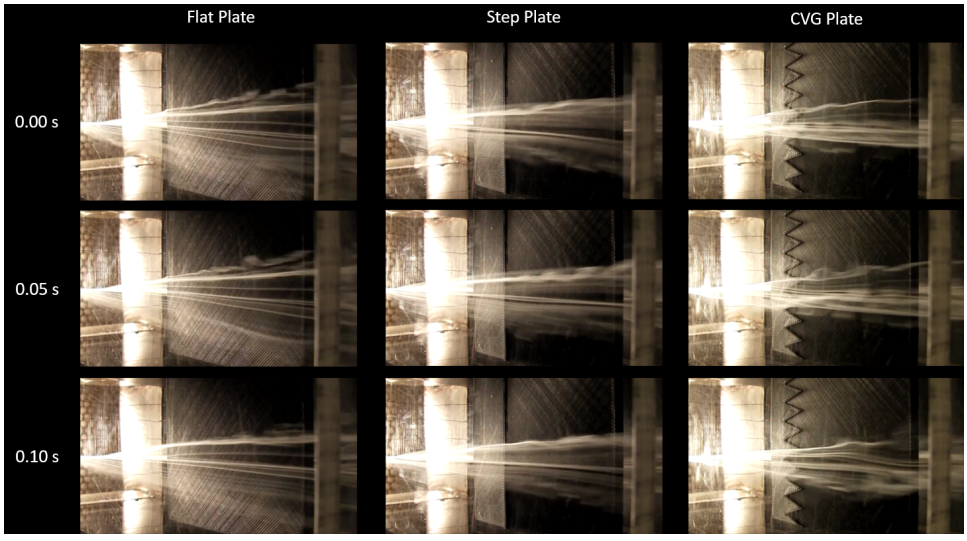

Figure 4.13: Visualization of unsteady inlet velocity.

and zoom of the camera needed to be improved along with the lighting of the test section. Future flat plate models needed either longer upstream length for the effects of leading edge bubbles to be mitigated or an entirely different leading edge shape all together.

4.4 Flat-Plate Re_X Scaled Dye and PIV Testing

The goal of this set of tests was to investigate the Reynolds number based on downstream location scaling of the CVG. This scale was selected for its simplicity, which only required constructing a flat-plate model and applying the CVG tape directly to it. Flow visual testing with dye injection was the original objective, but subsequent PIV tests and CFD simulations were also conducted. The findings of these tests guided the choices for the additional testing conducted.

4.4.1 Experimental Methods

A model was constructed of quarter inch polycarbonate plate which spanned the width of the tunnel and roughly 23 inches in the flow direction. A 45 degree angle was cut on the leading edge and the plate was mounted to a frame and painted white for optimal visualization. The experimental setup for the dye testing utilized the medium water tunnel, gravity-fed dye system, and the phantom M110 cameras from the high-speed PIV system discussed in Section 4.2.3. This configuration required the water tunnel test section to be open on the top with the flat-plate model suspended upside down in the test section. Dye injectors were placed in various configurations around the CVG to visualize the effects seen at different locations. The two cameras were configured to provide top-down and side views of the flow around the CVG, which allowed the two to be compared simultaneously. Figure 4.14 shows the model geometry, and Table 5.1 lists the properties of the flow. In addition to the dye testing, PIV tests were also conducted using the high-resolution PIV system discussed in Section 4.2.3, and the

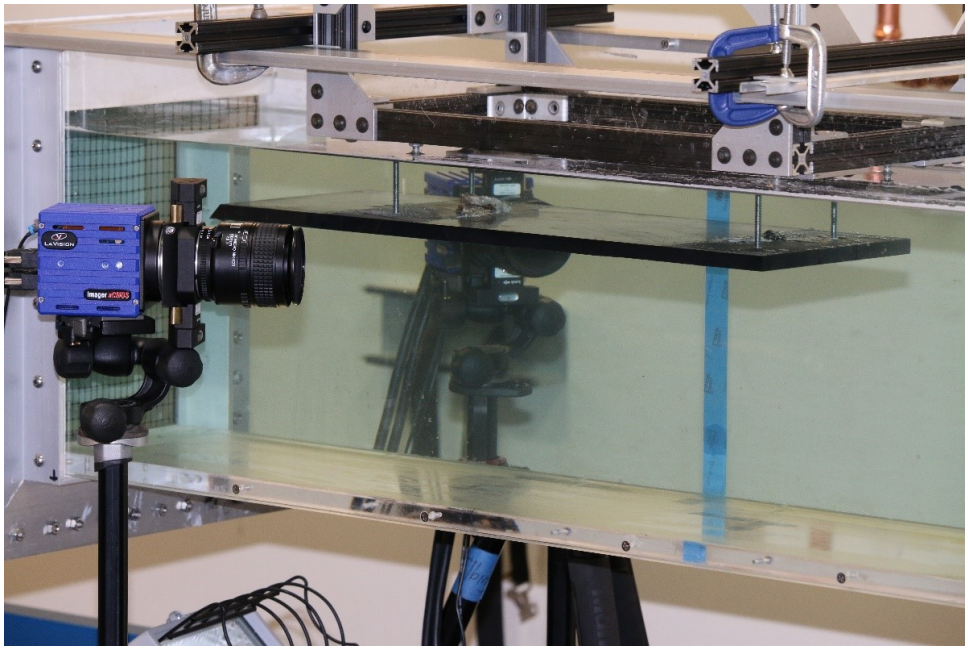

Figure 4.14: Medium water tunnel test model

data was collected with the specifications listed in Table 4.8. The Reynolds number range of the experimental CVG was matched to that of the subsonic flight tests with a tunnel velocity of roughly 1 m/s.

4.4.2 Results and Discussion

The dye test results were sensitive to dye injection pressure. When too much pressure was applied, the injection would add momentum to the flow, and when the pressure was too low, it resulted in poor visualization. This was further complicated when testing various tunnel velocities that required the dye injection to be readjusted to a new ideal pressure. Although the process was tedious, it was still possible to hone in the perfect pressure for each velocity to produce quality visualizations. The dye tests were conducted for a large range of velocities from (0.1 to 1m/s), but the results appeared to be consistent despite the velocity changes. Figure 4.15 shows results from four different tunnel velocities all with similar results. These results suggested that the CVG pump fluid from the upstream apex out to the downstream apex within the geometry and evacuate the central region of the CVG, which appeared

Parameter	Value	Unit
H	~ 0.367	mm
L	~ 24	mm
W	~ 16	mm
X	~ 450	mm
δ_{99}	~ 16	mm
θ	~ 1.6	mm
δ^*	~ 2.0	mm
H/δ^*	~ 0.19	mm
H/θ	~ 0.23	mm
H/δ_{99}	~ 0.023	mm
ρ	~ 1000	kg/m^3
μ	~ 0.001	$Pa\text{-}s$
ν	$\sim 1.0 \times 10^{-6}$	m^2/s
T	~ 273	K
U	~ 1	m/s
Re_θ	$\sim 1,600$	
Re_H	~ 367	
Re_X	$\sim 4.5 \times 10^5$	

Table 4.7: Re_X scale experimental flow properties (all properties which are a function of x-distance are given at the step location).

Parameter	Value or Description
dt	1000 μt
Number of Images	200
Frequency	1 Hz

Table 4.8: Re_X scale PIV settings

to be the case despite the variation of the freestream velocity. The findings were interesting, but did not shed light on the large effect of the flow field; therefore, PIV tests were conducted to attempt to produce a better description of the larger flow field. However, the incredibly small scale of the CVG device did not allow for adequate resolution near the device itself, as shown in Figure 4.16. The inability to properly resolve the flow near the CVG with the PIV system emphasized the need for an appropriate way to scale-up the CVG geometry and suggested the potential need to improve small-scale PIV capabilities. Additionally, the relatively small scale of the CVG posed the question of whether any CFD method would be capable of adequately simulating flow over the device. This led to the next experimental investigation, which tested and enlarged CVG geometry while experimental and computational methods were explored. Additionally, this experimental design highlighted some key issues which were improved upon in later work. The 45 degree leading edge of the flat-plat model consistently produced a separation bubble and adversely effected the natural formation of the boundary layer; therefore, a new leading edge design was needed. The quarter-inch polycarbonate plate was prone to flexing in the flow direction, and the thickness needed to be increased to reduce the effects on the flat-plate geometry.

4.5 Flat-Plate Re_H Scaled Dye and PIV Testing

Reynolds number based on step-height scaled experimental work was a direct product of the conclusions drawn from the x-distance based Reynolds number scale results, which emphasized the issues of working with such a small-scale geometry. Therefore, a larger geometry was designed and tested to investigate the flow field around a scaled CVG geometry step height. These tests focused on comparing the enlarged CVG geometry to a traditional backward-facing step of the same step-height.

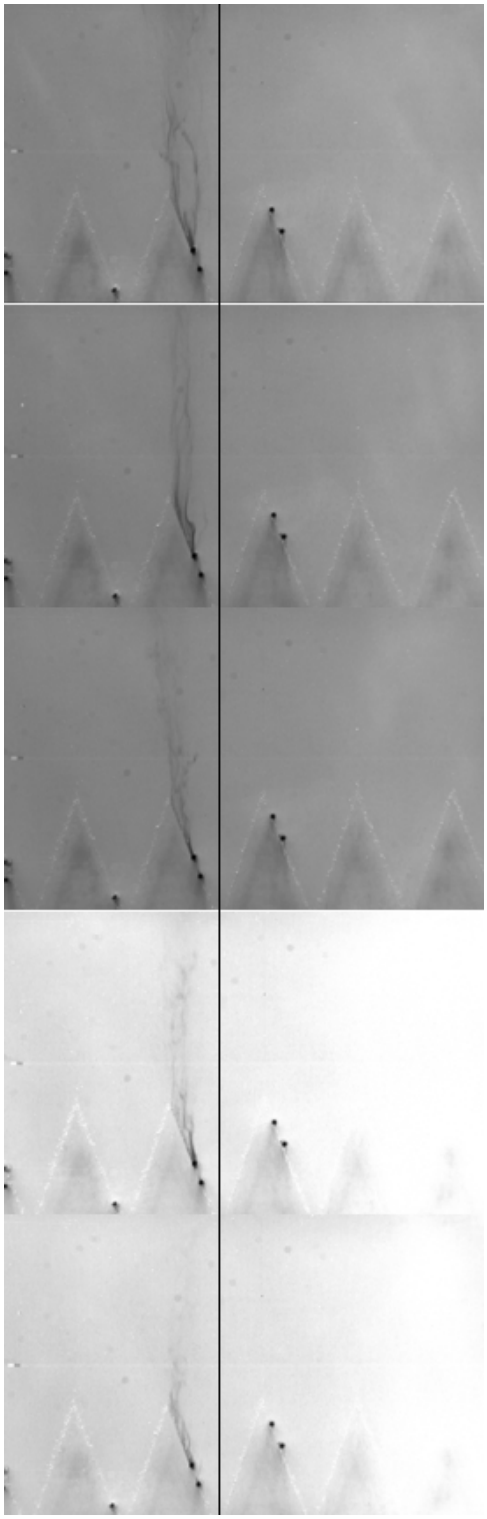

Figure 4.15: Medium water tunnel dye testing at different tunnel velocities, flow is up (top to bottom lowest speed to fastest speed).

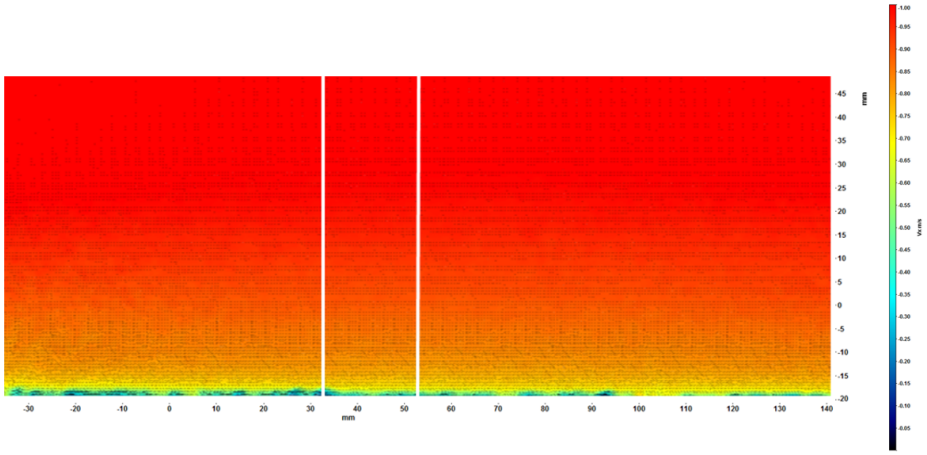

Figure 4.16: PIV measurements were not well resolved and the step geometry cannot be seen. Flow is left to right and white lines mark where the CVG begins and ends.

4.5.1 Experimental Methods

The test model was constructed of a half inch polycarbonate plate with a 45 degree leading edge fairing attached to the front. The plate was the width of the water tunnel in the span direction and roughly 2 feet long. The leading edge was 3D printed and contained the backward-facing step and enlarged CVG geometry, which was fixed to the plate so that the upstream surface consisted of the leading edge fairing, and the downstream surface was the polycarbonate plate. The constructed model is shown (painted black) in Figure 4.17. The entire model was painted white for dye testing and then black for PIV testing and mounted to a frame and placed upside down in the water tunnel with the top open. The appropriate scale was obtained when the water tunnel velocity was approximately 0.15 m/s, but a variety of velocities (0.1, 0.5, and 1 m/s) were investigated to explore the flow features. Flow properties are also provided in Table 5.6. The dye ports were drilled and placed upstream of the geometry to allow the dye to naturally advect downstream and over the geometries of interest. PIV testing was accomplished with the high-resolution system discussed in Section 4.2.3, the specifications in Table 4.10, and was intended to be a test of the experimental setup prior to having access to the high-speed system to take unsteady data of the

Figure 4.17: Re_H scaled CVG model

flow. However, evaluation of the dye tests and the initial non-time resolving PIV tests concluded that the Reynolds number based on step height was not the correct scaling approach, and as a result, was no longer of interest.

4.5.2 Results and Discussion

Flow visualization testing was inhibited by turbulent transition due to the 45 degree leading edge, which produced a separation bubble as seen in Figure 4.18 and required modifying the leading edge to an ellipse, which delayed transition. Once the leading edge surface was refinished, the flow over the model remained laminar all the way to the steps. Figure 4.19 compares the previous flow condition to the laminar inlet flow condition. The Enlarged CVG geometry dye injection results were the most valuable product of these tests. Flow behavior over the backward-facing step and enlarged CVG were compared side by side and found to be nearly identical. Both geometries had a clear separated shear layer, recirculation region, and periodic shedding of

Parameter	Value	Unit
H	~ 10	mm
L	~ 27	mm
W	~ 22	mm
X	~ 230	mm
ρ	$\sim 1,000$	kg/m^3
μ	~ 0.001	$Pa\text{-}s$
ν	$\sim 1.0 \times 10^{-6}$	m^2/s
T	~ 273	K
U	~ 0.1	m/s
Re_θ	~ 296	
Re_H	$\sim 1,000$	
Re_X	$\sim 35,000$	

Table 4.9: Re_H scale experimental flow properties (all properties which are a function of x-distance are given at the step location).

Parameter	Value or Description
dt	3000 μt
Number of Images	100
Frequency	1 Hz

Table 4.10: Re_H scale PIV settings

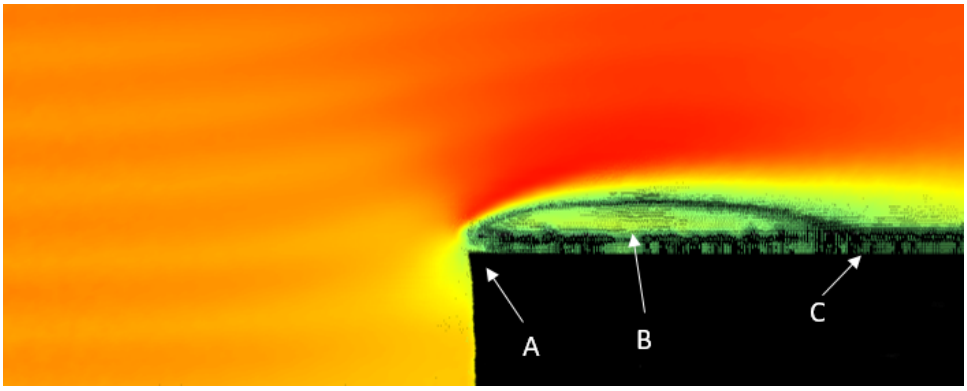

Figure 4.18: PIV image of flow over original flat-plate model with 45 degree leading edge. A separation bubble is apparent ("A" is the leading edge, "B" is the separation bubble, and "C" is the boundary layer recovery region.

vortices downstream. The only noticeable consistent difference between the two was that the CVG recirculation region appeared to capture more dye and become much darker than that of the CVG; however, this was most likely due to the fact that the CVG geometry has more volume upstream of its recirculation region where dye could accumulate over time. A comparison between the two is given in Figure 4.20. The conclusion made from these tests was that the CVG width and length must be scaled with the step-height and that, as the ratio of step-height to triangular length (in the flow direction) approached one or larger, the CVG behaved similarly to a backward-facing step. This finding guided the next scaling attempts which continued to add more parameters into the scaling approach, while small-scale flow visualization and PIV systems were developed separately. Additionally, Issues with the model leading edge suggested that future flat-plate models should utilize longer elliptical leading edges. This requirement highlighted the need for a higher-fidelity water tunnel model and put in motion plans to construct a water tunnel lid-mounted flat-plate model with a machined elliptical leading edge for ideal boundary layer formation.

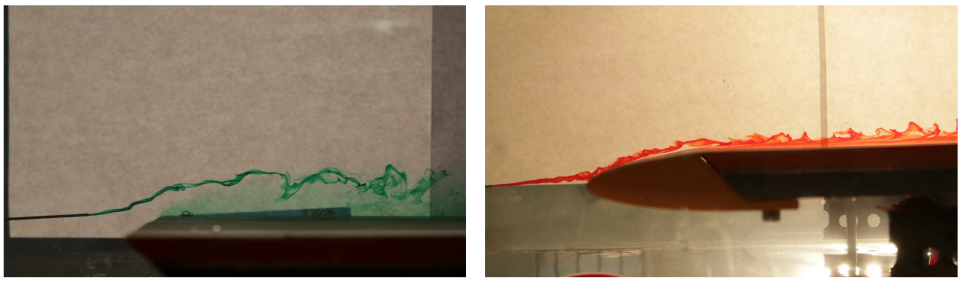

Figure 4.19: (left) Comparison of inlet flow quality between 45 degree and (right) elliptical leading edge.

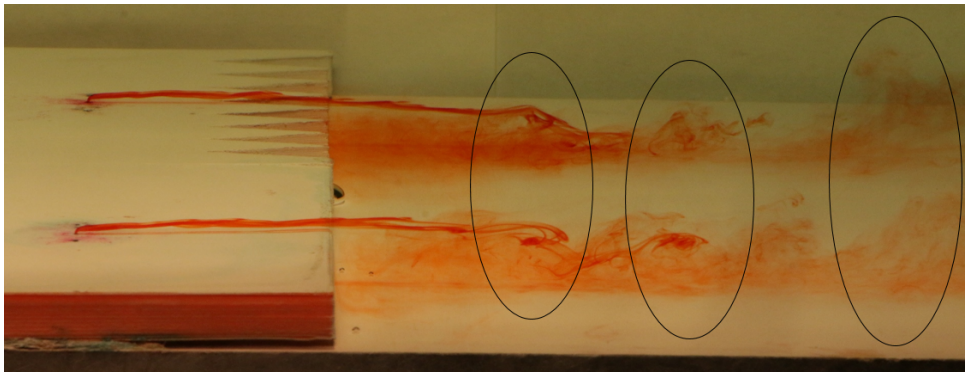

Figure 4.20: Flow over Re_H scaled CVG and backward-facing step model.

4.6 Airfoil Momentum and Wall Shear Scaled Dye and PIV Testing

This experimental study focuses on identifying differences in flow features associated with the CVG as compared to a traditional backward-facing step and the ideal smooth wing surface. Flow visualization methods were used to identify flow structures and characterize differences in the separation point on the airfoil. The CVG geometry and backward-facing steps were scaled using two separate methods based on the flight scale step height and the boundary layer parameters, which were discussed in Sections 3.10.3 and 3.10.4. There were extensive limitations associated with the results, due to some inconsistencies in the experimental methods. However, the results of this study indicated that the CVG geometry produced flow phenomenon was noticeably different than a traditional backward-facing step and the ideal wing surface. Specifically, the CVG delayed separation for laminar cases and produced more structured turbulent behavior for turbulent cases. These findings encouraged

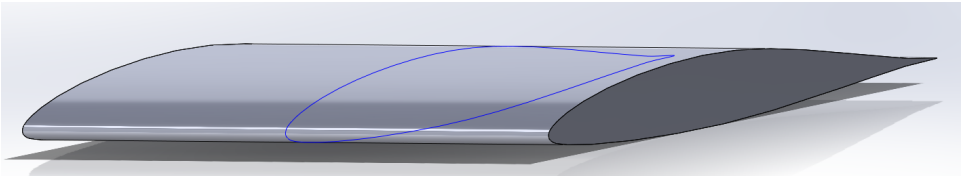

Figure 4.21: Ideal wing surface model.

further investigation of the CVG product. The goal of this experimental study was to attempt to quantify a noticeable difference in the flow characteristics between an ideal wing surface, backward-facing step, and the CVG geometry, and it specifically focused on visualizing potentially unique flow phenomena associated with the CVG geometry, such as streamwise vorticity.

4.6.1 Experimental Methods

Wing Section Model Design

A NACA 65-415 airfoil was selected for this study initially as a direct scaling from a Piper Cherokee flight test platform utilized by Edge Aerodynamix. The wing model stretched the entire span of the medium water tunnel (0.3 m) and had a 0.15 m chord in order to provide an aspect ratio of 2. An example of the ideal wing geometry is shown in Figure 4.21. The CVG and backward-facing step geometry was produced by generating an exact copy of the NACA 65-415 model, modifying the aft portion to produce the step or CVG, overlaying the two parts, and rotating the CVG or backward-facing step geometry about the leading edge to create the prescribed step height. The CVG pattern design and the rotation method is illustrated below in Figure 4.22 and Figure 4.23 for clarification. The wing geometry was 3D printed in segments using an AirWolf 3D printer. Three separate geometries were represented across the span of the wing model including the ideal wing surface, backward-facing step geometry, and the CVG geometry from left to right.

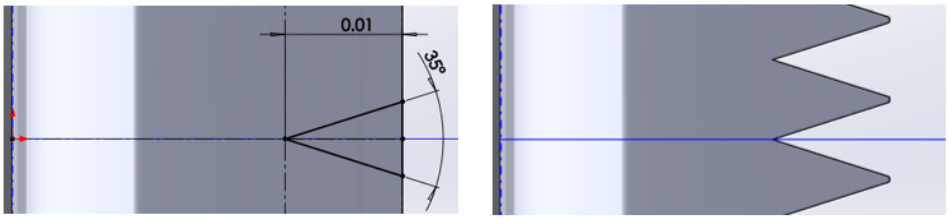

Figure 4.22: (left) CVG Geometry parameters at 17.5 percent chord. (right) CVG geometry after cut extrude.

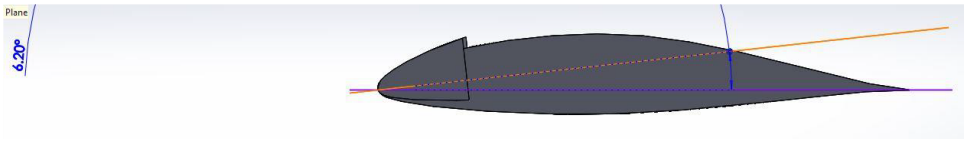

Figure 4.23: Step creation using rotated original wing geometry.

Test Procedure and Test Matrix.

Scaling options were evaluated from zero to one-meter-per-second tunnel velocity. The resulting CVG step-height scaling options are shown in Figure 4.24. It should be noted that the two scaling relationships do not intersect within the feasible velocity test range, which reiterates the difficulty of producing an accurate scaling without understanding the flow mechanisms related to the CVG product. The final test velocity for each geometry scale is given in Table 4.11; the middle test velocity is the actual scaled velocity, and the additional velocities are for comparison. The parameters evaluated for each image in the data collection were the following: reattachment location after the step, separation location, shedding period, amplitude of the shedding, and separation distance from the trailing edge. These measurements are illustrated in Figure 4.25.

Below is an example of the simplified test procedure:

- Place wing model in test section

Scale Method	Step Height	Test Velocity 1	Test Velocity 2	Test Velocity 3
Wall Shear Stess	$3.0mm$	$25.0cm/s$	$59.0cm/s$	$75.0cm/s$
Momentum Thickness	$0.36mm$	$34.6cm/s$	$36.0cm/s$	$37.5cm/s$

Table 4.11: Scaled step-heights tested.

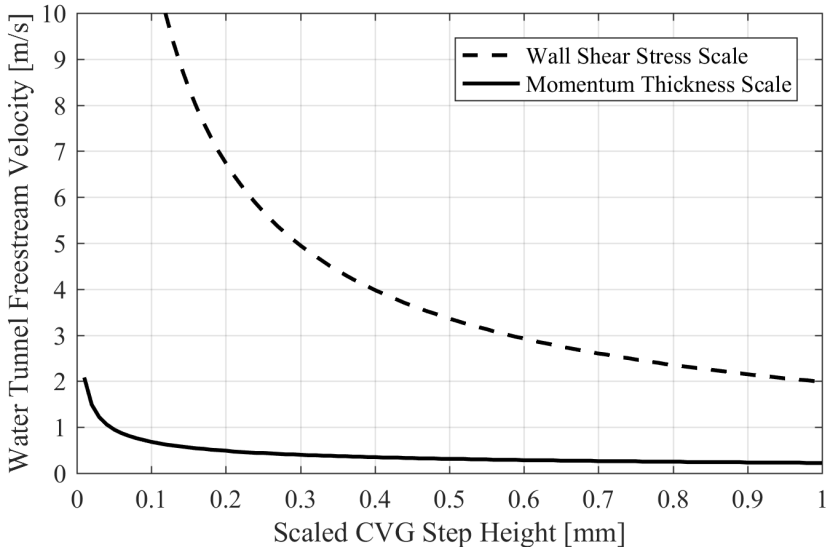

Figure 4.24: Possible CVG step-heights as a function of water tunnel freestream velocity.

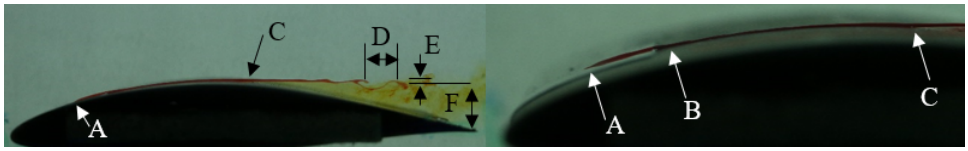

Figure 4.25: Explanation of measurements taken: "A" dye port (common reference point), "B" reattachment point after step, "C" separation location, "D" period of shedding, "E" shedding amplitude, "F" separation distance from the trailing edge.

- Connect dye system to the desired dye port
- Place spatial calibration ruler in the plane of the dye injection
- Move and level camera to the appropriate frame.
- Focus camera
- Take calibration image
- Remove calibration ruler
- Run tunnel to the desired test condition
- Wait 1 minute for the water tunnel to equalize
- Open dye injection feed
- Adjust gravity-fed dye traverse to appropriate static pressure
- Take sequential images
- Repeat steps for additional dye port locations or tunnel velocities

4.6.2 Results and Discussion

This experimental study was subject to multiple factors which limited the usefulness of the data collected. These factors are discussed in detail in the following subsections. The limitations of this study also significantly modified the evaluation of the results presented previously and the conclusions of the study. The experimental design was limited by the water tunnel facilities available for use. Specifically, the water tunnel width (0.3 m) influenced the wing model design which resulted in a shorter than ideal chord (0.15 m) in order to achieve an aspect ratio of two. However, the reduced chord drastically reduced the Reynolds number range of the wing section to between

20,000 and 200,000, which introduced the possibility of producing a separation bubble. The Reynolds number range where a separation bubble is known to form were avoided, which further constrained the low-speed testing options. Furthermore, the reduced Reynolds number at the location of the geometry, which ranges from 500,000 to 1,000,000 for the flight scale, more than likely influenced the results and weakened arguments concerning comparisons between tunnel testing and flight testing. Ultimately, this limited the results to comparisons between each test case and removed the validity of a detailed comparison to the flight case. The scaled geometries, which were discussed previously in detail, produced drastically different flow characteristics. Specifically, the momentum thickness scaled geometry maintained laminar flow past the backward-facing step and CVG. However, the wall-unit scaled geometry was forced to turbulence by the backward-facing step and CVG, which acted as a turbulent trip in the flow. This did not limit the ability to compare the two flows as a whole, but it did limit the ability to compare measured quantities, such as separation point, between the two scales. The most influential aspect of this was the inability to adequately evaluate turbulent flow signal or average quantities with only image data. Although, there were additional limitations that further inhibited the quantitative comparison between the two different scales. Limitations to comparing the data collected from the two scaled geometries were further enhanced by the use of two nearly independent teams which conducted testing for each scale. Furthermore, inconsistencies in testing procedure and test conditions were not adequately controllable or held constant between test regiments. The wing models angle of attack was not precisely controlled, allowing for differences in angle of attack every time the test platform was removed, which occurred twice for each team. This was obvious by comparing the separation point on the ideal wing geometry for each team, as shown in Figure 4.26. This plot indicated that there was considerable variation in angle of attack between the two teams' tests and reinforced the inability to directly compare the quantitative

results from one team to the other. Additionally, the data collected from different test regiments, even for the same team, where the wing model was removed from the test section should not be directly compared. An additional limiting factor to the results of this study was the acquisition of the images. In multiple test cases, the dye detached outside of the camera frame, as shown in Figure 4.27. This reduced the usefulness of nearly half of the data set collected, because the separation location was one of the most important and easily measureable parameters. Issues also arose in relationship to both of the flow visualization methods. The gravity-fed dye system was sensitive to input static pressure, which was controlled by the y-location of the traverse. Figure 4.28 is an example of the unsteady behavior caused by slightly too much static pressure in the dye system. This unsteady dye injection invalidated the measurement of the reattachment location and limited heavily the experimental results. The hydrogen bubble method produced poor visualizations for the test conditional of this study, as shown in Figure 4.29. This issue related back to the limitation regarding chord length, and as a result, required the use of higher tunnel velocities in order to reach adequate boundary layer scales. It was determined that the hydrogen bubble system should ideally be used in flows slower than 10 cm/s. Also, when using the hydrogen bubble flow visualization system, the results were more sensitive to the water tunnel test section reflections (visible in Figure 4.29). Therefore, future attempts with this method required use of a flat black insert on the background wall in order to remove any reflections from the test section.

Comparison between both scaled geometries was difficult because of the limitations discussed above. Issues effecting experimental results were common when working with low Reynolds number airfoils, often to the point of rendering unrepeatable results [97]. However, from the data collected, assuming relatively similar angle of attack, an initial look at a potential dimensionless relationship is shown in Figure 4.30, where Reynolds number based on the downstream location of the step and the Reynolds

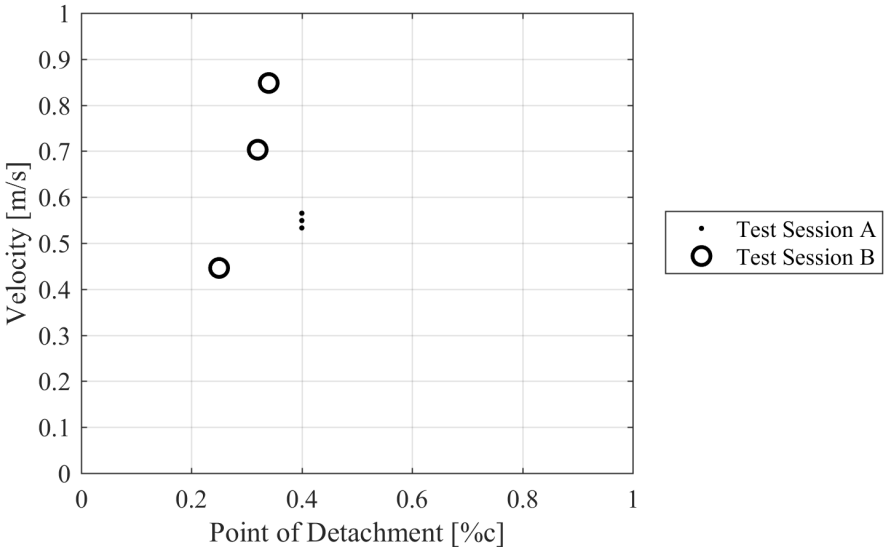

Figure 4.26: Plot of separation location as a function of tunnel velocity. This indicates that, between test sessions, the data is not consistent and cannot be directly compared.

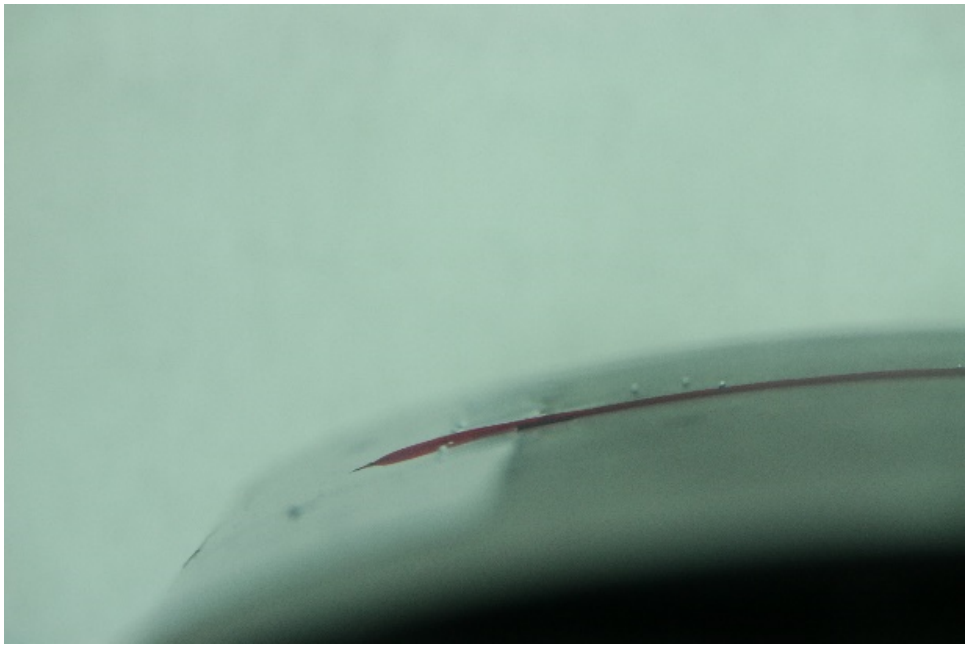

Figure 4.27: Depiction of camera frame not adequately large to capture separation point.

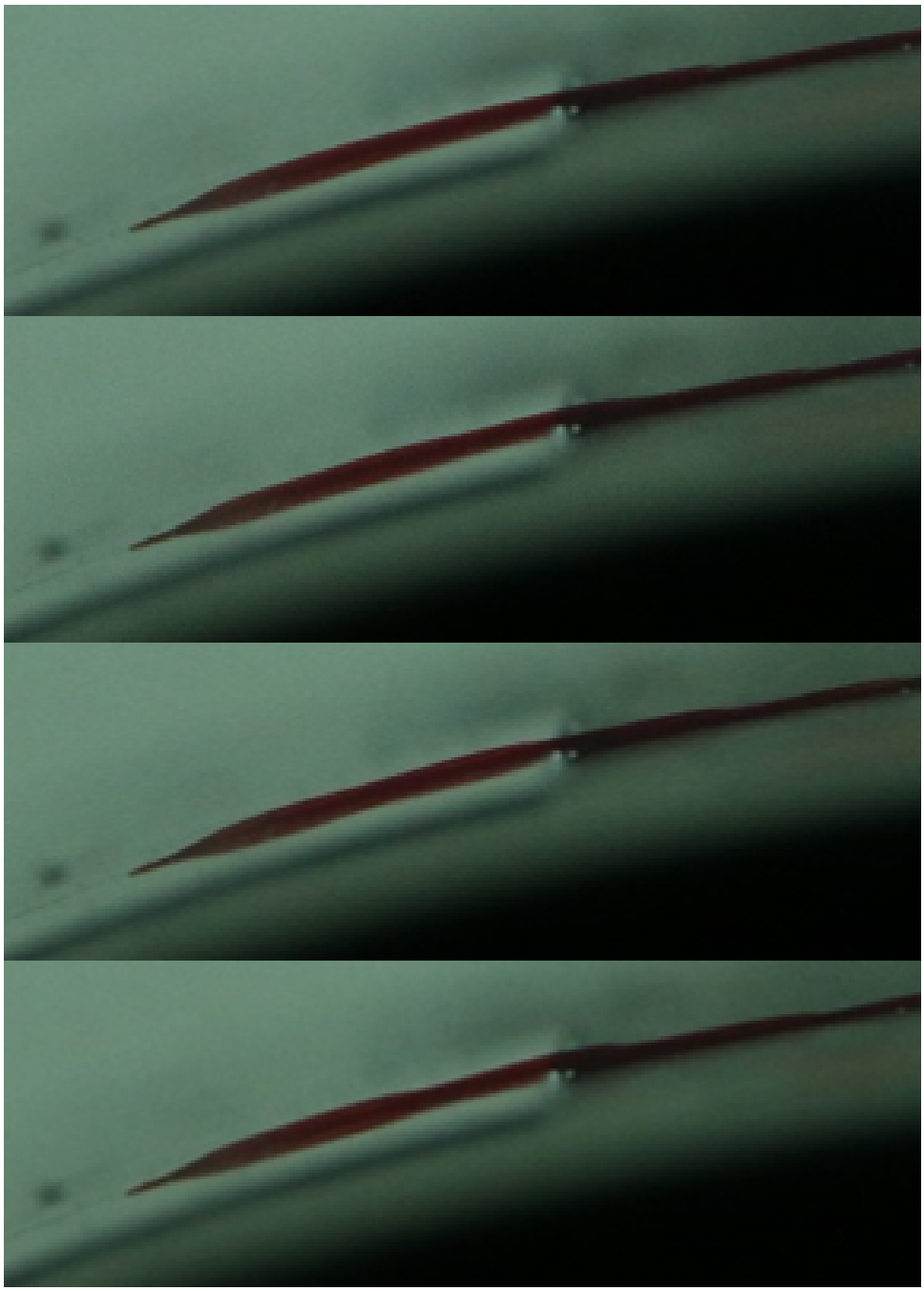

Figure 4.28: Sequential images of dye over backward-facing step depicting the unsteady dye injection and the effect on reattachment measurements.

Figure 4.29: Hydrogen bubble flow visualization (inverted and sharpened). The flow features are hard to discern. Reflections are seen as blurred lines and the faint bluish fingers (a closed hand operating the camera).

number based on the step height (which reduces to downstream distance over step height) are compared. From this plot, which consists of an extremely limited sample of data, a boundary between the flow over the step remaining laminar or tripping to turbulence can be produced. Although, without additional data, the current depiction only represents two liner bounds over a small region of the large, and most likely, nonlinear relationship. Additionally, a trend became apparent regarding the ideal wing surface data. The downstream separation point moved farther downstream as tunnel velocity increased. This was to be expected as shown in Figure 4.31, a simple panel method analysis of the NACA 65-415 performed by XFoil for the same chord base Reynolds numbers. The modeled results and the experimental results showed similar behavior, which strengthened the results of the experimental study. Numerous similar experimental studies were available for qualitative comparison. The laminar behavior over the step was consistent with Biswas, (2004), as shown in Figure 4.32, and the laminar separation behavior was consistent with Lin and Pauly, (1996), as

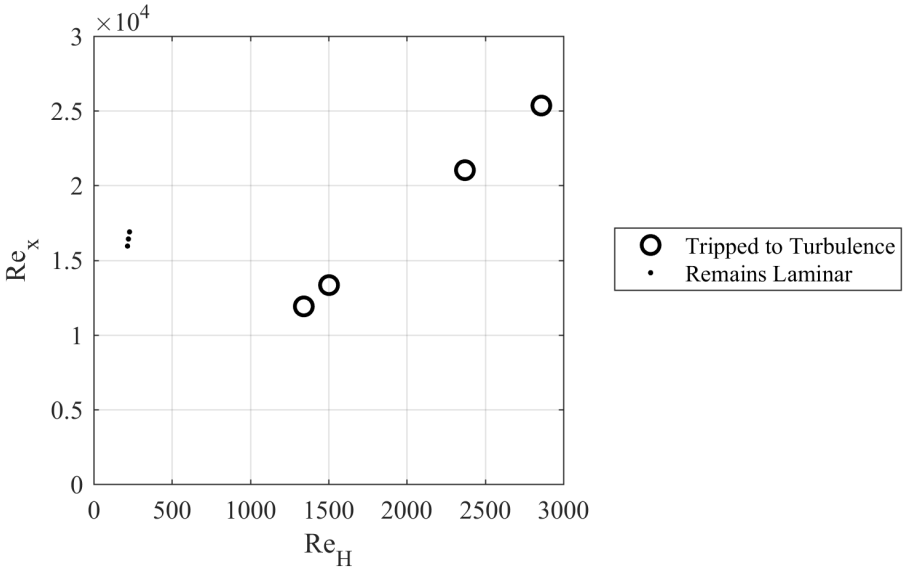

Figure 4.30: Initial data set that could be used to find a scaling relationship for the NACA 65-415 with backward-facing step that indicates weather a flow will transition to turbulence over the step or reattached and remain laminar. The plot is Reynolds number based on streamwise distance as a function of Reynolds number based on the step height.

shown in Figure 4.33. These comparisons build confidence in the results of the study. Detailed evaluations of the independent scaled results are discussed further in the following subsections.

The momentum scale results were heavily limited by the factors discussed in the previous section. However, the separation characteristics of the laminar flow in the adverse pressure gradient region was noteworthy. Therefore, after removing the data points in which the camera frame was not adequately large enough to capture the flow separation, a useful comparison of the downstream separation distance and separation height were plotted as provided in Figure Figure 4.34 and Figure 4.34 respectively. These plots clearly indicated that the CVG geometry produced favorable separation characteristics compared to the ideal and backward-facing step geometries were well within the uncertainty of the measurement. This suggests that the CVG geometry may be beneficial to reducing pressure drag. However, it should be noted that only one CVG data point was remained after removing the test results previously mentioned. This obviously left a lot of room for doubt and improvement. Although,

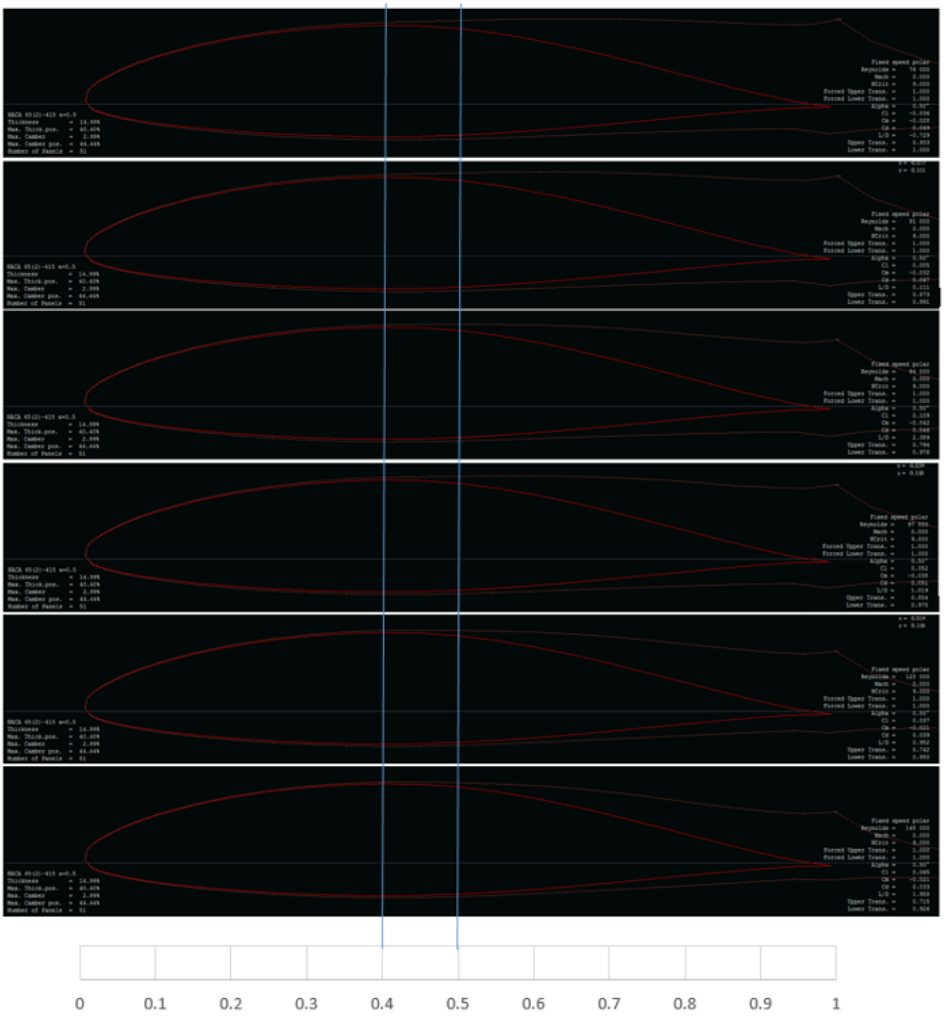

Figure 4.31: XFoil results for NACA 65-415 displaying estimated separation location for Reynolds numbers (from top to bottom) 76,000, 91,000, 94,000, 97,000, 120,000, and 145,000. The results indicate that the separation point is delayed with increase in Reynolds number, as seen in the experiments.

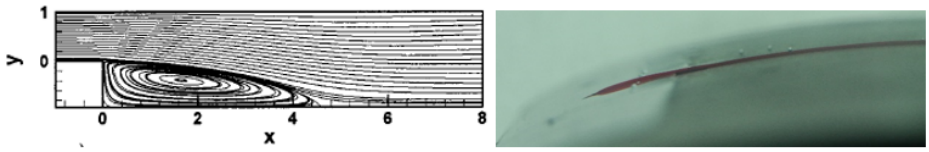

Figure 4.32: (left) Flow behavior over backward-facing step at a step-height-based Reynold number of 200, which corresponds to the momentum thickness scale [98]. (right) momentum thickness backward-facing step test.

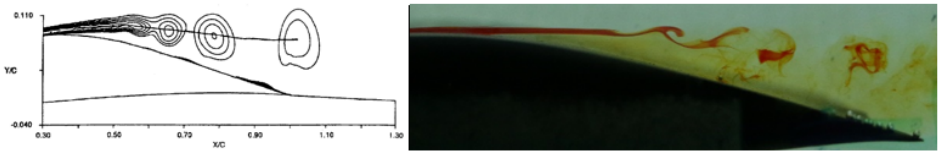

Figure 4.33: (left) Separation flow and vorticity contours over adverse pressure gradient for Reynolds number of 60,000 [99]. (right) Ideal wing surface dye flow visualization of Reynolds number of 94,000.

given the tests where the flow remained attached to the end of the frame and the consistency between the ideal and backward-facing step geometry results, it was likely that the improved separation characteristics were valid and additional tests should be conducted to further solidify these results. Assuming that the CVG geometry does indeed prolong attachment in the adverse pressure gradient region, the mechanism responsible for the delayed separation could be considered. According to Abbott and Von Doenhoff, (1959) improving separation characteristics is obtainable by adding energy into the boundary layer or removing low energy flow from the boundary layer [1]. Therefore, it is likely that this device manipulates the energy distribution in the boundary layer to delay separation. This characteristic was only noticeable for the momentum scale geometry, which maintained laminar flow over the step and may not have been noticeable or present for turbulent or larger Reynolds number flows. Without further investigation, the specific mechanisms employed by the CVG geometry to delay separation could not be identified. However, the notion suggested by the CVG manufacture, that the unique geometry produces streamwise vorticity downstream, was consistent with the method of adding energy to the boundary layer in order to delay separation.

The limited amount of comparable results from of the wall-unit scale geometry complicated the analysis of the collected data, as discussed previously. However, some meaningful qualitative observations were made regarding the larger scale geometry. First, the lower velocity case produced similar flow structures between both the backward-facing step and CVG, where the turbulent behavior in the adverse pressure

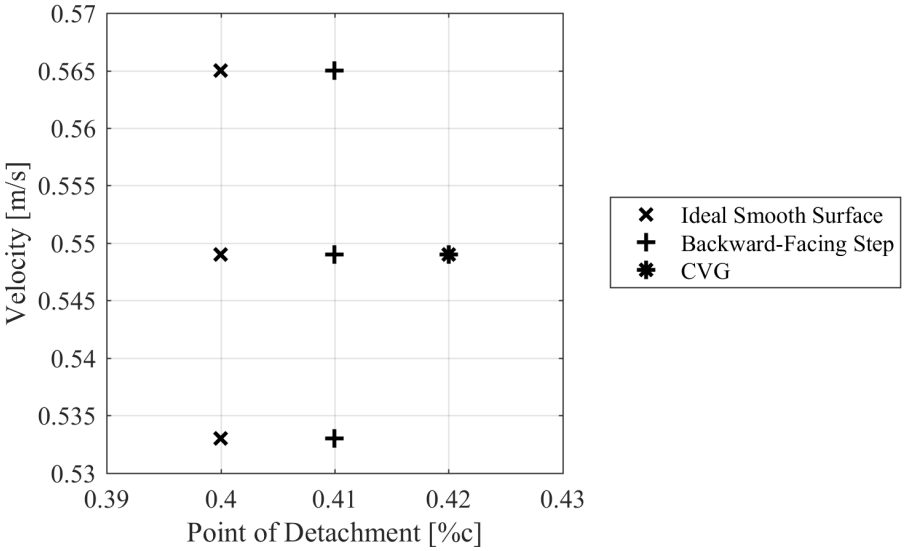

Figure 4.34: Separation location for the ideal wing surface, the backward-facing step, and the CVG geometry.

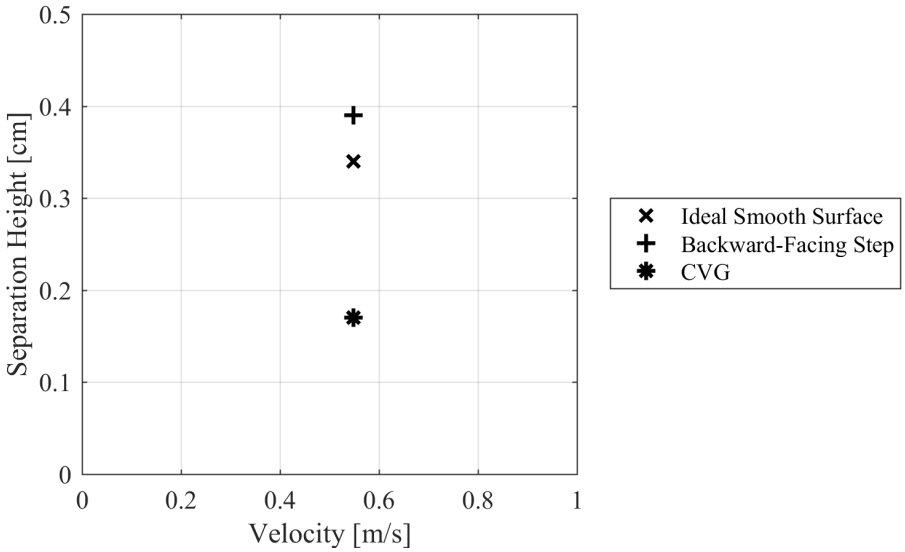

Figure 4.35: Separation height from the trailing edge for the ideal wing surface, the backward-facing step, and the CVG geometry

gradient region was seemingly random and well attached to the end of the camera frame. The similarity between these two geometries for the low Reynolds number case is shown below in Figure 4.36.This was to be expected, for flow passed a large backward-facing step, relative to the incoming Reynold number. In contrast, the higher Reynolds number tests produced different behaviors between the backward-facing step and the CVG geometries, as shown in Figure 4.37. The difference between the flow behaviors was that the backward-facing steps separation produced an inconsistent and unsteady behavior close to the wing surface and that the CVG geometry consistently had no dye close to the wall over the aft section of the wing. This was significant because it suggested that the turbulent flow structure associated with the CVG geometry was a more organized and steady (or repeatable) turbulent behavior than the backward-facing step geometry. Describing a turbulent flow as organized and steady, or consistent, is not proper. For example, Tennekes and Lumley, (1972) described turbulence as a dissipative irregular diffusive flow that occurs in a continuum at high Reynolds numbers with three dimensionally fluctuating vorticity elements. Because the behavior of the flow associated with the CVG geometry did not appear to be in good agreement with all of the defining features of turbulent flow behavior (irregular), it seemed that the CVG produced a hybrid flow condition or introduced an additional, dominate characteristic to the flow; such as vorticity [80]. Additionally, Yarusevych et al. (2009) stated that the structure of the airfoil wake region is heavily dependent on the Reynolds number and flow regime, which were both held constant between these two tests [100]. This suggested that the flow was influenced by the geometry rather than other potential factors. Nothing further can be said or claimed about this flow behavior without more tests for comparison or detailed quantitative analysis. However, the CVG flow structures and their comparison to a traditional backward-facing step were interesting and provided more questions than answers.

The two scaled geometries presented here produced inherently different flows.

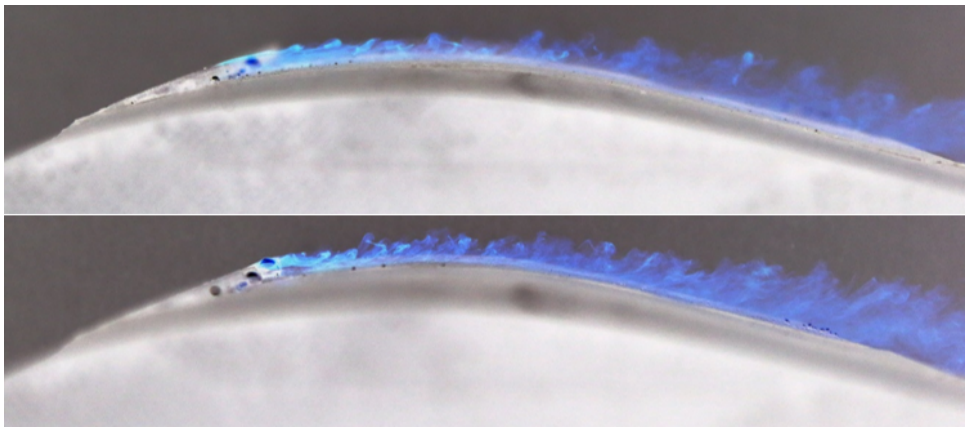

Figure 4.36: (top) Backward-facing step dye flow visualization at 40 cm/s. (bottom) CVG dye flow visualization at 40 cm/s.

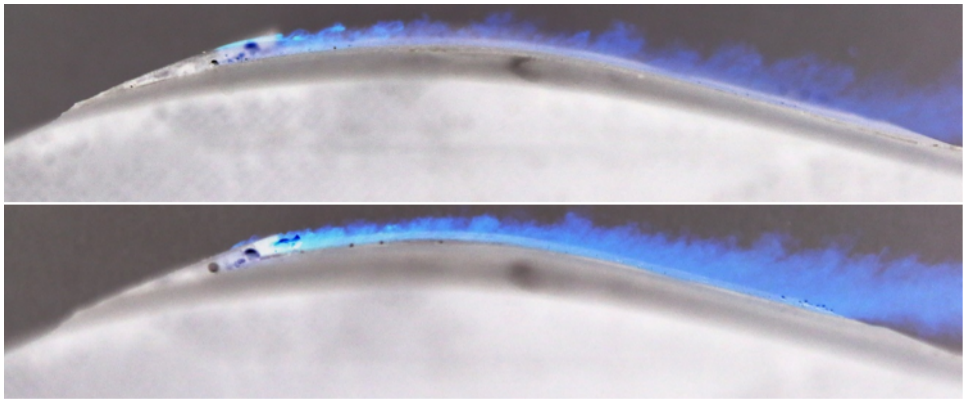

Figure 4.37: (top) Backward-facing step dye flow visualization at 70 cm/s. (bottom) CVG dye flow visualization at 70 cm/s

Specifically, the momentum scale geometry was small compared to the tunnel speed, which allowed the flow to remain laminar, as opposed to the wall-unit scaled geometry, which forced the flow to immediately transition to turbulence. This forced transition changed the entire behaver of the flow, because turbulent flow naturally improves separation characteristics and is unsteady. Therefore, the comparison between these two scaled geometries was difficult, as discussed in the previous section. Additionally, the angle of attack between the testing regiments was not held constant. Because the angle of attack was not the same for all tests, the chord-wise pressure gradient was likewise not the same for all the data collected. Therefore, comparison between tests accomplished separately cannot be directly compared.

However, from the limited amount of useful data presented here, there were some interesting discoveries that could be adequate evidence to justify further testing. The momentum scale results provided limited evidence that the CVG geometry noticeably improved downstream attachment. Delaying detachment in the adverse pressure gradient region of the airfoil can greatly reduce pressure drag. This prolonged attachment was only measurable for the momentum scale geometry and did not seem to carry over to the larger wall-unit scale geometry which tripped the flow to turbulence. Although, the wall-unit scale results qualitatively indicated that, for the CVG geometry, the downstream flow structure was more organized and contained a combination of the turbulent and laminar characteristics. The unique flow structure produced downstream from the CVG in the adverse pressure gradient region was obviously different than the flow structure produced from the backward-facing step, which resembled traditional turbulence. This flow organization associated with the CVG geometry could be an indication of coherent structures; however, without further investigation or a measurable quantity, the exact nature of the unique flow pattern could not be determined. Therefore, this study indicated a need for further investigation of the CVG geometry on idealized flat plates or a more repeatable varied pressure gradient

test bed. Additionally, future work should build upon the results and mitigate the limitations presented here.

Chapter 5

Computational

5.1 OSU Computational Resources and Software

5.1.1 OSU HPCC Cowboy Cluster

The High-Performance Computing Center at Oklahoma State University has a computational cluster, Cowboy, supported in part by the National Science Foundation grant OCI1126330. The Cowboy cluster consists of 252 compute nodes each with dual Xeon E5-2620 6-core 2.0 GHz CPUs and 32 GB of RAM. Additionally, the cluster has two big memory, fat, nodes each with 256 GB of RAM. The aggregated peak speed is 48.8 TFLOPs, with 3,048 cores and 8,576 GB of RAM. Cowboy also contains 92 TB of globally accessible high performance disk space. The cluster is networked and may be accessed through SSH session from anywhere with an internet connection. This resource was fundamental for the computational requirements of this investigation, and at times single handedly utilized 90 of the 252 compute notes, 1080 cores, roughly one third of the entire cluster [101].

5.1.2 Star-CCM+ Software

Star-CCM+ was a commercially available CFD software program designed for use in engineering applications. It had a built-in CAD package which allowed simulated geometries to be constructed within the simulation software, or CAD geometries could be imported in to simulation software as parasolid files. The CAD package employed with Star-CCM+ included the most basic set of tools and was sufficient for sim-

ple geometries, but complicated geometries would benefit from being constructed in more advanced CAD software and then imported into Star-CCM+. The software had automated mesh algorithms capable of producing Tetrahedral, Timmer Hexahedral, and polyhedral unstructured meshes. These automated algorithms may also produce layered high-aspect ratio prism cells near wall boundaries to better resolve the boundary layer formation. The automated mesh options provided by the software were convenient and provided a fair level of control in the mesh generation possess. However, the automatic nature of automated meshes caused some issues from time to time, especially concerning prism layer cell formations around angles. In addition to the automated mesh operations, Star-CCM+ provided the tools to create directed meshes, which are structured grids that were created by sweeping. The directed mesh method allowed for more stringent control grid design process and was ideal for ducted or piped flows. Flow domain designation in Star-CCM+ allowed the use of multiple regions, boundaries, and even types of physics within a single simulation. For example, two regions of differing mesh type and turbulent models may be intersected and interpolation functions may simulate the flow from one region to the next. This was a powerful tool and the flexible nature allowed for unique simulation design that had fewer limitations than other simulation software packages. Inlets, outlets, baffles, walls, symmetry planes, periodic boundaries and many other boundary conditions exist. A large set of models, from simplistic two-dimensional traditional laminar flow to more advanced three-dimensional turbulence models, such as RANS, LES, and DES along with a list of variants for each, were also available. It also had an impressive number of graphical data representation tools available for visualizing large amounts of data, the ability to write custom functions for nearly any input parameter, and even the ability to record macro scripts of commonly repeated commands in order to save time. This software offered as much utility, flexibility, and control as possible without being an open source code. However, its strengths were

also its weaknesses. A new user could produce visually impressive results in a matter of hours with little to no previous experience in CFD, and a seasoned CFD engineer may spend years learning all of the facets of the softwares capabilities, limitations, and controls. Star-CCM+ was selected as the CFD software for this research work based on the number of tools, models, and documentation readily available. It was instrumental in the exploratory CFD work accomplished so far, as it allowed various various models, boundary conditions, and mesh types to be tested all within the same software.

5.1.3 Pointwise Grid Design Software

Pointwise is a grid and mesh software that provided the user full control in creating structured hexagonal grids. The software allowed 2D and 3D-grids to be constructed with any desired spacing, growth rate or, specific cell size. The two grids may then be grown, swept, layered, projected or even smoothed using a variety of tools. Pointwise specialized in block-type structured grid topologies which allowed entirely structured gridding of complex geometries, such as the three dimensional turbine blade shown in Figure 4.37. It was also capable of producing automated unstructured tetrahedral and high aspect ratio prism layer type meshes. The software had some more advanced toolsets which were not fully utilized by the work presented here, which focused on using pointwise for complex structured grid topologies. Pointwise was selected for the purpose of producing highly controllable detailed block-type structured grids around the triangular CVG geometry.

5.2 Flat-Plate Re_X Scaled Simulation

The first attempt to model the flow over the CVG geometry was made after conducting the dye flow visualization tests discussed in Section 4.4. The goal of the simulation was to reproduce the flow patterns seen during the dye testing, and deter-

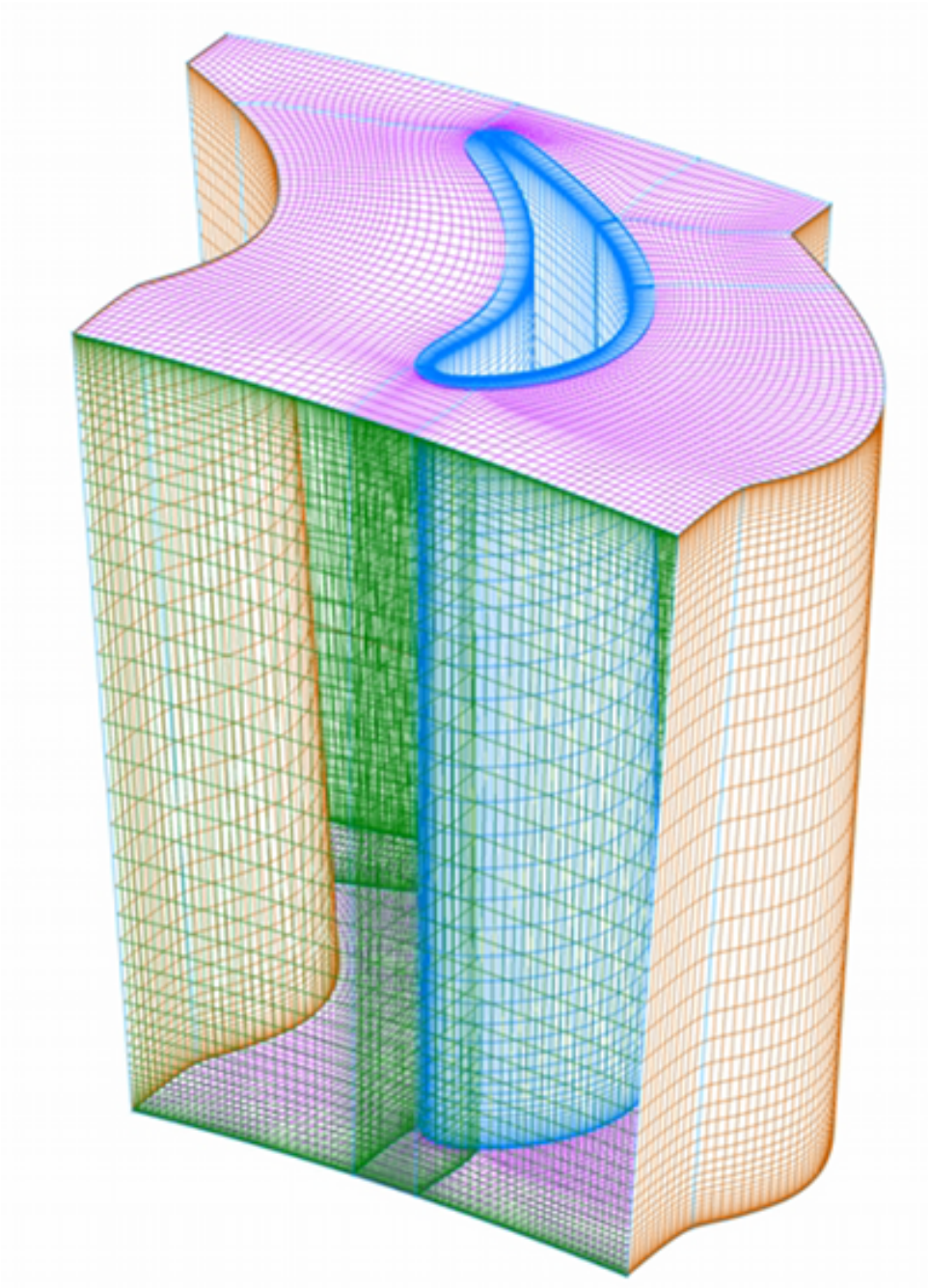

Figure 5.1: Example of advanced structured grid capability provided by Pointwise [102].

mine if computational methods could be an asset to the research effort. This attempt at simulating the flow over the CVG was accomplished early in the program and without any prior CFD experience. Therefore, the methods presented for this simulation were not ideal, but did guide the direction of the research effort as a whole. The simulation modeled the entire water tunnel test section, a rectangle, with the thin flat plate test model placed in the middle. The simulation flow properties, domain definition, mesh design, physics, and computational specifications are given in Table 5.1, 5.2, 5.3, 5.4, and 5.5, respectively. Generally, the simulation mimicked water tunnel flow characteristics and geometry with a thin test plate installed as shown in Figure 5.2. This simulation utilized the RANS SST K-Omega model discussed in Section 3.6, with a non-idealistic mesh design. The increased cell sizes resulted in a less computationally intense simulation that was solved with a standard workstation. The results of the simulation did however produce similar flow behavior visualized with streamlines in Figure 5.3, but the wall shear stress results were not in agreement with flight test wall shear patterns. This was to be expected considering the crude approach, and due to the inconsistent wall shear stress results, this simulation was not examined further. Yet, the simulation did provide an example of what under-resolved (or inaccurately modeled) flow can produce, which should always be evaluated by methods in order to avoid overconfident or misleading results. For example, the streamlines looked similar and, without evaluating the wall shear stress patterns (or quantitative data preferably), CFD simulations could have caused overconfidence in the level of accuracy, which may not be founded, as in the case of this simulation. This simulation also indicated that computational methods could be valuable to the research effort when properly conducted, and with that in mind, additional training and computation studies were accomplished.

Parameter	Value	Unit
H	~ 0.367	mm
L	~ 29	mm
W	~ 17	mm
X	~ 420	mm
δ_{99}	~ 11	mm
y^+	~ 0.022	mm
H/δ_{99}	~ 0.033	mm
H/y^+	~ 17	mm
ρ	$\sim 1,000$	kg/m^3
μ	$\sim 8.89 \times 10^{-4}$	$Pa\text{-}s$
ν	$\sim 8.89 \times 10^{-7}$	m^2/s
T	~ 300	K
U	~ 0.9	m/s
Re_H	~ 371	
Re_X	$\sim 4.25 \times 10^5$	

Table 5.1: Re_X simulation flow properties (all properties which are a function of x-distance are given at the step location).

Dimension	Length	Unit	(-) Boundary Condition	(+) Boundary Conditon
x-distance	~ 1.42	m	velocity inlet	pressure outlet
y-distance	~ 0.3	m	no-slip-wall	no-slip-wall
z-distance	~ 0.3	m	no-slip-wall	no-slip-wall

Table 5.2: Re_X simulation domain specifications.

Parameter	Value or Description	Unit
Mesh or Grid Type	unstructured polyhedral	
Total Cell Count	$\sim 700 \times 10^3$	cells
Δx	~ 100	y^+
Δy (first wall-normal cell)	~ 100	y^+
Δz	~ 100	y^+

Table 5.3: Re_X simulation grid specifications.

Parameter	Value or Description
Space	three-dimensional
Spatial Discretization	finite volume
Spatial Discretization Scheme	2^{nd}-order upwind
Time	steady
Flow	coupled
Equation of State	liquid
Viscous Regime	turbulent
Turbulence Model	RANS SST K-Omega
LES Wall Treatment	all y^+ wall treatment
Linear System Iterative Method	bi-conjugate gradient stabilized method

Table 5.4: Re_X simulation specifications.

Item	Value or Description
Number of Cores	8
Average Time per Iteration	4.7 s
Total Physical Time	3 hr
Total CPU Hours	75,000

Table 5.5: Re_X simulation computational resource specifications.

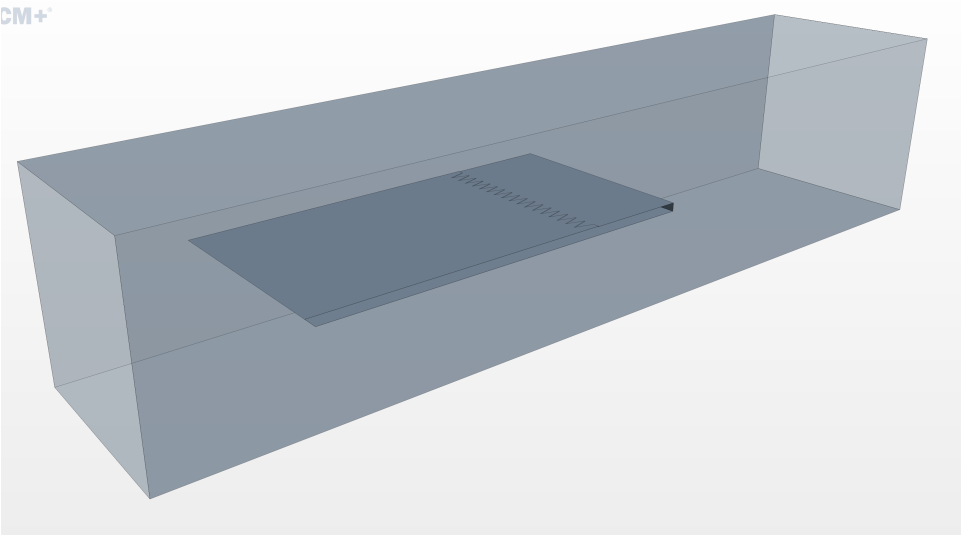

Figure 5.2: Re_X scaled flat-plate simulation computational domain.

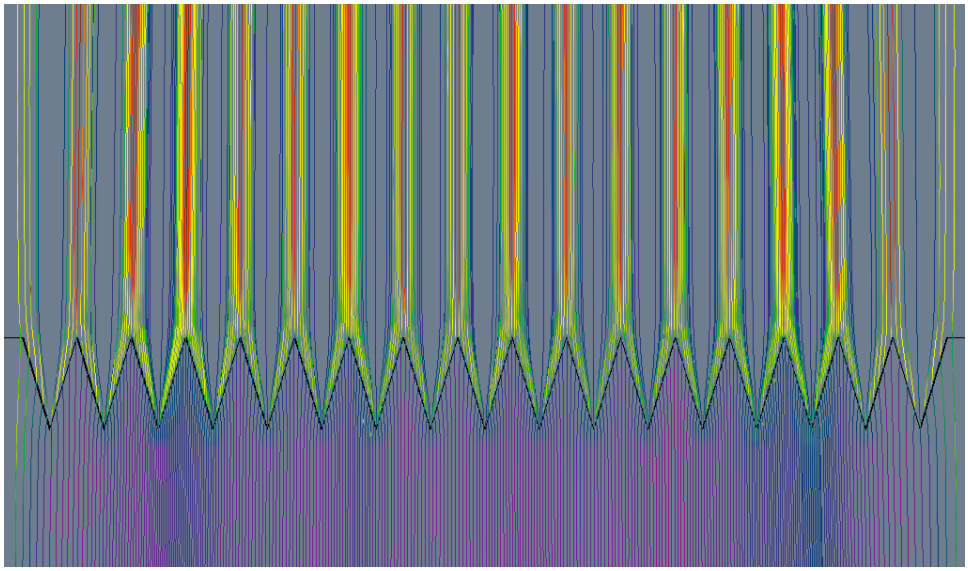

Figure 5.3: Re_X scaled flat-plate simulation crude results, which produced streamlines that behaved similarly to the flow from experimental dye tests (flow is up).

5.3 NACA 64A-212 Airfoil Simulation

The scope of this study was to accurately model a three-dimensional wing section with known coefficients of lift and drag, for the purpose of identifying effective wing section meshing methods. The NACA 64A-212 airfoil, which is the wingtip section of the Edge SOKO G-2 Galeb flight test platform, Reynolds numbers of three, six, and nine million, and angles-of-attack ranging from negative six to positive six were selected for this study because wind tunnel test results were readily available [1]. The goal of this study was to lay the foundation for future testing of the CVG device using the NACA 64A-212 airfoil section boundary layer and pressure gradient information, which could be obtained from an accurate CDF simulation.

5.3.1 Experimental Methods

The airfoil section geometry used in this study was an un-swept, un-tapered, constant 1.4 meter chord length NACA 64A-212 as shown in Figure 5.4. This geometry was modeled in Solidworks and imported into Star-CCM+. The domain was created in the built-in 3D-CAD client, which facilitated easy part subtraction form the flow domain,

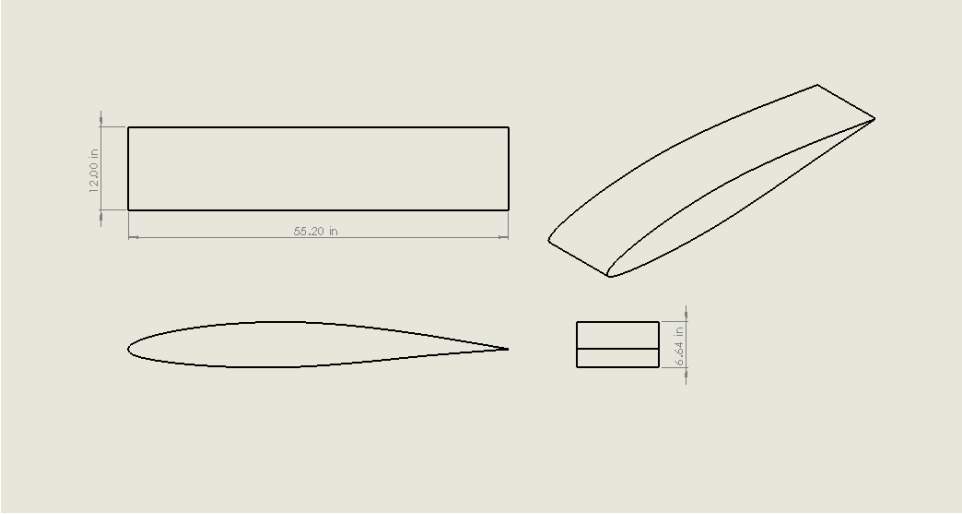

Figure 5.4: NACA 64A-212 airfoil simulation constant chord section drawing with dimensions.

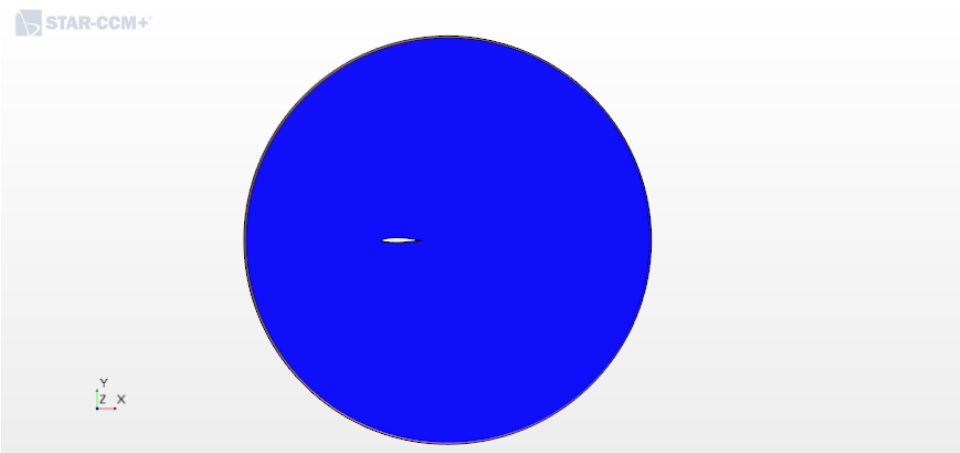

Figure 5.5: NACA 64A-212 airfoil simulation computational flow domain.

which is shown in Figure 5.5. The flow domains parallel Z-plane boundaries were defined as periodic to simulate a wing section of infinite span. The wing surfaces were defined as regular walls and the outer boundaries were given freestream conditions. The automated trimmer mesh was used in this study because the flow direction was fairly stable in the Positive-X direction through the domain for the given scenario. Twenty prism layers were also used on the surface of the wing to clearly resolve the boundary layer.

The grid for this study started as a bullet-shaped domain section utilizing an overset mesh for easy angle-of-attack changes. The curved front also allowed artificial

angle-of-attack change by changing the intel flow direction. The central goal for building the mesh in this manner was to eliminate the need to re-mesh between angle-of-attack changes. However, this design wasted mesh resources by requiring the overset mesh to be larger and finer than ideal. Also, the wake refinement cone had to be large enough to encompass the wake region for the extreme angle-of-attack cases. These two factors increased the total cell count to a value larger than desired causing the computational time to drastically increase, which negated the time saved by avoiding the mesh recalculation. Not to mention that the mesh employed was not refined enough, particularly near the trailing edge of the wing section, to accurately resolve the lift and drag coefficients of the section. Therefore, this mesh design was abandoned.

The next attempt focused on mesh efficiency, with the goal of placing mesh elements only where needed and eliminating wasted refined mesh area. For this reason, a circular mesh was use, which eliminated one-third of the total domain size as seen in Figure 5.6. Additionally, this mesh design did not use an overset mesh to accomplish changes in angle-of-attack. Instead the model geometry was modified using a 3D-CAD design parameter, subtracted from the domain, and finally meshed. A simple Java script was used to perform these tasks in-between solutions for autonomous data collection of multiple test points in one simulation. This Java script could be further refined with a "for-loop" to eliminate the repeated line commands in the future; however, for this simulation's needs it was quicker to copy the commands for the needed angle-of-attack changes.

The flow locations needing the most refinement were identified through multiple volumetric control renditions. The tailing edge and wake region of the wing were the most sensitive to grid size. This was why the volumetric controls were clearly biased toward refining the wake region of the wing section, especially close to the trailing edge. The mesh study initially consisted of multiple size options. Three mesh

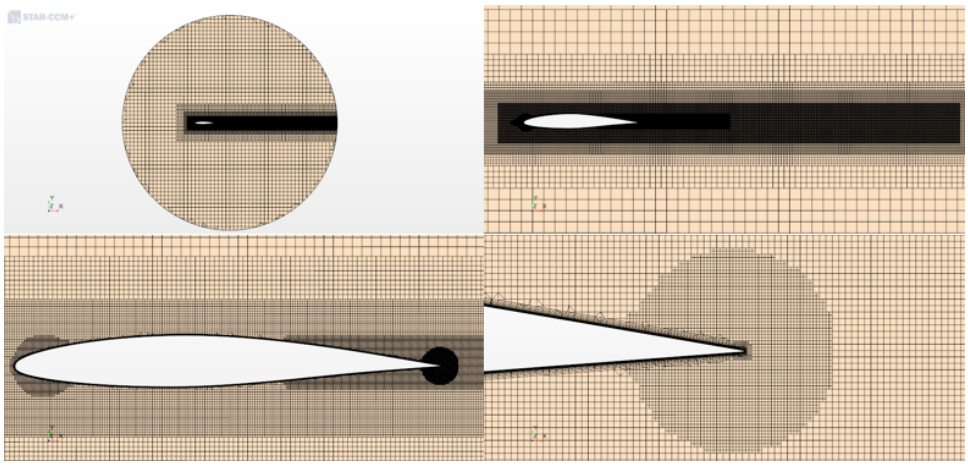

Figure 5.6: NACA 64A-212 airfoil simulation mesh design.

refinement levels were selected for a grid independent study, meshes "D", "G", and "I" consisting of roughly two, six, and ten million cells respectively. A ten million cell count was considered the maximum acceptable grid size possible for this study, and it was to be avoided if possible. This distinction was made because the goal of the study was to keep the mesh count as efficient as possible so that the geometric model could be expanded in the future without becoming computationally unfeasible. The grid independent study investigated the simplest case of a freestream flow with a Reynolds number of three million and the wing section at zero angle-of-attack. The results for the grid independent study revealed that the "D" mesh was far too coarse to resolve drag coefficient with any level of accuracy. However, the "G" and "I" mesh results were within 2 percent difference from each other for both lift and drag coefficient, but with a difference of 3 million total cells. Therefore, the "G" mesh was selected as the most efficient option for this study, as the "I" mesh was approaching the 10 million mark.

5.3.2 Results and Discussion

Three simulations of different inlet conditions (Reynolds numbers 3, 6, and 9 million) were constructed to sweep through eleven angles-of-attack (-6, -4, -3, -2, -1, 0, 1, 2,

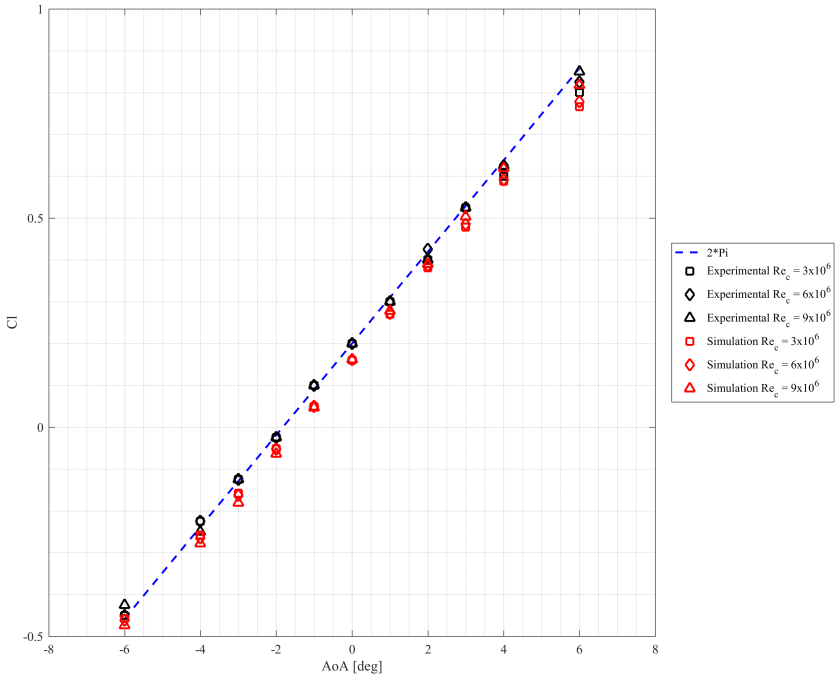

Figure 5.7: Cl over angle-of-attack simulation results compared to experimental results [1].

3, 4, and 6). Each simulation took 416 CPU hours to complete the eleven angle-of-attack sweep. The coefficient of lift and coefficient of drag were calculated for each test point and plotted over angle-of-attack, as shown in Figure 5.7 and Figure 5.8. The results obtained in this study were not as accurate as desired. However, investigating the results shed further light on the matter. From inspection, it was immediately obvious that the coefficient of lift results were nearly twice as accurate as the coefficient of drag results. This was not uncommon, because resolving accurate drag was the difficulty in most computational studies. In fact, the two-pi lift curve slope approximation, resulted in only 6 percent error from the experimental values. Therefore, if the results of this study were taken solely at face value, the conclusion would be that the simulation was inaccurate. However, a closer look revealed that there were numerous error trends in the data set.

The percent error in the coefficient of lift results were plotted as a function of

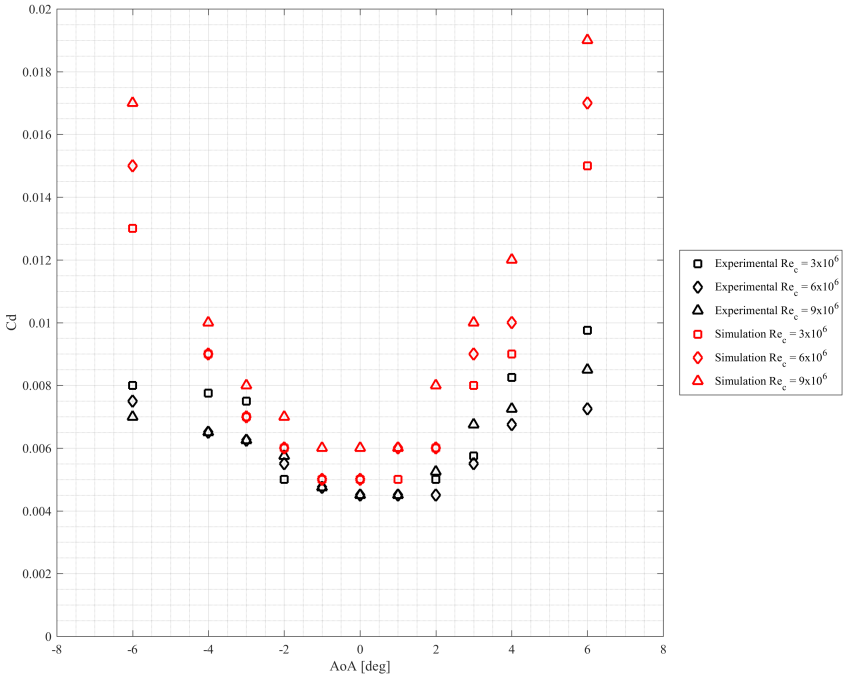

Figure 5.8: Cd over Cl simulation results compared to experimental results [1].

angle-of-attack in Figure 5.9. From this representation it was clear that the results for negative angle-of-attack had an error which was focused around negative 2 degrees. The NACA 64A-212 airfoil had a steeper slope past the fifty percent chord mark, as was common for transonic wing sections. This difference in the geometry caused the boundary layer to expand and separate farther forward at negative angles-of-attack as opposed to positive angles-of-attack, which is depicted in Figure 5.10. This early separation seen with negative angles-of-attack was not properly resolved with only the prism layer mesh in that region. Therefore, the coefficient of lift results for the negative angles-of-attack should be further resolved in future studies. If these less accurate results were removed from the data set, the new average percent error of the coefficient of lift data would be nearly three times less for all three Reynolds number simulations, as shown in Table 4.

The coefficient of drag results were the least accurate of the study, and are plotted

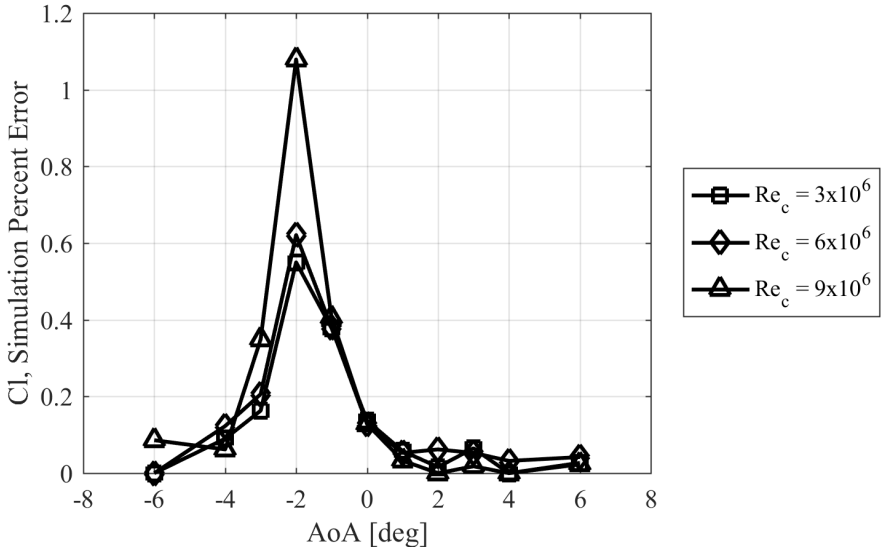

Figure 5.9: The percent error of the coefficient of lift results as a function of angle-of-attack.

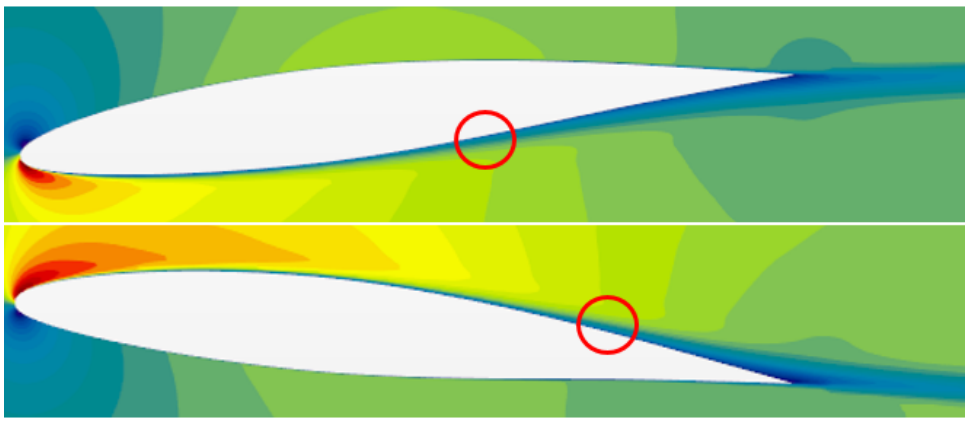

Figure 5.10: (bottom) Location of boundary layer expansion and separation for positive and (top) negative angles-of-attack.

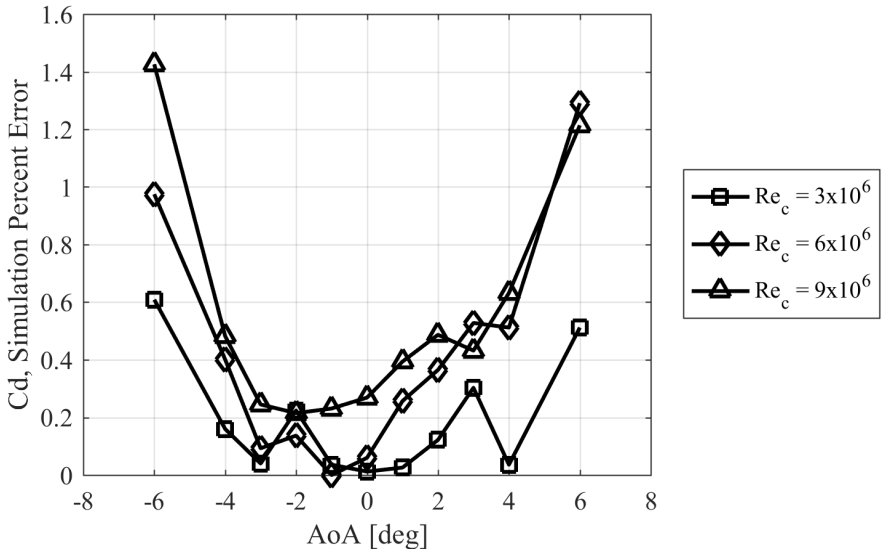

Figure 5.11: The percent error of the coefficient of drag results as a function of angle-of-attack.

as a function of angle-of-attack in Figure 5.11. From the plot it is apparent the extreme angle-of-attack cases, greater than positive three and less than negative three, were the least accurate from the data sets. This is further examined in Figure 5.12, where it shows that the volumetric wake refinement region was not encompassing the wake of the airfoil at its new location. In future studies the wake refinement regions should be translated vertically using the java scripting method that was used to rotate the airfoil and its volumetric controls for angle-of-attack changes. This change should increase the accuracy of the drag calculation at the boundary angles-of-attack. If the outer four test points were not considered, the average percent error of the coefficient of lift was nearly cut in half.

From this data set, another trend emerged, the coefficient of drag results were consistently less accurate for higher Reynolds numbers. This was most likely due to needing higher mesh refinement as the flow velocity was increased. It should be noted that the mesh refinement study was performed for the three million Reynolds number case at zero angle-of-attack only. Future studies should consider all Reynolds numbers, using Reynolds number specific grids for each simulation and boundary

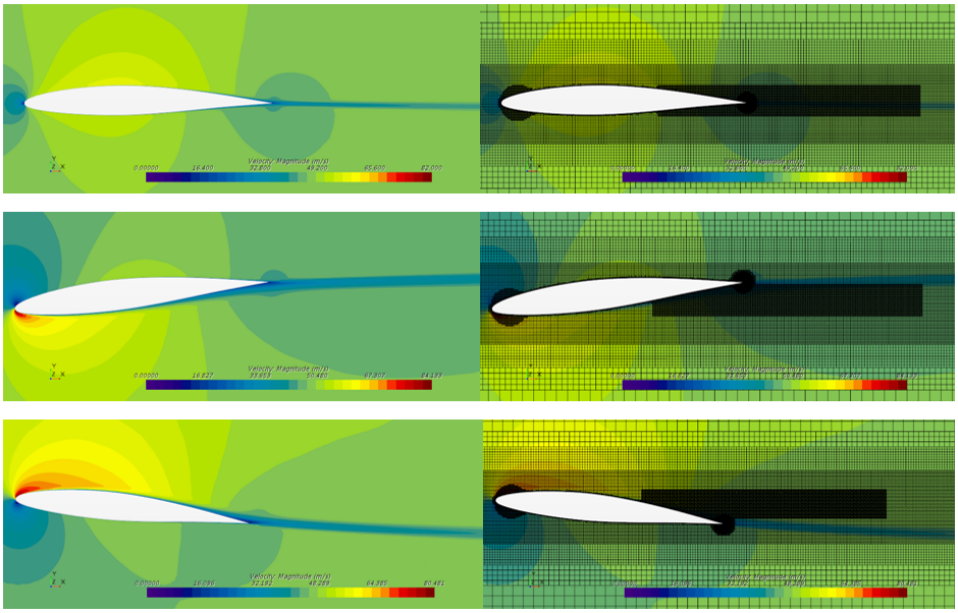

Figure 5.12: (top) Wake and mesh locations for 0 angle-of-attack, (middle) -6 angle-of-attack, and (bottom) 6 angle-of-attack.

angle-of-attack values for the grid independant study instead of the median value.

In conclusion, the results of this study identified many important considerations for accurately meshing and modeling airfoil geometries when mesh and computational efficiency were a high priority. These include high mesh resolution of the trailing edge and wake region, wake region volumetric controls that translated according to angle-of-attack in order to resolve the wake affectively, special attention for geometric differences in the bottom surface that promoted earlier separation, and further mesh resolution for higher speed flows. Additionally, it was noted that a generic overset grid used for all angles-of-attack was less efficient for our case than computing a mesh specifically designed for each angle-of-attack. These realizations are a good starting point for another rendition of this study to further hone in on efficient and accurate coefficient of lift and drag modeling. Additional studies and refinements are needed for these easily validated simulations before moving to more complicated geometries containing sweep, taper, and wing tip effects, as is intended in the long term scope of this project.

5.4 Flat-Plate Re_H Scaled Simulation

The simplified CVG geometry examined in this study was an un-swept triangular pattern. A characterization of the shedding frequency and the formation of hairpin-like vortices were addressed in comparison to those of a traditional backward-facing step. This simulation utilized the scaled approach discussed in Section 3.10.2, applied it to the Piper Cherokee flight test platform flow properties, and reproduced the same step-height-based Reynolds number of 1,650. The commercially available CFD software Star-CCM+ was used to produce the unstructured poly mesh and solve the unsteady Detached Eddy simulation. The goal of this study was to attempt to reproduce the qualitative results seen during the experimental study discussed in Section 4.5. A validation was performed with experimental results of a backward-facing step flow. The results of the study indicated that the CVG Strouhal number was consistent with those of traditional backward-facing steps. Additionally, the hairpin-like vortex structures, which normally occur randomly downstream from backward-facing steps, were shown to have their behavior manipulated by the CVG geometry. This suggested that the CVG geometry organized the turbulent structures and could drastically improve drag characteristics. Future work should improve upon the computational design presented here and take into account the limitations discussed.

For this study the focus was on three specific sets of results. First, the qualitative results from previous flow visualizations accomplished, which are discussed in Section 4.5 and shown in Figure 5.13. This study resulted in clear visualization of the 4 main flow characteristics of a backward-facing step flow (shear layer, recirculation, rollup, and vortex shedding), and were used to compare with the simulation results. Second, the qualitative direct numerical simulation (DNS) results presented in Deubief and Delcayre (2000), which show the Q-Criterion for a backward-facing step flow and the random generation of hairpin-like structures downstream of a backward-facing step [103]. These hairpin-like structures are not well understood, and resembled the hairpin

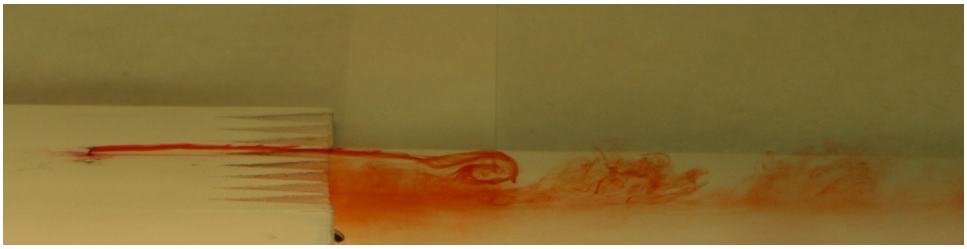

Figure 5.13: OSU water tunnel dye flow visualization over 1.0 cm CVG step at 10 m/s. The four flow structures associated with backward-facing steps are shown (shear layer, re-circulation, rollup, shedding).

vortices thought to be influential in turbulent production. However, these hairpin-like vortices were much larger than those associated with turbulent production (on the scale of the backward-facing step), but they likely behave similarly. For traditional backward-facing steps, the spanwise locations and spacing of these structures were shown to be random. Third are the experimental results of Liu et al. (2005), which were used to compare with the simulation results presented here [104]. The validation methods are discussed in more detail later on.

The physics evaluated in this study were simplistic, because the conclusions were largely qualitative. However, the Strouhal number (3.7) was evaluated and compared to the experimental values (∼0.07) for backward-facing steps [104]. Additionally, the simulation was scaled with Reynolds number of the step height and neglected Reynolds number of the streamwise location (Equation 3.2). Edge Aerodynamix's flight test platform was used to scale the CVG results, which operated at ∼66.8 m/s in nearly sea level (SL) conditions (density 1.23 kg/m^3 and viscosity 1.8×10^{-5} kg/m^3). The step height of the flight scale was 0.36 mm, which produced a step-height-based Reynolds number of ∼1,650.

5.4.1 Experimental Methods

This simplistic geometry was constructed with the built-in CAD tools. The CVG geometry section had one central isosceles triangle and a right triangle on each side, as shown in Figure 5.14. It was constructed with a 1 cm step height, 20 cm length

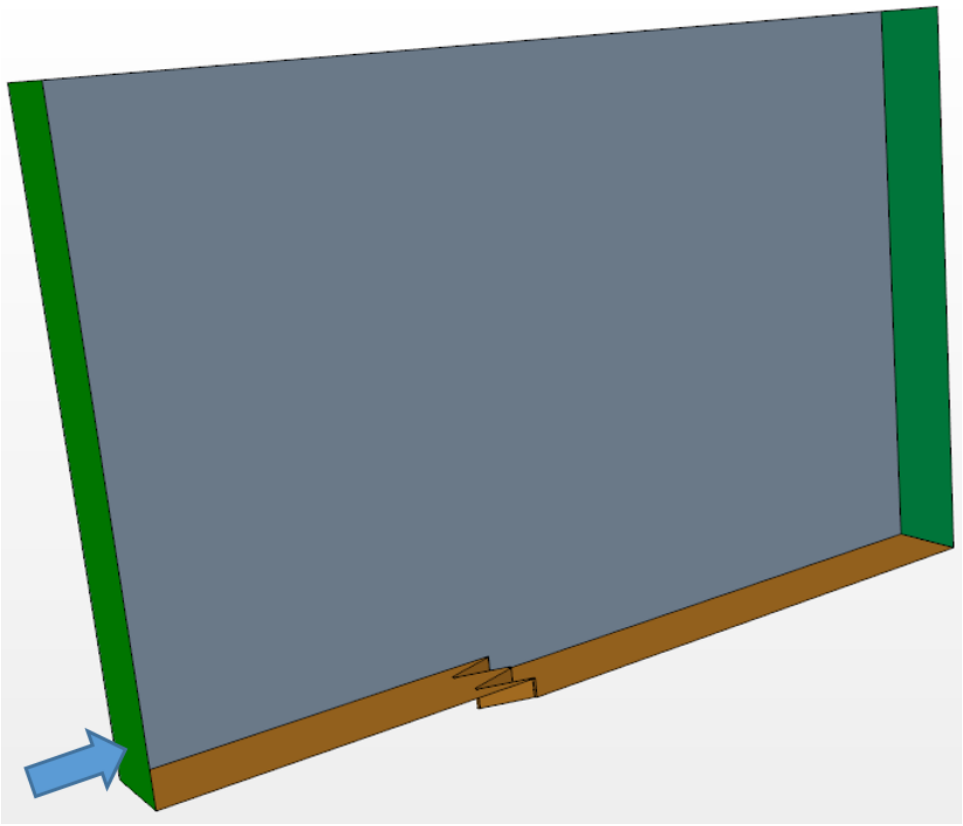

Figure 5.14: Re_H scaled flat-plate simulation computational domain with inlet to the left, wall and CVG geometry on the bottom, slip-wall on the top, periodic boundary condition in and out of the page, and pressure outlet to the right. The total domain volume is 50 by 4.2 by 40 cm (x, y, z: where z is up).

from the inlet to the most downstream step location (convex angles), a triangle height of 3.2 cm, and a isosceles triangle half-angle (also the right triangles hypotenuse angle) of 18 degrees. The width of the CVG geometry was 2.4 cm and was driven by the previously mentioned parameters. The flow domain, which had a length from inlet to outlet of 50 cm, a surface normal height of 40 cm, and a width into the page of 2.4 cm. The inlet boundary condition was to the left, outlet to the right, slip-wall on the top surface, no-slip-wall (surface of interest) on the bottom, and a periodic boundary condition was applied to the boundarys parallel to the page (grey). Flow conditions for the simulation were a velocity of 0.146 m/s, a density of water 1,000 kg/m^3, and a pressure (SL) of 101 kPa.

An unstructured poly mesh of 20 million cells was created, as shown in Figure 5.15.

The poly mesh was chosen to reduce error resulting from cell wall orthogonality, with the expected three-dimensionality of the flow near the CVG geometry. This mesh design had a wall-normal cell height of 3 mm, for flow with a wall-unit of roughly 1.2 mm. The wall-normal cell size of 3 mm was chosen to reduce the cell count. A defect in the mesh generation method produced a cell refinement banding, as seen in Figure 5.15, and heavily impacted the cell structure efficiency. The base cell size was 2.5 mm (the upper region of the domain). A refinement region reduced the cell size to 1 mm (the lower region) and a surface control reduced the wall surface mesh to 0.5 mm. The unsteady solution was calculated from 0 to 25 seconds, which corresponded to 3.5 realizations across the entire domain. A detached eddy simulation (DES) turbulence model was implemented, which utilized large eddy simulation (LES) for the large scale structures and the RANS SST K-Omega (mentor) model for small scale structures, as defined by grid size. This was a second-order, implicit, central-difference-scheme with a time-step of 0.01 and an average CFL value of 0.8. The iterative procedure used 10 inner iterations per time-step, resulting in 2,500 total iterations. This simulation was executed on the Oklahoma State Univerity Cowboy super cluster, utilizing 244 cores, and completed within 24 hours. The simulation flow properties, domain definition, mesh design, physics, and computational specifications are given in Table 5.6, 5.7, 5.8, 5.9, and 5.10, respectively.

5.4.2 Results and Discussion

The simulation was compared against experimental results from Driver and Seegmiller (1985). However, these experimental results were for a backward-facing step flow with a step-height-based Reynolds number of 36,000. Therefore, the exact simulation discussed previously, was modified by increasing the inlet velocity to produce a step-height-based Reynolds number of 36,000 in order to compare the results. It should be noted that the only changes made to the simulation were the inlet velocity,

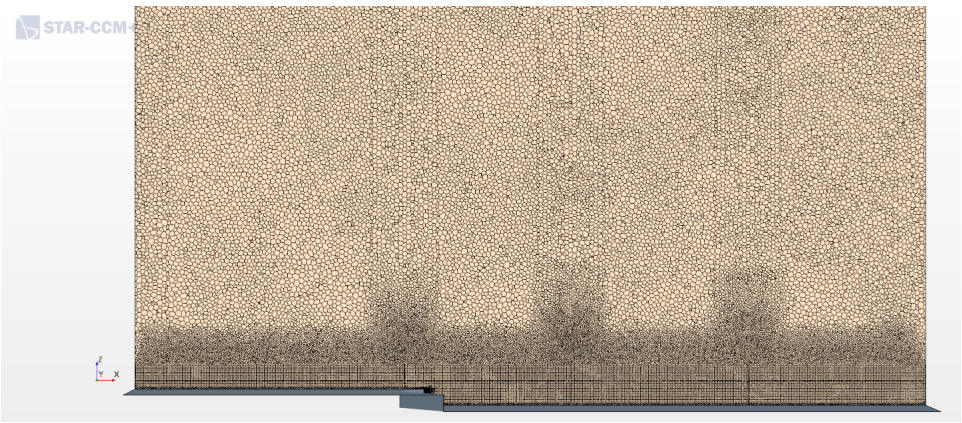

Figure 5.15: XZ plane slice of unstructured poly mesh. The total cell count was 20 million, and the first wall-normal cell had a thickness of ∼3 mm (where one wall unit is ∼1.2 mm). The banding in the mesh was a defect of the mesh generation and should be corrected for future studies.

Parameter	Value	Unit
H	~ 10	mm
L	~ 28	mm
W	~ 20	mm
X	~ 170	mm
δ_{99}	~ 4.4	mm
y^+	~ 0.11	mm
H/y^+	~ 91	mm
H/δ_{99}	~ 2.3	mm
ρ	$\sim 1,000$	kg/m^3
μ	$\sim 8.89 \times 10^{-4}$	$Pa\text{-}s$
ν	$\sim 8.89 \times 10^{-7}$	m^2/s
U	~ 0.146	m/s
Re_H	~ 1650	
Re_X	$\sim 30 \times 10^3$	

Table 5.6: Re_H simulation flow properties (all properties which are a function of x-distance are given at the step location).

Dimension	Length	Unit	(-) Boundary Condition	(+) Boundary Conditon
x-distance	~ 50	cm	velocity inlet	pressure outlet
y-distance	~ 4	cm	no-slip-wall	slip-wall
z-distance	~ 30	cm	periodic	periodic

Table 5.7: Re_H simulation domain specifications.

Parameter	Value or Description	Unit
Mesh or Grid Type	unstructured polyhedra	
Total Cell Count	$\sim 2 \times 10^6$	cells
Δx	~ 5	y^+
Δy (first wall-normal cell)	~ 5	y^+
Δz	~ 5	y^+

Table 5.8: Re_H simulation grid specifications.

Parameter	Value or Description
Space	three-dimensional
Spatial Discretization	finite volume
Spatial Discretization Scheme	hybrid bounded-central-differencing
Time	implicit unsteady
Temporal Discretization Scheme	1^{st}-order backward differentiation
Time-Step	0.01
Flow	coupled
Equation of State	liquid
Viscous Regime	turbulent
Turbulence Model	IDDES
Wall Treatment	all y^+ wall treatment
Linear System Iterative Method	bi-conjugate gradient stabilized method
Iterations per Time-step	10

Table 5.9: Re_H simulation specifications.

Item	Value or Description
Number of Cores	244
Average Time per Iteration	2.6 s
Total Physical Time	18 hr
Total CPU Hours	5,140

Table 5.10: Re_H simulation computational resource specifications.

which was increased from 0.146 m/s to 3.2 m/s, and the turbulence model, which was changed to steady RANS SST K-Omega (discussed in Section 3.6). This was significant, because the mesh was not modified, causing the near wall-normal cell size to be ∼500x larger than ideal. The validation case attempted to compare a two-dimensional backward-facing step flow to a three-dimensional CVG flow; therefore differences were to be expected. Coefficient of pressure from the inlet to the outlet in-line with the farthest upstream and downstream points of the step were measured. These were nondimensionalized with step height and compared to the experimental results, as shown in Figure 5.16. The coefficient of pressure results were not identical to the experimental results, but shared similar behaviors and magnitudes, and as such, builds confidence in the solution. Velocity profile data was also compared to experimental results at four step-heights upstream, and one and four step-heights downstream. These plots indicated that the simulation flow was turbulent and had a higher streamwise Reynolds number (500,000) than the experimental case (5,000). However, the behavior following the step was similar to the expected velocity profiles downstream of the step. Additionally, reattachment length was evaluated as shown in Figure 5.17. The reattachment length expected for a backward-facing step with a streamwise Reynolds number of 5,000 and a step-height-based Reynolds number of 36,000 is x/H = 6.26 ±0.10 [105]. The simulation results indicated that the reattachment for the CVG was unsteady and occured between x/H ≈ 10-13. The increased reattachment was most likely due to the three-dimensionality of the CVG geometry. This validation case was not ideal, but does shed light on the validity of the simulation results.

The shedding frequency analysis of the simulation results was accomplished by tracking the locations of the shed flow structures by pixel evaluation in Microsoft Paint. An example of the images compared is shown in Figure 5.18. The shedding structures were clearly visible and could be tracked downstream to the same point.

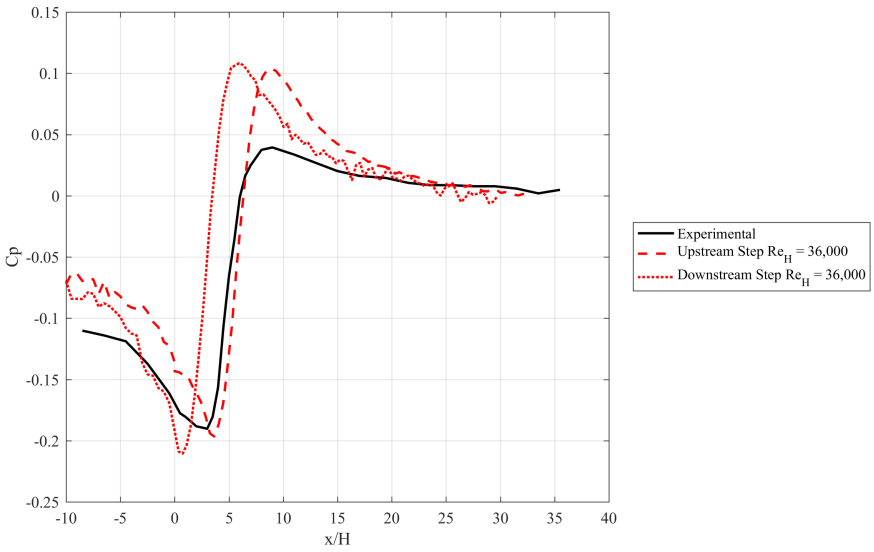

Figure 5.16: Validation simulation results for coefficient of pressure compared to experimental results for the same step-height-based Reynolds number of 36,000, where streamwise location had been nondimensionalized with step height and the step occured at $x/H = 0$. The Upstream Re: 36,000 refers to the coefficient of pressure on a collinear line with the upstream (concave) step and Downstream Re: 36,000 the coefficient of pressure on the plane of the downstream (convex) step; effectively bounding the extremes for step location.

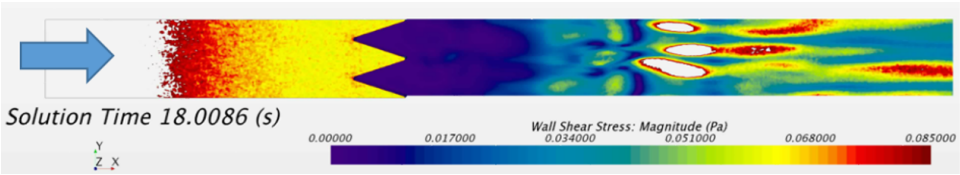

Figure 5.17: Wall shear stress magnitude at solution time 18.0 seconds was shown to visualize reattachment, which was defined as the downstream location (from the recirculation region shown immediately following the CVG geometry in purple) where coefficient of friction (or wall shear: $\tau_w = \frac{1}{2} C f \rho U_\infty^2$) was equal to zero. Reattachment was shown as a thin inconsistent purple region stretching across the span of the surface.

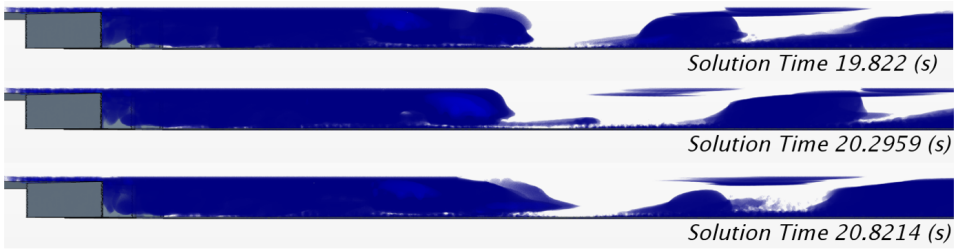

Figure 5.18: Time series of flow shows the analysis of the shedding frequency for one period. The "S" in "Solution Time" was used as a makeshift reference point in this figure (pixel count was used for actual data analysis). (top) Solution at 19.82 seconds with vortex centered over "S". (middle) Solution at 20.30 seconds with new vortex shedding and transvering downstream toward "S" occuring. (bottom) Solution at 20.82 seconds with vortex centered over "S". Therefore, the period by inspection was ∼1 Hz.

Then the time difference could be taken to solve for frequency. This method added uncertainty to the frequency measurement that was found to be ±0.7.

The results for Q-Criteria are shown in Figure 5.18. From these images and accompanying videos the shedding frequency was found to be roughly 1.0 Hz (±0.07) for the 1,650 step-based-Reynolds-number-simulation, which corresponded to a Strouhal number of 0.69 (±0.05). Therefore, the shedding frequency of the CVG was very consistent with known experimental results. This increased the confidence of the solution obtained and suggested that the behavior of the CVG was strongly rooted in the backward-facing step behavior. Additionally, the hairpin-like structures were shown to consistently shed in pairs lined up with the CVG geometry, as seen in Figure 5.19. This behavior suggested that the CVG do, in fact, manipulate the usually random coherent structures. This was significant because it implied that the CVG may control the turbulent production downstream of the step, which could drastically influence the skin friction characteristics or stabilize the downstream pressure and wake drag phenomena.

The mesh used in this computational study was less than ideal, and as such, limited the results. A wall-normal cell spacing of roughly 3 mm was used for both the 1,650 and 36,000 step-height-based Reynolds number simulations, where the ideal values (based on a wall-unit of 1) were 1.2 mm and 6 μm respectively. This was likely one

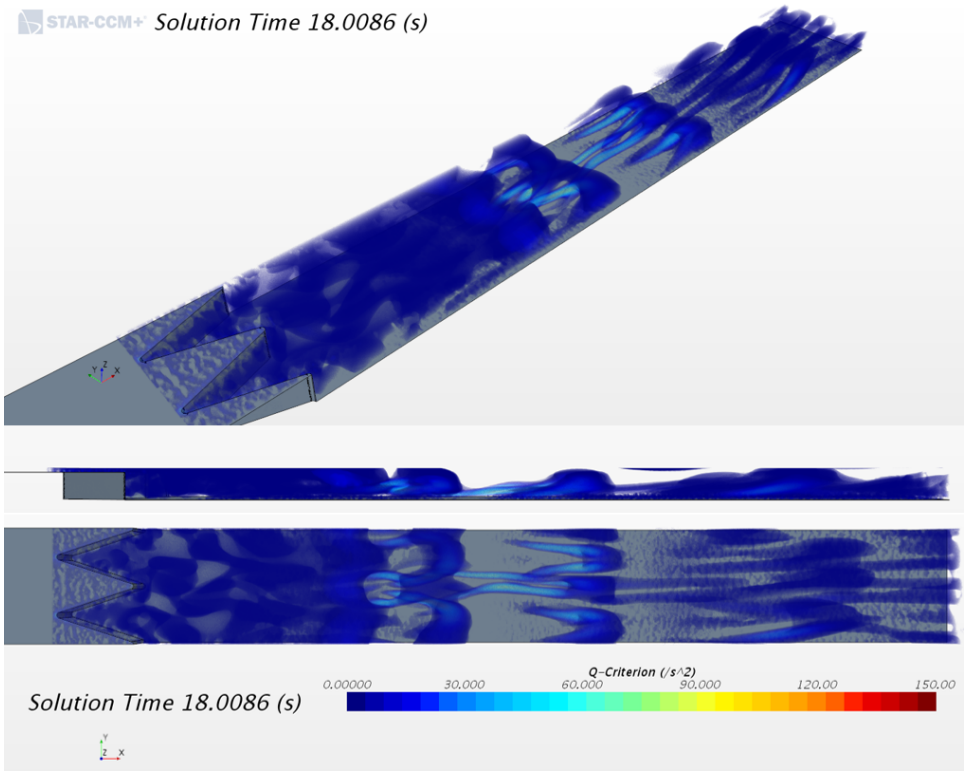

Figure 5.19: Q-Criterion visualization of flow over CVG at solution time 18.0 seconds for three views. (top) 3D view. (middle) Side view showed shedding frequency clearly. (bottom) wall-normal view indicated that hairpin-like vortex formations occur systematically, lined up with the CVG, which indicated that the CVG geometry manipulated the hairpin-like vortex structures, by organizing their process and ultimately organizing the turbulent flow behavior.

of the explanations for the less accurate validation results. Additionally, validation errors were caused by premature turbulent transition near the inlet, which may be corrected by manipulating the turbulence model. The step-based Reynolds number was held constant between the flight tests and the simulation, but the streamwise-distance-based Reynolds number for the simulation was two orders-of-magnitude less than the flight test. The simulation could be appropriately scaled with both step-height and streamwise-distance-based Reynolds number by prescribing an inlet condition, which models the developed boundary layer.

This computational study investigated the flow structures associated with the scaled CVG geometry as compared to experimental results for a backward-facing step. The simulation results were loosely validated, although there were limitations to the validation method as discussed previously. These results agreed qualitatively with the known flow behaviors associated with backward-facing steps. Additionally, the simulation reproduced a Strouhal number of 0.7 as expected for backward-facing steps from previous experimental studies. However, the downstream formation of hairpin-like vortex structures was shown to be driven by the CVG geometry, as opposed to the random formation common with backward-facing steps. This manipulation of the hairpin structures likely played a significant role in the drag reduction mechanism employed by the CVG. Future computational studies should overhaul the simulation based on the limitations discussed previously and incorporate flat plate and backward-facing step simulations for comparison.

5.5 RAE 2822 Transonic Airfoil Simulation

Typically, the initial aerodynamic design, subsequent testing, and simulation of an aircraft wing assumes an ideal wing surface without imperfections. In reality, however the surface of an in-service aircraft wing rarely matches the surface characteristics of the test wings used during the conceptual design phase and certification process.

This disconnect is usually deemed negligible or overlooked entirely. Specifically, many aircraft incorporate a leading edge slat; however, the mating between the slat and the top surface of the wing is not perfectly flush and creates a small aft-facing step behind the slat. In some cases, the slat can create a step as large as one millimeter tall, which is entirely submerged within the boundary layer. This abrupt change in geometry creates a span-wise vortex behind the step and, in transonic flow, causes a shock to form near the leading edge. This study computationally investigated the implications of an aft-facing slat-step on an aircraft wing and was compared to the ideal wing surface for transonic flow conditions. The results of this study are useful for design of flow control modifications for aircraft currently in service and important for improving the next generation of aircraft wings.

5.5.1 Experimental Methods

This simulation was designed to compare the results of an airfoil with a backward-facing step geometry modeling the presence of a retracted slat-step feature. The RAE 2822 airfoil was chosen for this simulation because there were detailed experimental and computational results already available for it, and it had similar characteristics to the Boeing 757-500 airfoil cross-sections as shown in Figure 5.20. The experimental results were obtained by Cook et. al. and the computational test specifications are listed in Table 5.11. Three airfoil variants were simulated, a clean configuration, and two with a small-scaled backward-facing step, which was scaled with chord length in reference to the 737-500. The computational Grid for this simulation was built with the pointwise software previously discussed in Section 5.1.3. A structured grid was chosen to more easily refine the region near the backward-facing step. A "C" and "H" type grid design was implemented with a far-field domain size of at least fifty chord lengths in each direction, as shown in 5.21. Domain specifications are given in Table 5.12. Three grid refinement levels were produced resulting in a range of five

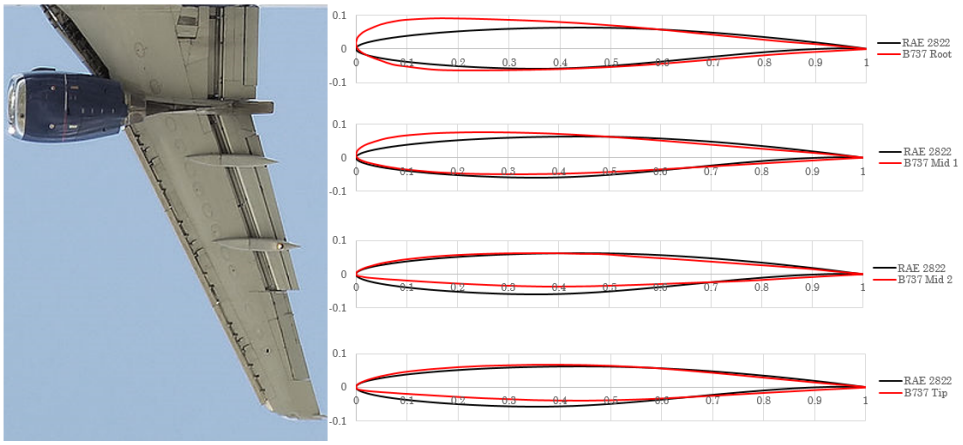

Figure 5.20: Comparison between 737 airfoil sections and the RAE airfoil [106]

Parameter	Value	Unit
H	$\sim$ 0.29-0.60	mm
C	~ 1.0	m
X	$\sim$ 0.114-0.208	mm
ρ	~ 1.17	kg/m^3
μ	$\sim 4.56 \times 10^{-5}$	$Pa\text{-}s$
ν	$\sim 3.87 \times 10^{-5}$	m^2/s
T	~ 300	K
U	~ 252	m/s
Re_H	$\sim 1,875$-$3,900$	
Re_C	$\sim 6.5 \times 10^6$	
$Mach$	~ 0.725	

Table 5.11: RAE 2822 simulation flow properties (all properties which are a function of x-distance are given at the step location)

hundred thousand to five million cells. The specific grid design specifications are listed in Table 5.13. The RANS SST K-Omega turbulence model, previously discussed in Section 3.6, was used and the specific models applied are listed in Table 5.14. These simulations were computed with the OSU Cowboy cluster (metioned previously in section 5.1.1, and the computational resource specifications are provided in Table 5.15.

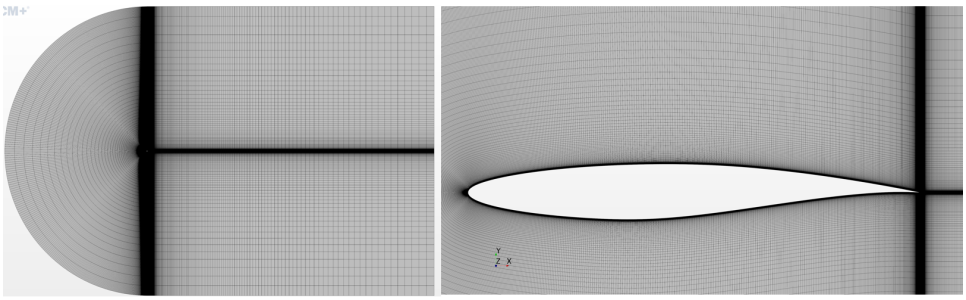

Figure 5.21: RAE 2822 airfoil simulation computational flow domain with structured "C" and "H" type grid.

Dimension	Length	Unit	(-) Boundary Condition	(+) Boundary Conditon
x-distance	~ 60	cm	freestream	freestream
y-distance	~ 2.8	cm	freestream	freestream
z-distance	~ 12	cm	2D	2D

Table 5.12: RAE 2822 simulation domain specifications

Parameter	Value or Description	Unit
Mesh or Grid Type	structured	
Total Cell Count	~ 0.5 to 5.0×10^6	cells
Nodes	$\sim 1,425 \times 400$ to $5,100 \times 1,000$	
Δy (first wall-normal cell)	~ 1	y^+

Table 5.13: RAE 2822 simulation grid specifications

Parameter	Value or Description
Space	two-dimensional
Spatial Discretization	finite volume
Spatial Discretization Scheme	2^{nd}-order upwind
Time	steady
Flow	coupled
Equation of State	ideal gas
Viscous Regime	turbulent
Turbulence Model	RANS SST K-Omega
Wall Treatment	all y^+ wall treatment
Linear System Iterative Method	bi-conjugate gradient stabilized method

Table 5.14: RAE 2822 simulation specifications

Item	Value or Description
Number of Cores	24-48
Average Time per Iteration	2.2-24 s
Total Physical Time	2-13 hr
Total CPU Hours	30-665 hr

Table 5.15: RAE 2822 simulation computational resource specifications

5.5.2 Results and Discussion

The results of these simulations were found to be nearly grid independent, with very little variation between grid refinements. However, the shock location was clearly under predicted, as shown in Figure 5.22. This resulted in less than 1 percent error compared to the lift and drag experimental results. This error in the simulation is likely due to the turbulent trip added to the airfoil at the three percent chord location during experimental testing. An artificial leading edge turbulent trip could be applied to the airfoil to explore this possibility. Despite the slight error in shock location with respect to the experimental results, the three simulated geometries were compared to each other in an attempt to identify the differences between them. All three were surprisingly consistent with each other; however, at the locations of the backward-facing step, a sharp pressure coefficient spike was produced, as shown in Figure 5.23. The effect of the backward-facing step may also be seen in the scaler Mach images, as shown in Figure 5.24. These results suggested that the presence of an extremely small backward-facing step could drastically affect the flow field in the transonic flight regime. Additionally, the drag results for three geometries were compared and showed a nearly identical five percent increase in pressure drag, one percent decrease in shear drag for a net drag increase of nearly three percent for the airfoils with backward-facing steps. These results need to be further refined prior to making any conclusions, but it does appear that the small scale backward-facing steps could have a significant negative effect on the performance of airfoil. Future work should compare turbulence models, grid design, and results with other published

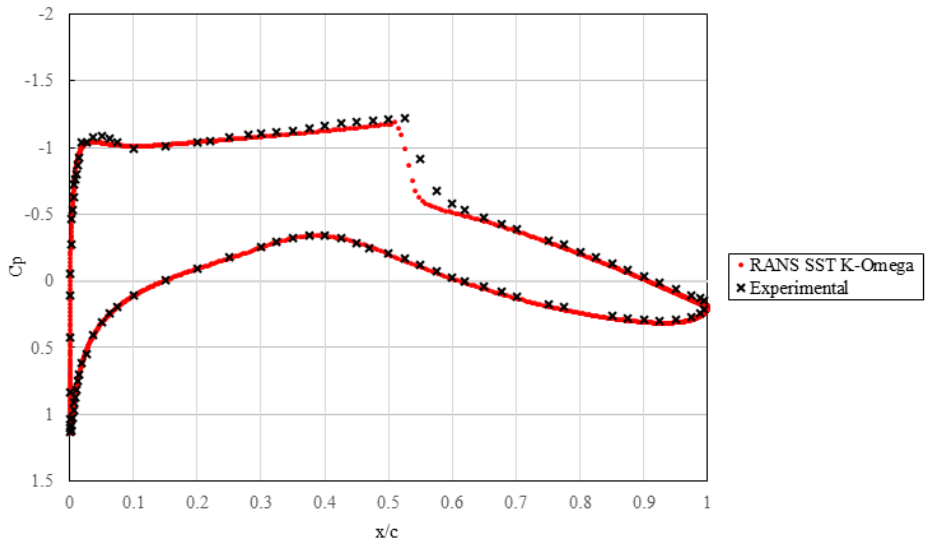

Figure 5.22: Comparison of smooth RAE 2822 airfoil simulation results to experimental results [107].

CFD simulations for this airfoil at these conditions to improve the clean geometry case and then apply those modifications to the backward-facing step cases.

5.6 Flight Scale Wall Shear Pattern Reproducing Simulation

The goal of this simulation was to attempt solving the flow around the unscaled, or subsonic flight scale CVG device. This approach was computationally intensive and, when this route was originally started, it was unclear if it would even be possible to simulate the flow at this scale. Because no quantitative experimental CVG data existed for these conditions, the validation of the simulation was based on qualitative wall shear stress patterns produced during subsonic flight tests and known law-of-the-wall velocity profiles for turbulent boundary layers. A list of the flow properties are given below, which were taken from the range of subsonic flight test flow properties provided by Edge Aerodynamix's flight test results. The computational approach of this simulation was modified and built upon iteratively with each new set of results, and three distinct phases have been completed for this simulation thus far.

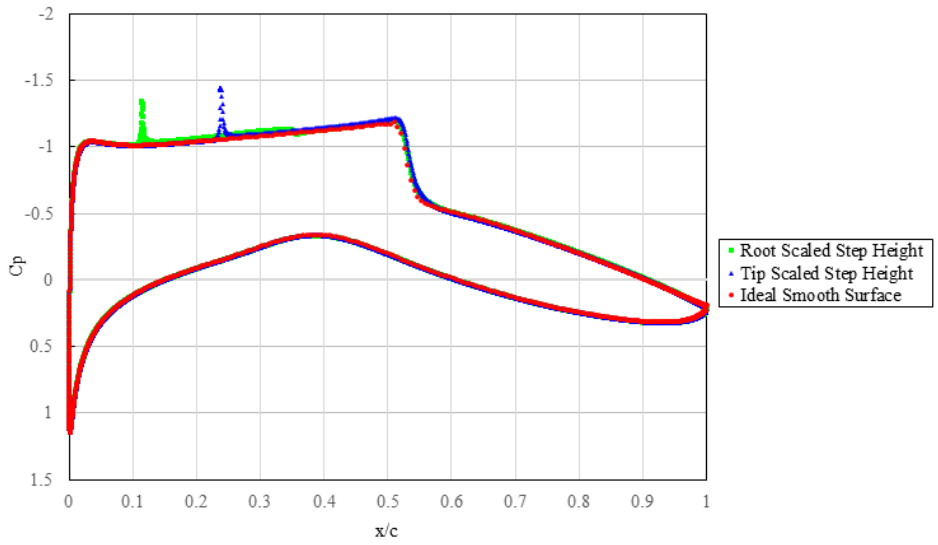

Figure 5.23: Comparison of RAE 2822 simulation results for the backward-facing step airfoil to experimental results for the ideal smooth airfoil [107].

5.6.1 Experimental Methods

Initially, this simulation began with a two CVG width domain, and the Star-CCM+ automated unstructured trimmer mesh. The domain was defined with an inlet boundary condition upstream (negative x-direction), a slip-wall on the top-wall (positive y-direction), a pressure outlet boundary downstream (positive y-direction), no-slip-wall boundary with the CVG geometry on the bottom wall (negative y-direction), and periodic boundary conditions on both the negative and positive z-direction boundaries, as shown in Figure 5.25. Periodic boundaries allowed the simulated domain to be drastically smaller without forcing a channel flow phenomena. The domain geometry specifications are provided in Table 5.17. A slip-wall constraint was applied to the top-wall because initial attempts with a freestream condition produced an unstable solution that did not converge. The slip-wall boundary was used to mitigate the instability with the freestream condition, but was not the ideal boundary condition. At the inlet, a constant velocity boundary condition was applied. The mesh was designed based on the wall unit specification of the flow, and prisms were erected to encompass the boundary layer. Mesh specification are provided in Table 5.18 and Figure

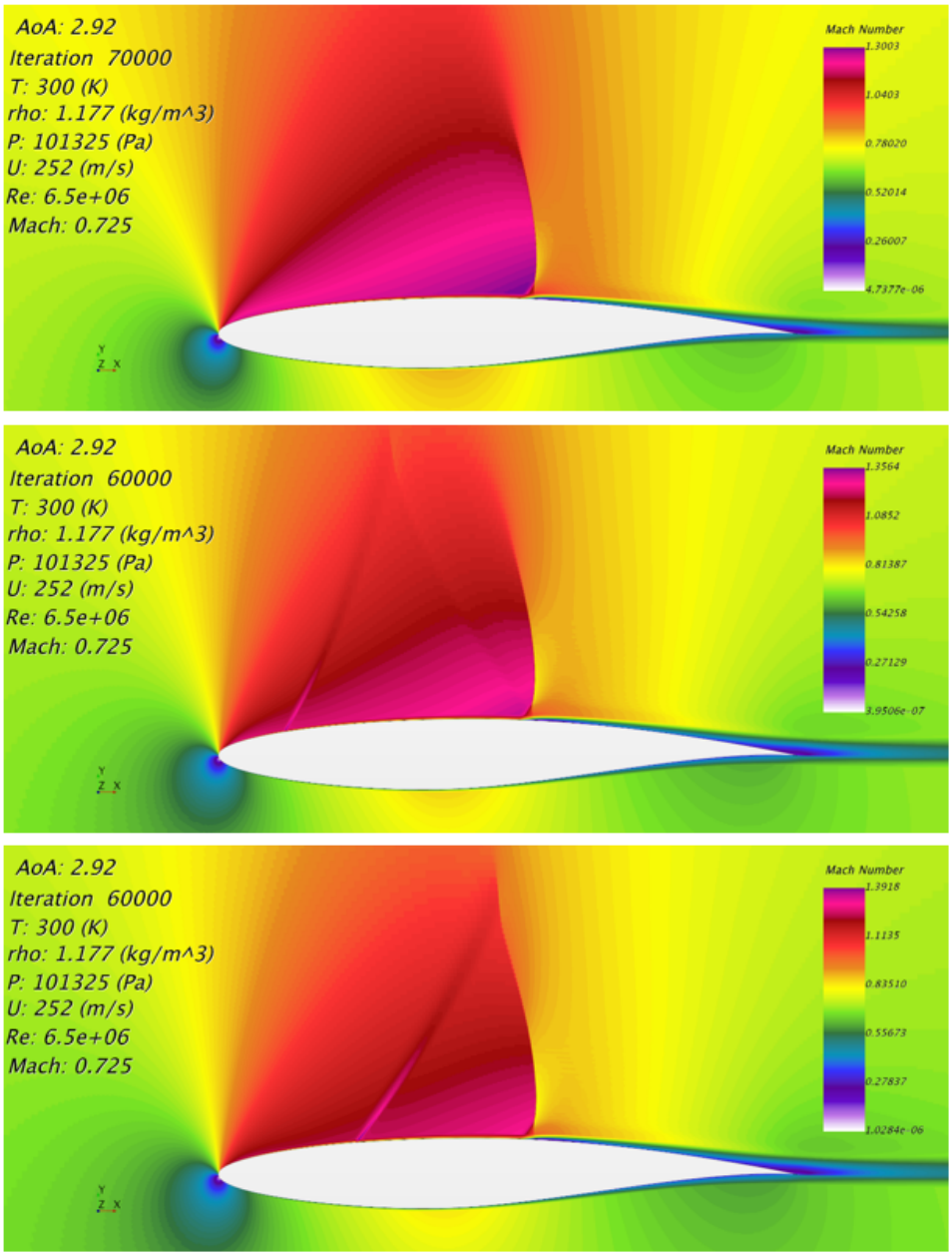

Figure 5.24: Mach profiles: top is smooth airfoil, middle is root-percent chord backward-facing step airfoil, and bottom is tip-percent chord backward-facing step airfoil.

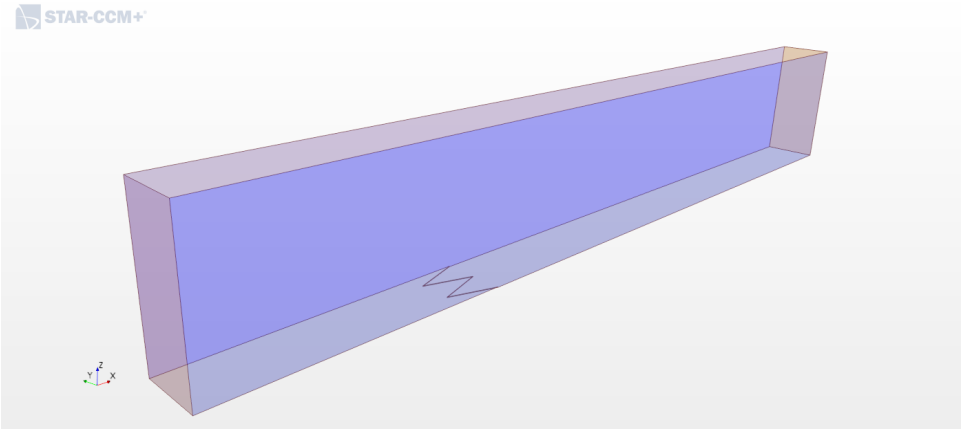

Figure 5.25: Phase 1 computational flow domain.

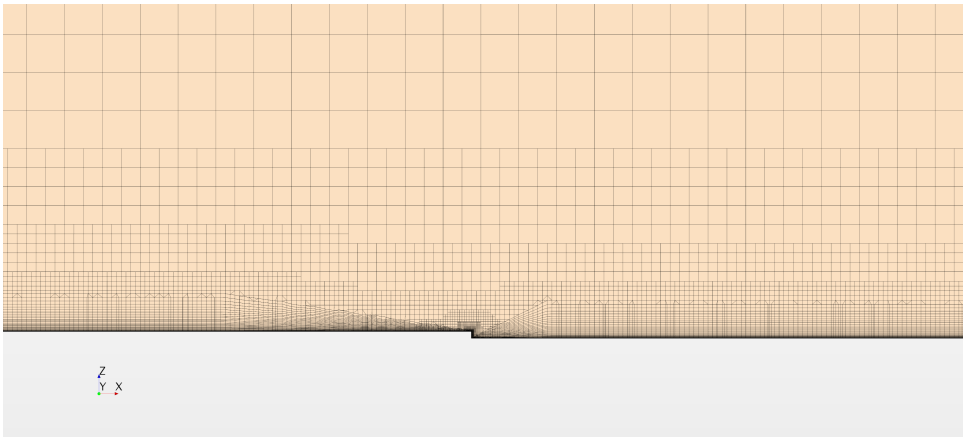

Figure 5.26: Phase 1 unstructured mesh.

5.26 shows the meshed domain. A DES turbulence model was selected in order to reduce total cell count and, ultimately, simulation solve time. The DES model used a blending function to allow the large scale motions to be resolved with an LES model, and the small scale motions, which were defined based on the scale of the motion relative to the local grid size, were modeled with the RANS formulation as described in Seaction 3.6.

The results of the phase one simulation did not produce the expected wall shear patterns (see Figure 5.27); therefore, the simulation was deemed incorrect and additional results were not collected or considered. Instead, the next revision was developed. Phase two was designed with the assumption that the mesh was not refined enough to resolve enough of the small scale motions to produce the expected wall

Parameter	Value	Unit
H	~ 0.367	mm
L	~ 44.5	mm
W	~ 28.0	mm
X	~ 49.2	mm
δ_{99}	~ 0.554	mm
θ	~ 0.075	mm
δ^*	~ 0.193	mm
y^+	~ 0.0053	mm
H/y^+	~ 69.3	mm
H/δ^*	~ 1.90	mm
H/θ	~ 4.92	mm
H/δ_{99}	~ 0.66	mm
ρ	~ 1.17	kg/m^3
μ	$\sim 1.77 \times 10^{-5}$	$Pa\text{-}s$
ν	$\sim 1.51 \times 10^{-5}$	m^2/s
T	~ 285.2	K
U	~ 60	m/s
Re_{τ_w}	~ 51	
Re_θ	~ 296	
Re_H	$\sim 1,454$	
Re_X	$\sim 1.95 \times 10^5$	
$Mach$	~ 0.17	

Table 5.16: Phase 1, 2, and 3 simulation flow properties (all properties which are a function of x-distance are given at the step location).

Dimension	Length	Unit	(-) Boundary Condition	(+) Boundary Conditon
x-distance	~ 60	cm	velocity inlet	pressure outlet
y-distance	~ 5.6 to 2.8	cm	no-slip-wall	slip-wall
z-distance	~ 12	cm	periodic	periodic

Table 5.17: Phase 1, 2, and 3 simulation domain specifications.

Parameter	Value or Description	Unit
Mesh or Grid Type	unstructured trimmer	
Total Cell Count	$\sim 18 \times 10^6$	cells
Δy (first wall-normal cell)	~ 1	y^+
Wall-Normal Growth Rate	~ 1.2	

Table 5.18: Phase 1 (DES) simulation grid specifications.

Parameter	Value or Description
Space	three-dimensional
Spatial Discretization	finite volume
Spatial Discretization Scheme	2^{nd}-order hybrid bounded-central-differencing
Time	implicit unsteady
Temporal Discretization Scheme	2^{nd}-order backward differentiation
Flow	coupled
Equation of State	ideal gas
Viscous Regime	turbulent
Turbulence Model	IDDES
Subgrid Scale Model	RANS SST K-Omegal
DES Wall Treatment	low y^+ wall treatment
Linear System Iterative Method	bi-conjugate gradient stabilized method
Iterations per Time-step	10

Table 5.19: Phase 1 (DES) simulation specifications.

Item	Value or Description
Number of Cores	540
Average Time per Iteration	4.9 s
Total Physical Time	366 hr
Total CPU Hours	171,700 hr

Table 5.20: Phase 2 (DES) simulation computational resource specifications.

Figure 5.27: Wall shear patterns are not properly simulated in phase 1.

Figure 5.28: Comparison of phase 2 refined mesh with half sized and orignal sized domain; notice downstream effect.

shear patterns. However, increasing the cell refinement would drastically increase the total cell count and computational time. Therefore, this iteration of the simulation design reduced the total domain width (in the z-direction) by a CVG width. This allowed the mesh to be adequately refined without increasing the total cell count; although, it did limit the effects of span-wise interaction between the domains downstream. This effect may be seen in the results of a comparative study of the effect of halving the domain width with no other simulation differences, as shown in Figure 5.28. Limiting this span-wise interaction is not ideal, but was necessary to further refine and iterate on the simulation design and should be considered once an adequate simulation is produced. The mesh specifications for phase two are given in Table 5.21, and Figure 5.29 shows the meshed domain. The domain boundary conditions 5.17, Turbulence model 5.19, and simulation properties 5.16 were not modified between phase one and phase two.

Parameter	Value or Description	Unit
Mesh or Grid Type	unstructured trimmer	
Total Cell Count	$\sim 30 \times 10^6$	cells
Δy (first wall-normal cell)	~ 1	y^+
Wall-Normal Growth Rate	constant for 0.15 mm then ~ 1.2	

Table 5.21: Phase 2 (DES) simulation grid specifications

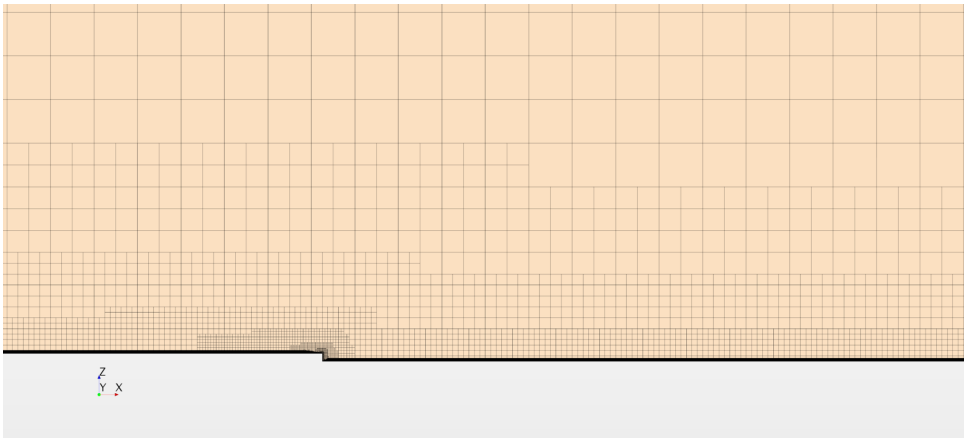

Figure 5.29: Phase 2 refined unstructured mesh.

The results of phase two produced wall shear patterns similar to those seen in flight, but not identical, as shown in 5.28. This seemed to support the idea that the mesh was not adequately refined to properly resolve the dominate behavior of the flow. However, further investigation revealed that in order to produce the expected wall shear patterns, the mesh had to be refined to a point which defeated the purpose of using the DES model all together. Figure 5.30 shows a comparison of the DES blending function between the phase one and phase two simulation results, which clearly indicated that the DES simulation was forcing an LES model solution in the near-wall region of the flow for phase two. These results suggesed that the DES method was not capable of modeling the flow around the CVG, because the RANS equations were not flow resolving, and as such, could not appropriately resolve the small scale motions which produce the unique wall shear patterns seen in flight. This finding was significant because it pointed to the scale of the CVGs flow interaction and all but completely ruled out the use of RANS type models near the CVG geometry. From the results of phase two, it was obvious that future revisions of this simulation would require eddy resolving turbulence models. The shear results produced by the phase two simulation were not sufficiently similar to the wall shear stress patterns seen from flight tests, and because of this, the results were not evaluated in depth. Instead, the next phase of the simulation was developed.

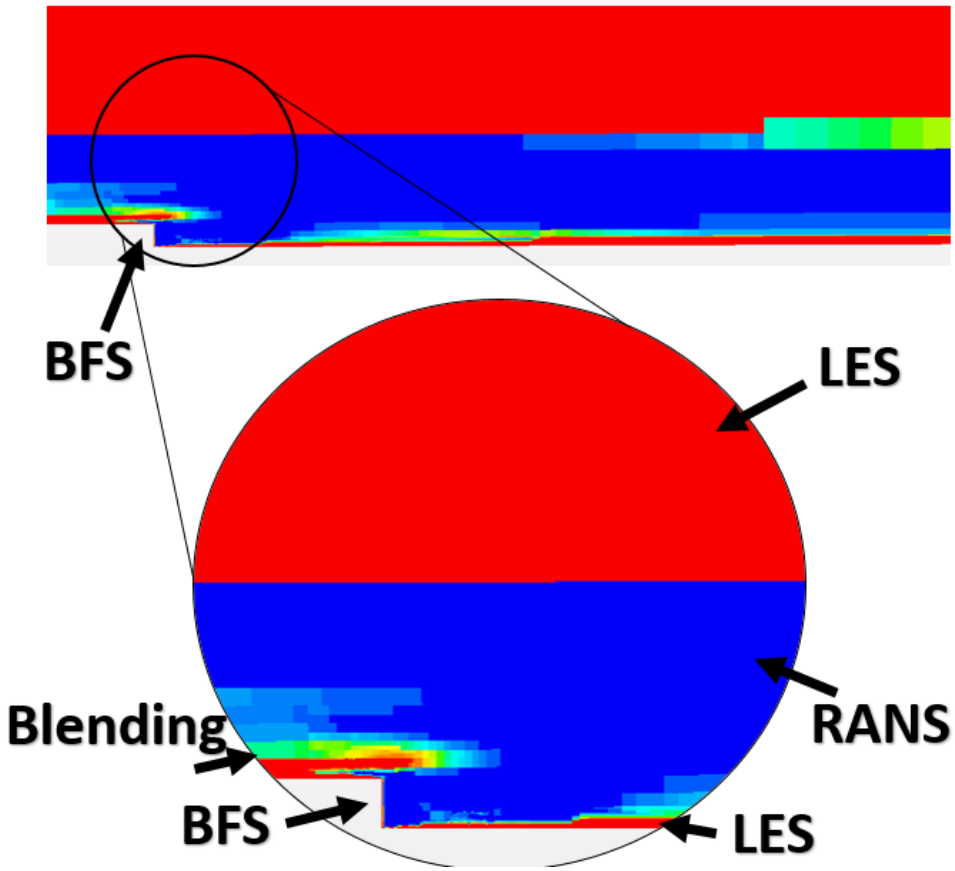

Figure 5.30: Phase 2 IDDES solution blending (Red is LES, Blue is RANS, and in between is blended). The far field should be LES and near the wall should be RANS for proper IDDES configuration.

Phase three of this simulation sought to resolve most of the near wall turbulent kinetic energy production and fall into the category of a near wall resolving LES (NWR-LES) simulation, as defined by Pope (2015) [87]. The dynamic Smagorisky sub-grid scale model (as discussed in Section 3.7) was used in accordance with this objective, where the LES simulations filter range was dependent on cell size, so that if the cells were adequately small, the simulation would default to a DNS type solution [87]. Although, it should be noted that the discretization schemes implemented (spatial and temporal as discussed listed in Table 5.22) were only second-order accurate, and not of higher-order accuracy as those which are commonly implemented with DNS methods. The mesh from phase two was completely disregarded, and a new structured grid was designed using the Pointwise software discussed in Section 5.1.3. A structured hexahedral grid was chosen because it allowed more control in the grid design, enabling each cell size to be defined in the x, y, and z-directions. However, the added control came at the cost of hand crafting the entire grid, which was far more intensive than using the automated unstructured meshes. The goal was to keep the same domain size, so that the results would be comparable to the previous phases, and at the same time, keep the total cell count below 100 million cells in order to limit computational time. Grid specifications were developed around the upper limits of Tucker's recommended cell sizes for wall resolving LES models, as shown in 5.31. The upper limit values were selected as a first attempt in order to minimize the total cell count. An additional complication of implementing the structure grid was producing the triangular grid topology around the CVG, which was difficult using structured hexagonal cell elements. This was overcome by creating a specialized topology which broke the three-sided triangular surfaces into three smaller four-sided geometries. Cell skewness was a serious issue initially, but adjusting the cell distribution mitigated the effect, as shown in Figure 5.32. The turbulence model and grid design specifications are given in Table 5.22 and 5.23 respectively.

Parameter	Value or Description
Space	three-dimensional
Spatial Discretization	finite volume
Spatial Discretization Scheme	2^{nd}-order bounded-central-differencing
Time	implicit unsteady
Temporal Discretization Scheme	2^{nd}-order backward differentiation
Time-Step Control	convective CFL time-step control
Time-Step Control CFL Target Mean	0.5
Time-Step Control CFL Target Max	5.0
Time to Solution Convergence	$\sim 0.01s$
Total Data Collection Time	$\sim 0.007s$
Flow	coupled
Equation of State	ideal gas
Viscous Regime	turbulent
Turbulence Model	LES
Subgrid Scale Model	dynamic Smagorinsky model
LES Wall Treatment	low y^+ wall treatment
SGS Filter Width	2.0
SGS Time Scale Coefficient	3.5
Linear System Iterative Method	bi-conjugate gradient stabilized method
Iterations per Time-step	15

Table 5.22: Phase 3 (LES) simulation specifications.

Parameter	Value or Description	Unit
Mesh or Grid Type	structured	
Total Cell Count	$\sim 75 \times 10^6$	cells
Δx	~ 130	y^+
Δy (first wall-normal cell)	~ 1	y^+
Δz	~ 30	y^+
Wall-Normal Growth Rate	constant for 1mm then ~ 1.2	

Table 5.23: Phase 3 (LES) simulation grid specifications.

Method	$\Delta x^+/\text{Min}(\Delta y^+)/\Delta z^+$
DNS	(10–15)/1/5
Wall resolved LES	(50–130)/1/(15–30)
LES with a wall model	100–600/(30–150)/100–300
Hybrid RANS-LES	(100–600)/1/(100–300)
RANS	1000/1

Figure 5.31: Recommended starting grid sizes for specific simulation types [108].

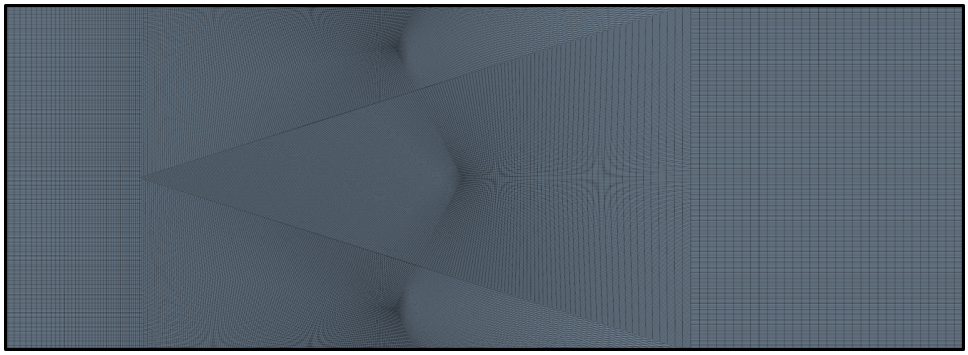

Figure 5.32: Grid topology around CVG geometry produced skewed cells.

5.6.2 Results

The results from phase three produced nearly identical wall shear stress patterns to those seen in Edge Aerodynamix flight testing, as seen in Figure 5.33. These results indicated that the simulated flow over the CVG was at least similar to the flow around the CVG in subsonic flight tests. However, the simulation results were not without error. The second validation criteria for this simulation, the law-of-the-wall velocity profiles, were not in accordance with expected results. Law-of-the-wall profiles for the CVG simulation are provided at three different x-locations; upstream of the CVG shown in Figure 5.34, immediately downstream of the CVG shown in Figure 5.35, and far downstream shown in Figure 5.36. The locations of these profiles are shown on the diagram in Figure 5.37. The profile agreed well with the Blasius solution upstream of the CVG where a laminar boundary layer was expected, but downstream of the

CVG, in the turbulent region, the log-law of the profile was noticeably shifted. This shift was a known defect of the LES simulation filtering operation and was discussed in detail by Denero (2011). The shifted log-law profile can be improved upon by reducing the cell count further, but because the LES equations are ultimately filtered (whether physically or due to numerical filtering as a result of lower-order schemes), it was not possible for the LES model implemented to reliably produce results on the order of accuracy of DNS results in its current configuration [93]. Taking this into consideration, the results of the phase three simulation were not well enough resolved to produce accurate law-of-the-wall profiles; therefore, comparing its results to experimental or DNS data would not be as informative. However, producing another simulation for a backward-facing step simulation with the exact same grid and solution method would give a baseline for comparison. Therefore, a baseline simulation was constructed for a backward-facing step of the same step height and ran to convergence. The backward-facing step variant of the phase three simulation shear results were in agreement with backward-facing step wall shear stress tests performed at the same subsonic flight conditions as shown in Figure 5.38. Log-law region shift was also present in the backward-facing step variant, confirming that the issue relates back to the solution method and not a unique effect produced by the CVG geometry.

5.6.3 Limitations and recommendations

The results from this simulation were limited by a number of factors which are addressed below in order to inform future revisions:

- Ideally the inlet, outlet, and top-wall boundary conditions would be replaced with a freestream boundary condition to eliminate the effect of ducting; however, is it is difficult to define the upstream and downstream boundaries so that the boundary layer developed on the bottom wall is not influenced. Correcting this

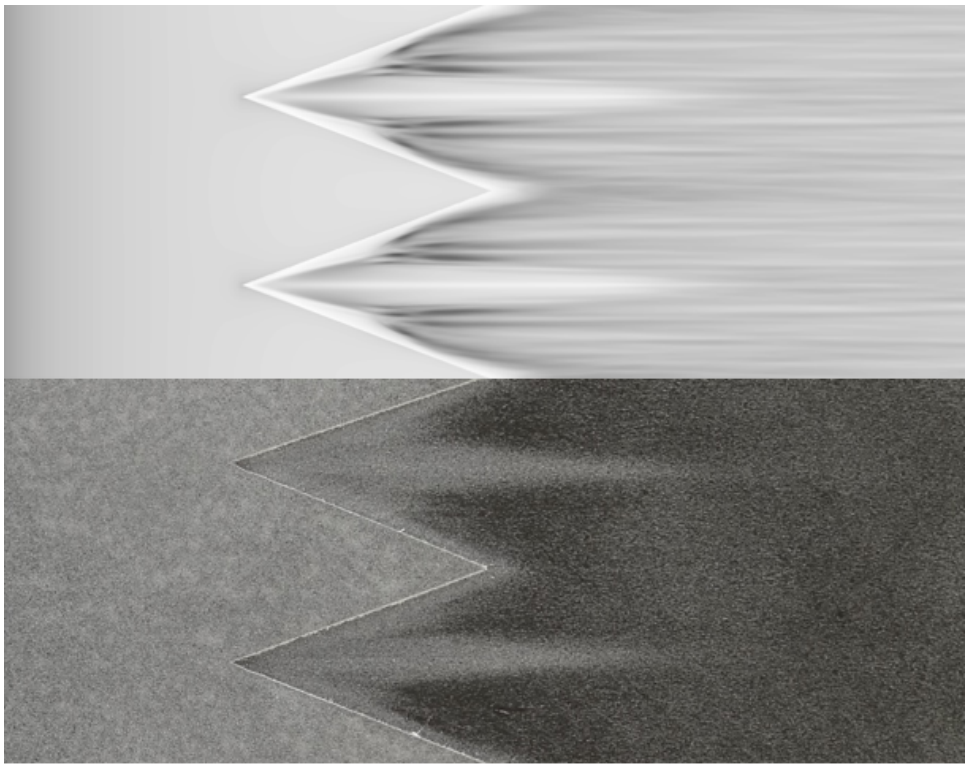

Figure 5.33: CVG wall shear stress patterns agree very well with flight test results (top is simulation result and bottom is flight test result).

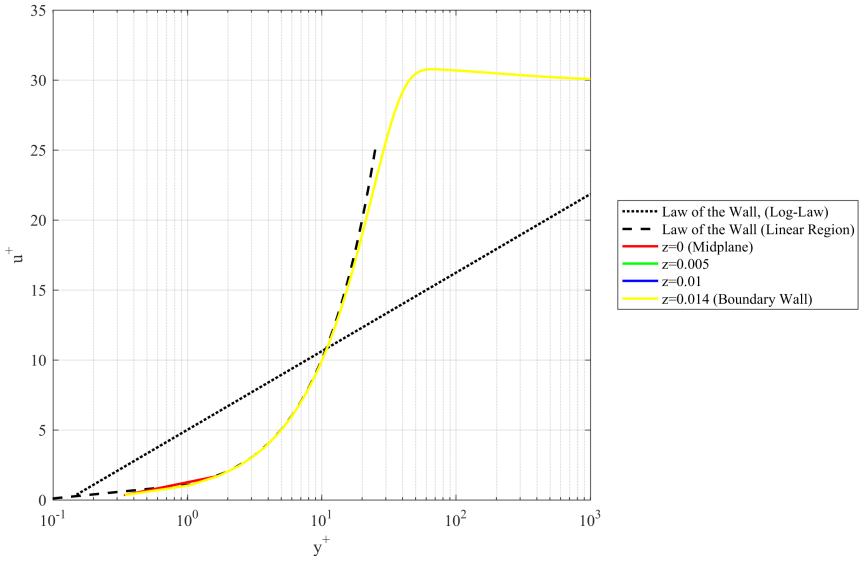

Figure 5.34: law-of-the-wall velocity profile upstream of CVG (x=-0.025 m). The four profiles collapsed to the same profile.

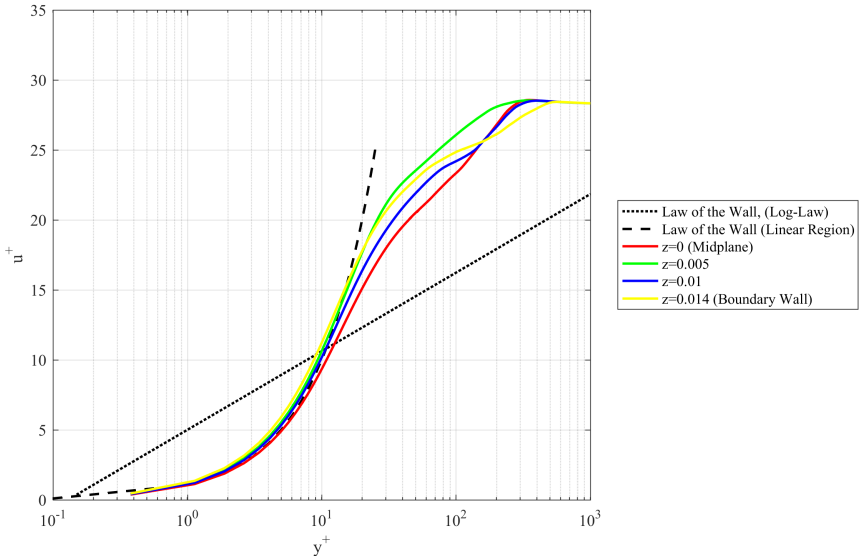

Figure 5.35: law-of-the-wall velocity profile downstream of CVG (x=0.1 m).

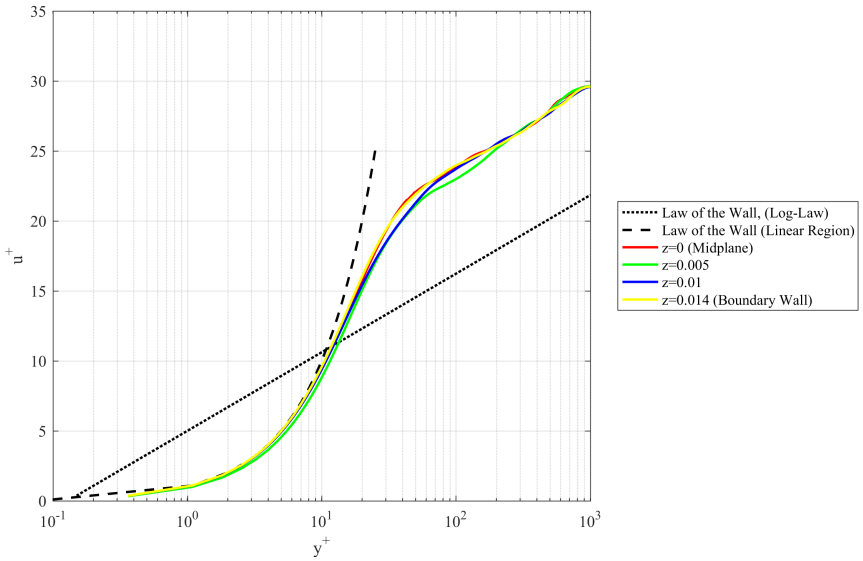

Figure 5.36: law-of-the-wall velocity profile far downstream of CVG (x=0.4 m).

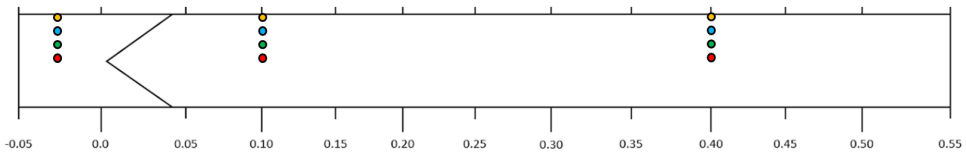

Figure 5.37: Top down view diagram displays the location of law of the wall velocity profiles in meters (red is at the center plane and green, blue, and yellow approach the wall).

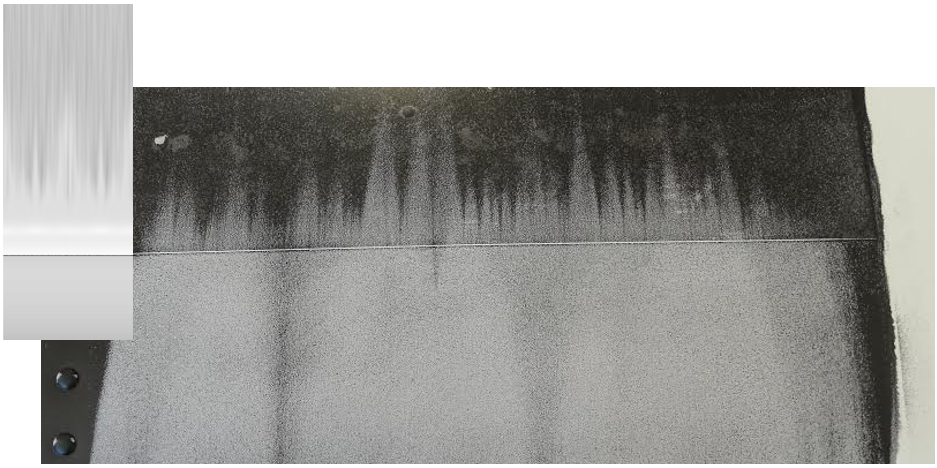

Figure 5.38: Backward-facing step wall shear stress patterns agree very well with flight test results.

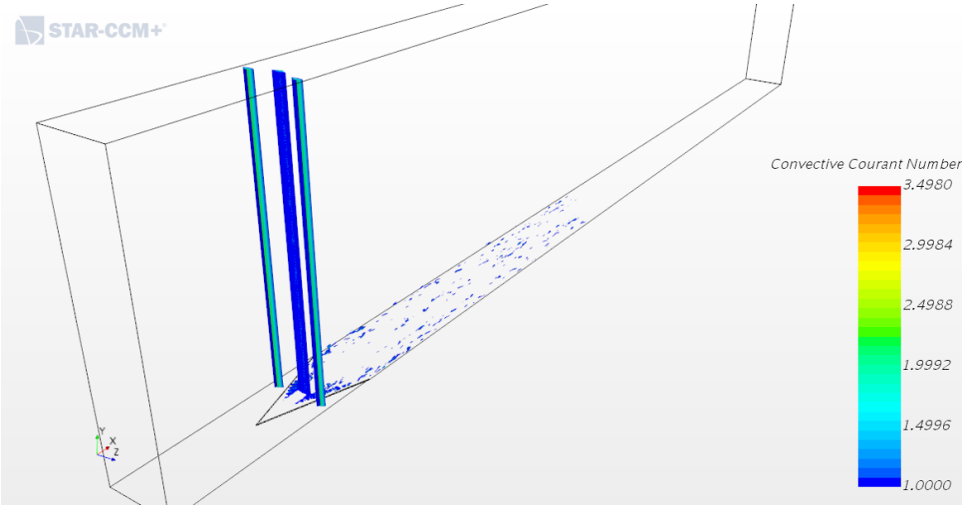

Figure 5.39: Effect of grid topology on CFL through domain.

issue would also allow the domain height to be drastically reduced, which will be necessary for the increased refinement that future simulations will require.

- Pointwise structured grid skewness in the topology around the CVG geometry produced small skewed cells in the far field, where the freestream velocity is relatively large. This ultimately produced higher than ideal convective currant number values in vertical columns through the domain, as shown in Figure 5.39. Ideally, the grid topology should be adjusted to at least mitigate if not entirely resolve this issue.

- The prescribed constant inlet velocity produced a large wall shear stress near the inlet and did not allow proper boundary layer development prior to the CVG geometry. Future simulation should prescribe a boundary layer profile at the upstream inlet that allows the flow to more naturally develop and produce a more reasonable boundary layer at the step.

- The domain length of this simulation was originally chosen for the DES turbulent model, which did not attempt to resolve the smallest scales of motion; therefore, domain length was not a serious consideration. However, with the current direction of the simulation, attempting to be wall resolving, the domain length of 0.6 meters is unreasonable. A shorter domain will more easily be resolved, due to limiting the maximum Reynolds number, but also by reducing the cell count (by as much as 75 percent). The next revision to this simulation will have to balance the domain length from being too long to resolve or too short, which could affect the development of flow around the CVG.

- Computational resources and computational solution time were serious constraints for this simulation and will continue to be so with future iterations. Given the OSU HPPC Cowboy cluster specifications at this time (as discussed in Section 5.1.1), the cell count should be limited to below 100 million with the expectation that the computational resource limit is roughly 540 cores.

- The log-law region shift produced in the phase three simulation must be improved upon by further refining the grid. However, as the grid refinement increases, the required time-step reduces and, ultimately, results in a nonlinear increase in computation time. Therefore, it would be valuble to perform a grid refinement study based on the results of Denaro (2011) [93] in order to evaluate the capability of the Star-CCM+ LES SGS models prior to applying them to the computationally intense flight scale CGG simulation.

5.6.4 Conclusion

This simulation is an ongoing project which will require more revisions and improvements in order to reach an adequate solution. However, the phase three results do seem to suggest that the flow structure around the CVG could be appropriately simulated, as indicated by the remarkable similarity between flight test wall shear stress patterns and those produced in the simulation. This finding is significant because, up until this point, there have been no indications that computational methods could reproduce the flow structure produced in flight, which limited the ability to study the CVG device. Although the results presented here do have a known law-of-the-wall velocity profile error, it is a product of the LES filter function and ultimately an artificial turbulent viscosity value. Therefore, the results of this simulation are not conclusive and should be built upon using the previously discussed limitations and recommendations to further improve its viability.

5.7 Additional CFD Projects in Development

In addition to the previously discussed computational experiments conducted, there are other CFD projects currently in development which all support the goals of the research effort. These projects were still in the early stages at the time of this document's conception, but brief descriptions of each with insight into their preliminary findings are provided.

5.7.1 2D Backward-Facing Step Grid Study and Verification

A well-known CFD verification study consolidated by the NASA Langley Research Center, Turbulence Modeling Resource, of the traditional backward-facing step has produced many model turbulence model results and continues to be built upon. This body of research data provides an ideal comparison for our mesh or grid design methods and computational models for a flow regime very similar to the CVG, which

does produce a small scale swept backward-facing step. The experimental results are provided from Driver and Seegmiller (1985) [105] and have been reproduced computationally with multiple turbulence models. Preliminary results using the Star-CCM+ implementation of the RANS SST-K-Omega turbulence model with provided structured grids have produced comparable results for other researchers.

5.7.2 NACA 65-415 Airfoil Simulation

The subsonic flight test platform, which is the basis for the majority of the research conducted at OSU, is the "Arrow" variant of the Piper Cherokee. Understanding the specific flow characteristics at the location of the CVG would improve scaling capabilities and verify the assumed flow properties currently used. Therefore, a subsonic simulation around the Piper Cherokee NACA 65-415 airfoil is currently in development. If a properly validated simulation design can be produced, using Abbott and Doenhoff (1959) [1] data as the validation technique, then accurate boundary layer specifications and pressure gradient data can be extracted from the simulation and used in flat plate experimental tests and high-fidelity CVG simulations.

5.7.3 Water Tunnel Data Validation Exercises

The ultimate goal of the CFD effort is to obtain a validated simulation of the properly scaled CVG geometry from water tunnel experimental results. This would allow the flow field around the CVG to be thoroughly evaluated with high definition visual representations and a near infinite amount of data. However, this hinges on the ability to properly reproduce an experimental flow. This has been accomplished to some extent in other CFD simulations presented here, but not using quantitative experimental results obtained from PIV measurements. This is the missing link between the experimental and computation research efforts. Therefore, this project takes generic wall boundary layer PIV data from the medium water tunnel at some upstream location

and sets it as the inlet condition of the simulation. Then, the results of the simulation are compared at some downstream location with additional PIV data taken at the same downstream distance. The scope of this project includes evaluating differences between 2D and 3D simulations, mesh or grid designs, and various turbulence models. This project is critical to the appropriate validation of the required future CFD simulations needed to properly evaluate the flow around the CVG geometry.

Chapter 6

Conclusions

The Conformal Vortex Generator technology was investigated through experimental and computational means. These tests were not limited to the CVG device themselves, but also encompassed the flow fields in which the CVG operate. This Chapter will restate the work presented and the conclusions drawn.

6.1 Summary

Edge Aerodynamix's CVG is a new drag reduction technology, which is currently available for the Boeing 737 transport category aircraft and the Robinson 22 helicopter. These applications are inherently different, and this work focused on the Boeing 737 application. However, the Boeing 737 operated in a transonic flight regime and extremely large Reynolds numbers, which restricted test capabilities. Edge Aerodynamix had carried out fuel burn experiments on the full scale platform, which compared the fuel consumption with and without the CVG technology applied and had also observed shock behavior differences between two cases. Fuel consumption tests indicated improved fuel efficiency as high as 6 percent under typical operating conditions, which was the motivation behind characterizing the CVG technology. Subsonic flight tests indicated that unique flow patterns, seen as low-shear diamonds, were generated near the CVG with lasting effects that produced organized shear behavior, seen as long low-shear streaks, throughout most of the favorable pressure gradient region. These wall shear stress results were the direct focus of this investigation which endeavored to characterize the laminar to turbulent transition in the subsonic

flight regime, which could then be indirectly applied to the transonic flight regime for future transonic investigations. The transonic shock behavior indicated that the CVG device stabilized an otherwise transient shock feature, which oscillated in the chord-wise direction. This stabilization of the shockwave was significant and could be the source of the largest drag reduction effect. However, without adequate transonic experimental facilities this mechanism cannot be directly evaluated. Therefore, this investigation focused on subsonic wall shear stress flight tests conducted by Edge Aerodynamix.

6.1.1 Research Findings

Experimental results were reported for initial low-speed wind tunnel flow visualizations, which indicated that the CVG are sensitive to inlet flow conditions and that visualization of the flow around the CVG device would require an appropriate scaling for a more consistent comparison. These results led to medium-sized water tunnel flow visualization tests using colored dye injection of the Reynolds number based on downstream distance scaling with the high-speed phantom cameras. The dye tests found that the flow seemed to follow the inner-wall of the CVG device, despite the flow direction and speed of the mean-flow. These findings were consistent with wall shear stress flight results and indicated that the flow at the upstream apex of the CVG is pulled into the device and along the inner-wall, relocating that fluid to the downstream apex. These results were limited by the small size of the CVG, dye pressure sensitivity, and dye injection location. Therefore, PIV testing of the flow field was performed to better understand the larger flow field around the CVG device. However, the results from the PIV tests were not adequately resolved for the small size of the step and emphasized the need for an appropriate scale that would allow for better resolution of the geometry or the ability to resolve smaller geometries with the PIV system. Additionally, an early attempt at CFD modeling was made to evaluate the

flow around the CVG geometry. The results of this crude RANS k-omega simulation were consistent with dye test results, indicating that flow is dispersed from the middle section of the CVG immediately after the upstream apex, but the wall shear stress results from the simulations were in conflict with the flight test shear stress results, which was most likely due to poor resolution around the CVG devices. Therefore, the outcomes of the dye flow visualization, PIV flow field tests, and the CFD simulation resulted in multiple investigative paths. The PIV methods were improved to allow enhanced zooming; a larger scale geometry scaling was explored, and computational methods were improved upon. Additionally, the three-sided approach was adopted for future tests which attempted to design scaling that can be tested through visual, PIV, and CFD methods.

A CFD study of the high-speed SOKO Test platform was conducted in order to improve CFD skills, and provide valuable flow properties, namely local boundary layer thicknesses and pressure gradients for future scaling work. These results were mixed, but proved accurate for moderate angles of attack, which would be the subject of reasonable scaling approaches. This work built confidence in the value of adding computational methods to the research program and provided additional 2D airfoil data for future scaling work. The larger scale geometry, developed from the Reynolds number based on step-height-based Reynolds number scaling, was explored with dye testing, PIV, and CFD methods. The dye injection tests found that this scaling of the CVG behaved similarly to a backward-facing step of the same scale. PIV results, though limited to non-time-resolved data, were in agreement with the dye testing. The CVG simulation work provided more insight about the unsteady nature of the flow, indicating that the larger scale CVG seemed to organize the shedding behavior by shedding hairpin structures aligned with the CVG geometry. From these enlarged CVG tests, it was determined that the CVG device is sensitive to apex ratio, which is the CVG triangular height "L" to the step height "H", and as this ratio

approaches 1 the step behaves more like a backward-facing step. Additionally, the indication of organized shedding of hairpin structures suggests that the CVG device may be capable of organizing coherent structures. However, these results were not adequately evaluated, because other scaling options were pursued after determining that the enlarged CVG geometry was behaving similarly to a traditional backward-facing step.

The results of the enlarged CVG led to the creation of two new scaling approaches, which related the step height to the structure of the boundary layer. These approaches were applied to airfoil test sections in order to account for relative pressure gradient conditions. The two scaling options were based on the boundary layer momentum thickness and the wall unit parameter. Detailed dye flow visualization tests indicated that the two scales were inherently different, producing drastically different results. The study was limited by wing section chord, tunnel velocity, and inconsistencies between tests. The conclusions drawn from these scalings indicated that CVG geometrical triangle length "L" and width "W" must be considered together in future scaling approaches and that attempting to reproduce relative pressure gradients with wing sections is not practical for the medium-sized water tunnel. Therefore, an adequate scaling, which could be applied to a traditional flat plate test section and accounted for step height, boundary layer thickness, pressure gradient, and geometry of the CVG triangles, was required. In addition to these experimental tests, two CFD simulations were pursued. The first focused on the transonic effects of the slat-step seen on the Boeing 737 platform. This simulation reproduced the airflow over a 2D RAE 2288 airfoil and investigated the effect of a scaled slat-step placed along the chord similar to the Boeing 737. The results indicated that the slat-step could produce additional shock features on the wing surface, and therefore, increasing pressure wake drag. However, this simulation work is ongoing and continues to develop. The second simulation sought to reproduce the flow around a simplified CVG geometry

on a flat plate at the subsonic flight conditions similar to those encountered by Edge Aerodynamix's subsonic test platform. The scale of this simulation was drastically reduced to enable the use of semi-flow resolving turbulence models, initially DES and then LES. The results of this simulation showed that wall shear patterns, nearly identical to those produced during Edge Aerodynamix's flight tests, can be reproduced with CFD simulation. This was significant because it was the first formal reproduction of any result that could be directly compared to the actual flight test results produced by Edge Aerodynamix, and it suggests that, for a simplified case, the flow around the CVG could be adequately resolved and simulated. The results of this study were influenced by the LES simulation dynamic Smagorinsky SGS model turbulent viscosity and are still in question; however, the wall shear patterns are an indication of, at least, similar flow structure to that of the flight tests. This simulation is an ongoing project and will continue to be revised and further developed to mitigate the effects of the SGS turbulent viscosity and increase the confidence in the results obtained.

Additional CFD studies have been in undertaken, including a backward-facing step grid evaluation, the subsonic flight test airfoil simulation, and water tunnel validation preparation simulations. The backward-facing step study focuses on evaluating the effects of mesh types on solution accuracy and will be crucial to the proper selection of grid and mesh designs moving forward. The subsonic flight test platform airfoil simulation pursues accurate flow properties around the airfoil that will provide useful information concerning the boundary layer and pressure gradient at the CVG location. The water tunnel validation simulations are necessary to develop the experience needed to take future PIV results and apply them to simulation work, which will then attempt to reproduce PIV results in other areas of the flow. Figure 6.1 illustrates the research direction since the program's inception in the Fall of 2015.

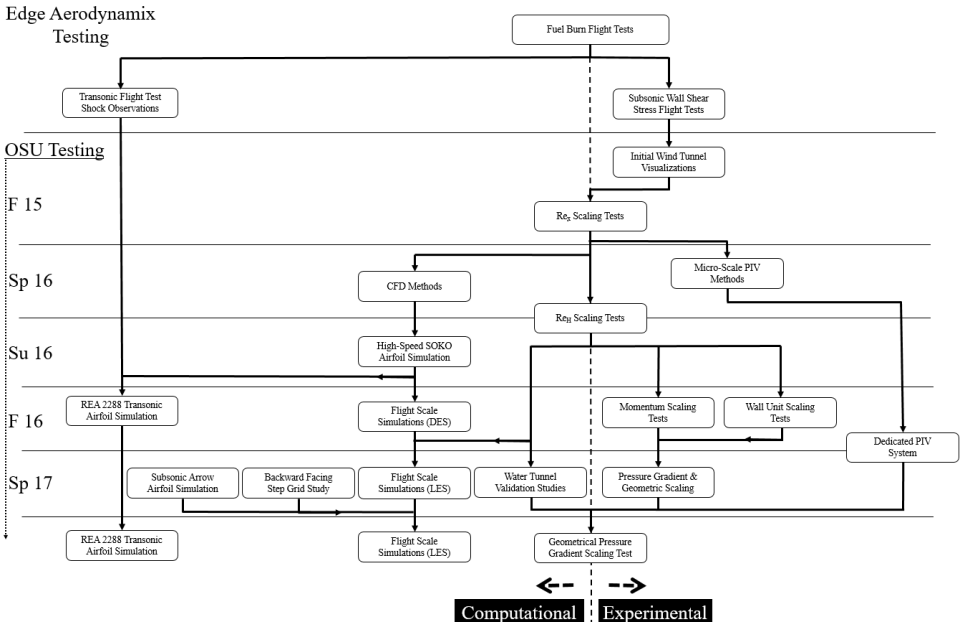

Figure 6.1: Illustration of research direction from Edge Aerodynamix test results into testing at Oklahoma State University.

6.1.2 Overall Conclusions

Products of Preexisting Edge Aerodynamix Flight Test Results:

- The application of the CVG device to the Boeing 737 noticeably increases fuel efficiency in cruise conditions, based on fuel burn comparative flight tests performed by Edge Aerodynamix (discussed in Section 4.1.2).

- The CVG appears to have an effect on transonic shock stability, based on the shockwave observations performed by Edge Aerodynamix (discussed in Section 4.1.2).

- The CVG device interacts with the flow and produces unique shear stress patterns in the form of low-shear diamonds between CVG apexes and thin low-shear streaks that persist over a large portion of the favorable pressure gradient section of the wing in subsonic conditions, based on subsonic wall shear stress visualization flight testing performed by Edge Aerodynamix (discussed in Section 4.1.3).

Products of Oklahoma State University Investigations:

- The CVG device is sensitive to aspect ratio (geometrical triangular length "L" to step height"H") and resembles flow over a traditional backward-facing step as this approaches 1 (or larger), based on dye flow visualizations of large and small aspect ratio CVG (as shown in Figure 6.2 and discussed in Section 4.5).

- A small-scale backward-facing step, similar to that created by the retracted slat on the Boeing 737, could produce additional shock features in the flow field (as shown in Figure 6.3) and increase pressure drag, based on the initial results of the RAE 2288 comparative CFD study (discussed in Section 5.5).

- Appropriate scaling of the CVG requires at least accounting for geometric properties (length "L", width "W", and step height "H"), boundary layer properties, pressure gradient, fluid properties (density and viscosity), and flow velocity, based on previous scaling attempts neglecting specific parameters.

- Wall shear stress patterns similar to those produced during flight can be reproduced computationally (as shown in Figure 6.4), and with further refinement, could give valuable insight to flow interactions with the CVG technology, based on average wall shear stress results from the subsonic flight test scaled LES simulations with the dynamic Smagorinsky SGS model (discussed in Section 5.6).

6.2 Proposed Drag Reduction Mechanism

The drag reduction mechanism was not characterized in the work presented; however, a proposed hypothesis was developed. The unsteady shockwave visualizations obtained by Edge Aerodynamix, which suggested that the CVG had a stabilizing effect on the transonic shock as mentioned in Section 4.1.2, are the only full-scale

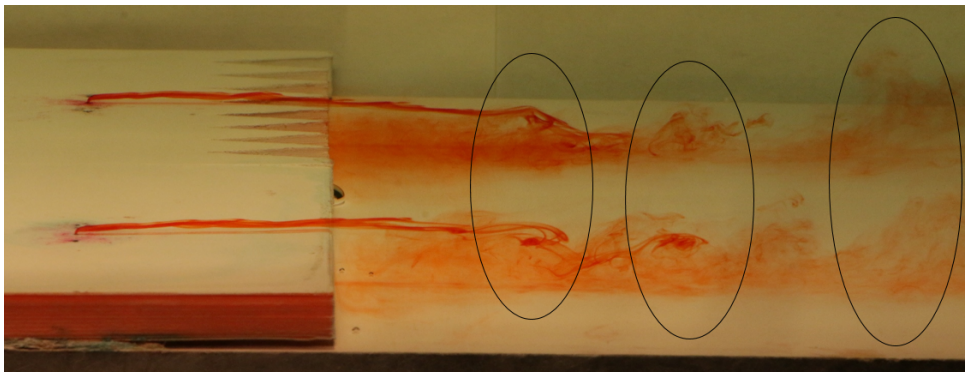

Figure 6.2: Dye test results indicated that Re_H scaled CVG behave similarly to backward-facing step.

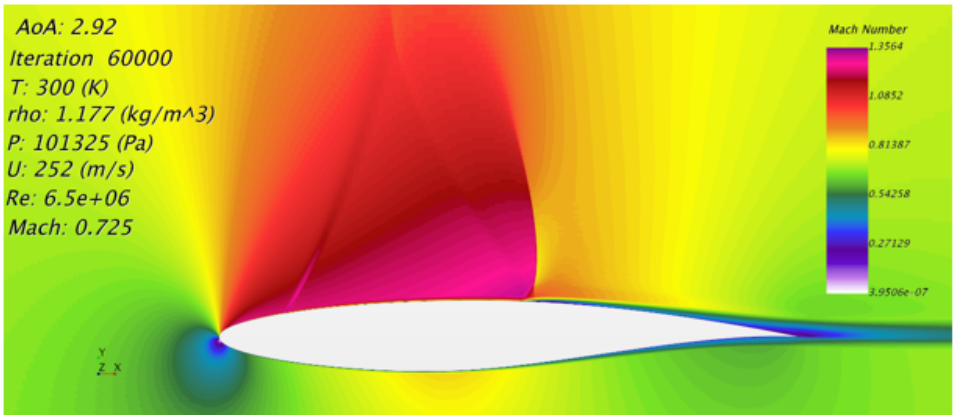

Figure 6.3: Mach profile indicated that small scale backward-facing steps in transonic flows may produce additional shock features and influence aerodynamic properties.

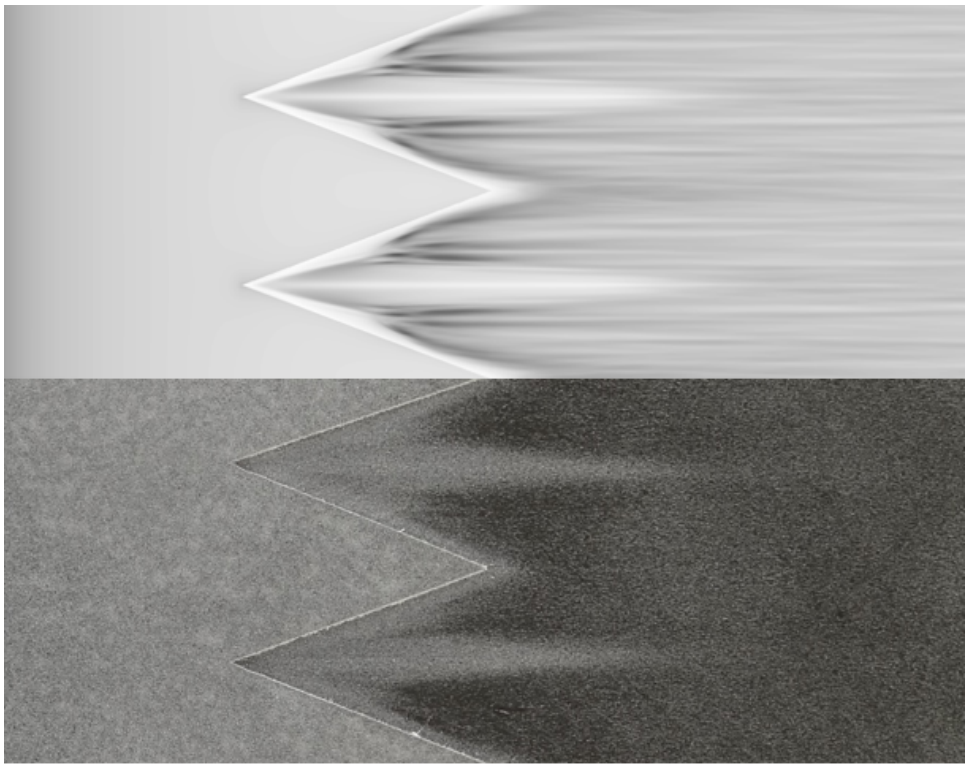

Figure 6.4: CVG wall shear stress patterns agree very well with flight test results (top is simulation result and bottom is flight test result).

flight test results available for analysis (other than fuel consumption). A qualitative study of unsteady transonic shocks found that, as the shockwave traverses toward the trailing edge, the flow remains attached much further downstream, and when the shock moves upstream, the separation region grows in size [109]. Therefore, if the CVG does stabilize the transonic shock, it could account for the fuel savings. Raghunathan and McIlwain (1990) found that passive shockwave control could reduce wake drag by as much as 10 percent, and others have seen reductions as high as 30 percent [110]. A similar study found that porous surfaces under the shockwave location reduced drag [111]. A computational investigation of unsteady shock control over the RAE 2822 airfoil found that the shock oscillations, which were self-excited and self-sustained, could be completely removed with the addition of a passive flow control channel on the airfoil surface [112]. However, most of these shockwave/boundary layer drag reduction methods found that passive shockwave interaction reduces

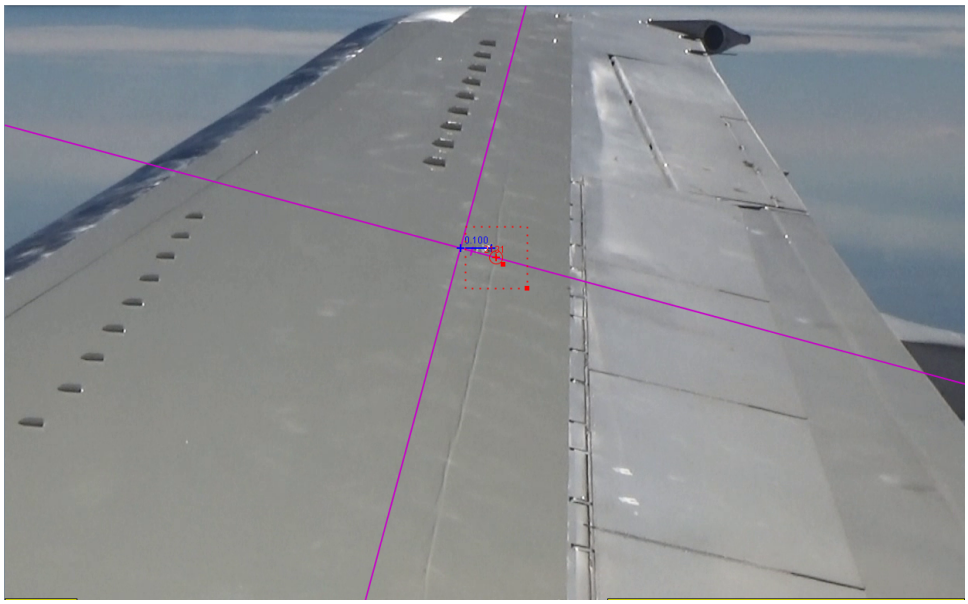

Figure 6.5: Example image from Tracker open source software, which indicates the shock location relative to a rotated coordinate system.

wake drag by producing a, y-type, two-shock feature, that results in a significant increase in viscous drag [113]. Therefore, an evaluation of the shock behavior, from the flight test visualization videos, was accomplished to either dismiss or strengthen the argument that the CVG reduces drag by influencing shockwave behavior. The visualization videos were roughly 12 minutes long (30 frames per second), one with the CVG applied to the wing and one without. Visual inspection of the videos indicated that the shock behavior was more chaotic without the CVG applied to the wing; however, visual inspection was a limited approach. Therefore, an open source video analysis software, Tracker, was used to collect quantitative data from the qualitative videos [114]. However, due to camera frame movement, shock visualization quality, and aircraft flight path adjustments, only 300 seconds of the clean wing configuration and 100 seconds of the CVG configuration were evaluated. An example image of the video processing method is shown in Figure 6.5.

The results of the shock tracking indicated that there was a high-frequency and low-frequency motion in the chord-wise direction as shown in Figure 6.6. This is consistent with Lee (2001) which noted that many studies have shown that periodic

unsteady shock behavior, which is related to flow behavior at the trailing edge that can propagate upstream and influence the shock region [115]. These results were then processed by taking a moving average over 300 samples (10 seconds) and subtracting the local moving average from the displacement, which produced the zero-moving-average (or the fluctuation from the moving average) of the data, as shown in Figure 6.7. This clearly indicates that the high-frequency shockwave oscillations are much smaller in amplitude in video taken with the CVG applied. This suggests that the CVG could be responsible for dampening the high-frequency motion of the shockwave. Larger-scale vortex generator interactions with transonic shockwaves have been previously studied and found that, for ideal shockwave/boundary layer interaction, vortex generator height compared to boundary layer height decreases as Mach increases [116]. This finding suggests that small devices, smaller than the boundary layer, can have a significant impact on the transonic shock. The downstream boundary layer vortex structures have been shown to heavily impact the unsteady nature of the transonic shockwave [117]. Therefore, it is not unreasonable that the upstream boundary layer, which develops the downstream boundary layer, could influence the shock behavior. Dolling (2001) noted that the majority of unsteady shockwave studies did not take into account the influence of the upstream incoming boundary layer and normally idealized it as 2-deminsional with a zero-pressure gradient; and therefore, the influence of the incoming boundary layer are not well known [118]. However, Wu and Martin (2008) found that high-frequency wrinkle fluctuations in the shock structure are highly correlated with the incoming boundary layer mass flux [119]. These results and the work of previous studies further strengthen the proposed drag reduction method.

If the CVG does influence the shockwave/boundary layer interaction and ultimately dampen high-frequency oscillations, it is possible that this would account for a significant drag reduction. However, it is also possible that the CVG devices drag

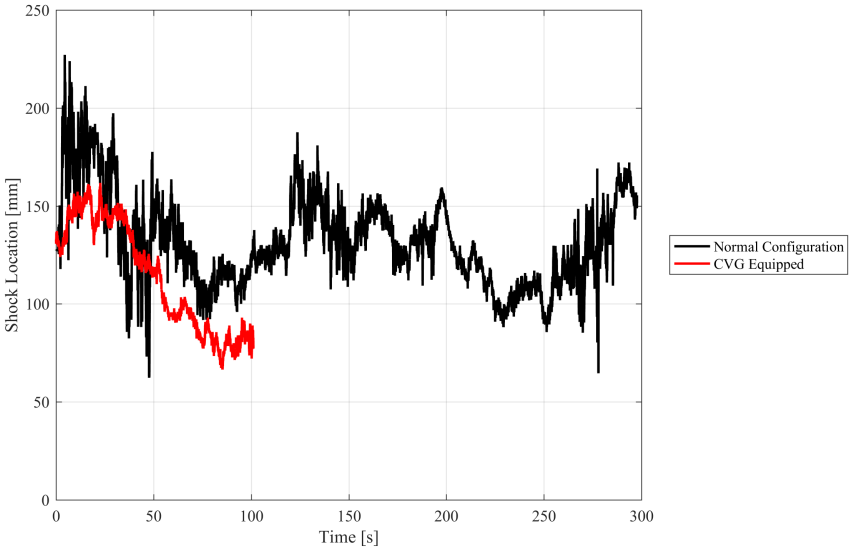

Figure 6.6: Raw shock displacement data collected from image analysis (less than 1cm of uncertainty).

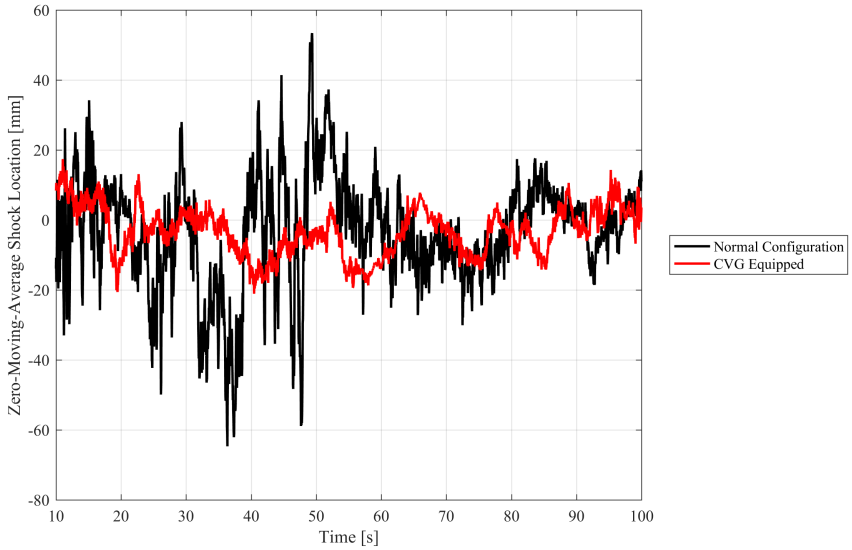

Figure 6.7: Plot of the zero-moving-average fluctuating shock displacement, which suggested that the CVG could dampen high-frequency shock oscillations.

reduction mechanism is not dependent on transonic shockwave stabilization and that the dampening of shockwave oscillations are only an additional benefit from the actual drag reduction mechanism. Furthermore, the video analysis, was heavily limited by the sample size and the unknown potential variations in the flight conditions, such as freestream turbulence. Therefore, without additional data to attempt reproduce these results it is plausible that the observed shock behaviors between the flight configurations are coincidental. As a caveat, until future studies are conducted and trends in the data are either verified or rejected, this proposed hypothesis of CVG drag reduction should be taken with caution.

6.3 Recommendations and Future Work

The author recommends continuing the projects in progress, as they will provide useful information for future work. The 2D backward-facing step simulation is capable of producing a straightforward evaluation of Star-CCM+ automated meshes as compared to structured meshes. Understanding the effect on the simulation results for any given mesh type will guide future simulation mesh or grid selection. The water tunnel validation simulations are important to relate the computational results to the experimental results and should be considered a priority. Additionally, 2D airfoil simulations, though not capturing the 3D effects of the CVG, should continue to be properly refined. Ideally, validated steady, 2D, RANS simulations would be used to specify realistic inlet boundary conditions for flow resolving simulations around the CVG geometry. Simulations of this type could be produced for all of the current flight test platform airfoils and any future CVG applications. Additionally, 2D transonic airfoil simulations should be used to further evaluate the effects of small-scale steps on transonic airfoils, even steps on the order of a CVG thickness would be of interest. However, resolving small-scale geometries for these high Reynolds number and Mach number simulations pose many difficulties. The RAE 2288 simulation is an excep-

tional baseline case with a solid validation method from the NASA CFD simulation validation resource data base. Once satisfactory comparative results are produced, studies of airfoil sections from aircraft utilizing high-lift slat devices would be of value, but the mesh or grid design from the validated RAE 2288 simulation would be a guide to producing accurate results for airfoils without available validation data. Therefore, 2D airfoil simulations should not be disregarded as less valuable, but rather as a necessary aspect of the research initiative to understand the CVG technology as a whole.

The subsonic flight scale simulation should be revised in accordance with the conclusions of Section 5.6.3. The scales associated with this simulation run the border of what is currently possible with the Oklahoma State University computational resources, Star-CCM+ commercial CFD software, and physics modeling currently in existence. Thus, extreme care should be taken when preparing this simulation. Limits on total grid element count, time step, and solution time should be considered prior to building the simulation in order to avoid unrealistic solve times. The computational times associated with the previous version should act as a guide. The results of future revisions to this simulation should be evaluated against Edge Aerodynamix's flight test results, previously obtained experimental and computational Law of the wall results, and water tunnel flow visualization.

Furthermore, the scaled experimental approaches are critical to properly evaluating and characterizing the CVG drag reduction mechanism. Therefore, the experimental investigations should be continued with hope of producing an accurate scaling law and visualizing the unique flow field associated with the CVG device. An accurate scaling law would provide much needed information about the device's relationship with the flow, ideally describing how the CVG geometry, and its flow physics, scale with the incoming flow velocity, pressure gradient, and boundary layer formation. This scaling relationship would be the foundation on which to build future transonic

tests to evaluate Mach effects. Additionally, the experimental results are the only method through which to adequately validate the CFD simulation work, which could provide a three-dimensional, time-resolved description of the entire flow field around the CVG. More plainly, the immense potential value of CFD results, which are obtained through some level of modeling (either by discretization or modeled physics) are dependent on an adequate relationship back to the (entirely physical) experimental results. Future experimental water tunnel testing of the scaling law discussed in Section 3.10.5 should be the basis on which future simulations are validated and should be a priority.

Additional experimental opportunities include scaled CVG devises applied to high-speed drone platforms produced in senior design projects. These unmanned vehicles would be ideal for quick CVG scaling evaluation, where as two similar aircraft could be studied side-by-side, one with CVG and one without and then switched. If fuel consumption data can be adequately determined to an accuracy of at least one percent, then this could be a viable experimental option. Also, wall shear stress testing would be valuable and offer a direct relationship back to the flight test results. Shear testing could be accomplished in a water tunnel with surface stress sensitive films produced by Innovative Scientific Solutions Incorporated (ISSI). The shear testing would require a new system (and investment), but would add value in producing wall shear stress patterns and comparing them to the flight tests.

Bibliography

[1] I. H. Abbott and A. E. Von Doenhoff, *Theory of Wing Sections*. Dover Publications, 1959.

[2] F. T. Lynch and M. D. Klinge, "Some practical aspects of viscouse drag reduction concepts," Tech. Rep. Technical Paper 912129, SAE, November 1991.

[3] K. F. Kuck, "A review of sand and rain erosion on helicopterrotor baldes," Tech. Rep. USAAVSCOM TM-84-D-2, United States Army Aviation Systems Command, 1984.

[4] M. S. Pepi and V. K. Champagne, "Solid particle (sand) erosion testinf of u.s. army aviation rotor blad baseline materials," Tech. Rep. ARL-TR-4313, Army Research Laboratory, November 2007.

[5] M. Pepi, R. Squillacioti, L. Pfledderer, and A. Phelps, "Solid particle erosion testing of helicopter rotor blade materials," *J Fail. Anal and Preven.*, vol. 12, pp. 96–108, 2011.

[6] P. Collins and C. Moore, "Solutions to helicopter blade erosion improving aircraft availability and reducing costs," in *European Rotocraft Forum*, no. 009, September 2014.

[7] K. Richter and E. Schulein, "Boundary-layer transition measurements on hovering helicopter rotors by infared thermography," *Experimental Fluids*, vol. 55, no. 2, pp. 21–24, 1988.

[8] M. E. Calvert and T. Wong, "Aerodynamic impacts of helicopter blades erosion coatings," in *AIAA Applied Aerodynamics Conference*, no. 2914, June 2012.

[9] Edge Aerodynamix Website, "Performance change diagram." http://www.edge.aero/copy-of-technology-diagram-4, 2017.

[10] J. Croft, "Taming turbulence with tape: Conformal vortex generators." Aviation Week and Space Technology http://aviationweek.com/commercial-aviation/taming-turbulence-tape-conformal-vortex-generators, April 2016.

[11] A. Sareen, C. A. Sapre, and M. S. Selig, "Effect of leading edge erosion on wind turbine blade performance," *Wind Energy*, vol. 17, pp. 1531–1542, July 2014.

[12] A. Sareen, C. A. Sapre, and M. S. Selig, "Effect of leading-edge protection tape on wind turbine blade performance," *Wind Engineering*, vol. 36, pp. 525–534, September 2012.

[13] P. Ireland, "Application of conformal sub boundary layer vortex generators to a foil or aero/ hydrodynamic surface," 1 2011.

[14] M. B. Bragg and G. M. Gregorek, "Experimental study of airfoil performence with vortex generators," *AIAA Journal of Aircraft*, vol. 24, May 1987.

[15] M. Van Dyke, *An Album of Fluid Motion*. The Parabolic Press, 1982.

[16] E. R. Van Driest, "On turbulent flow near a wall," *Journal of the Aeronautical Sciences*, vol. 23, no. 11, pp. 1007–1010, 1956.

[17] A. K. M. Fazle Hussain, "Coherent structures and turbulent," *Journal of Fluid Mechanics*, vol. 173, pp. 303–356, 1986.

[18] J. Jimenez, "Wall friction and the structures of near-wall turbulence," in *11th Australasian Fluid MEchanics Conference*, (Hobart, Australia), pp. 813–816, December 1992.

[19] J. C. Hunt and J. F. Morrison, "Eddy structure in turbulent boundary layers," *Eur. J. Mech. B - Fluids*, vol. 19, pp. 673–694, 2000.

[20] S. K. Robinson, "Coherent motions in the turbulent boundary layer," *Annual Review of Fluid Mechanics*, vol. 23, pp. 601–639, 1991.

[21] J. Jimenez, "Cascades in wall-bounded turbulence," *Annual Review of Fluid Mechanics*, vol. 44, pp. 27–45, 2012.

[22] S. S. Le and W. W. Willmarth, "Measurements of the structure of the reynolds stress in a turbulent boundary layer," *Journal of Fluid Mechanics*, vol. 60, no. 3, pp. 481–511, 1973.

[23] J. Lumley and P. Blossey, "Control of turbulence," *Annual Review of Fluid Mechanics*, vol. 30, pp. 311–327, 1998.

[24] O. M. Phillips, "Shear-flow turbulence," *Annual Review of Fluid Mechanics*, vol. 1, pp. 245–264, 1969.

[25] A. J. Smits and B. J. McKeon, "High reynolds number wall turbulence," *Annual Review of Fluid Mechanics*, vol. 43, pp. 353–375, 2011.

[26] S. J. Kline, W. C. Reynolds, F. A. Schraub, and P. W. Runstadler, "The structure of turbulent boundary layer," *Journal of Fluid Mechanics*, vol. 30, no. 4, pp. 741–773, 1967.

[27] H. T. Kim, "The structure of turbulent boundary layer," *Journal of Fluid Mechanics*, vol. 50, no. 1, pp. 133–160, 1971.

[28] E. R. Carino and R. S. Brodkey, "A visual investigation of the wall region in turbulent flow," *Journal of Fluid Mechanics*, vol. 37, no. 1, pp. 1–30, 1969.

[29] J. Laufer, "The structure of turbulence in fully develop pipe flow," Tech. Rep. TN-2954, National Advisory Committee for Aeronautics, 1954.

[30] C. R. Smith and S. P. Metzler, "The characteristics of low-speed streak in the near-wall region of a turbulent boundary layer," *Journal of Fluid Mechanics*, vol. 129, pp. 27–54, 1983.

[31] M. S. Chong, J. Soria, A. E. Perry, J. Chacin, B. J. Cantwell, and Y. Na, "The structures of wall-bounded shear found using dns data," *Journal of Fluid Mechanics*, vol. 357, pp. 225–247, 1998.

[32] J. H. Lee and H. J. Sung, "Very-large-scale motions in a turbulent boundary layer," *Journal of Fluid Mechanics*, vol. 673, pp. 80–120, 2011.

[33] R. J. Adrian, "Hairpin vortex organization in wall turbulence," *Physics of Fluids*, vol. 19, no. 041301, pp. 1–16, 2007.

[34] B. J. Cantwell, "Organized motion in turbulent flow," *Annual Review of Fluid Mechanics*, vol. 13, pp. 457–551, 1981.

[35] L. Kovasznay, "The turbulent boundary layer," *Annual Review of Fluid Mechanics*, vol. 2, pp. 95–112, 1970.

[36] M. R. Head and P. Bandyopadhyay, "New aspects of turbulent boundary-layer structure," *Journal of Fluid Mechanics*, vol. 107, pp. 297–338, 1981.

[37] J. Jimenez, "On the structure of near wall turbulence," *Physics of Fluids*, vol. 6, no. 2, pp. 944–953, 1994.

[38] J. M. Wallace, "The wall region in turbulent shear flow," *Journal of Fluid Mechanics*, vol. 54, no. 1, pp. 39–48, 1972.

[39] S. K. Robinson, S. J. Kline, and S. R. Spalart, "A review of quasi-coherent structures in a numerically simulated turbulent boundary layer," Tech. Rep. Technical Memorandum 102191, NASA, 1998.

[40] A. T. Conlisk, Y. G. Guezenennec, and G. S. Elliot, "Chaotic motion of an array of vortices above a flat wall," *Physics of Fluids*, vol. 1, p. 704, 1989.

[41] R. F. Blackwelder and H. Eckelmann, "Streamwise vortices associated with the bursting phenomenon," *Journal of Fluid Mechanics*, vol. 94, no. 1, pp. 577–594, 1978.

[42] J. C. S. Meng, "Engineering insightof near-wall microturbulence for drag reduction and derivation of a dsign map for seawater electromagnetic turbulence control," in *Proceedings of the International Symposium on Seawater Drag Reduction*, (Newport, Rhode Island, USA), pp. 359–367, July 1998.

[43] E. W. Adams and J. P. Johnston, "Effects of he separatng shear layer on the reattachment flow structure part 2: Reattachment length and wall shear stress," *Experiments in Fluids*, vol. 6, pp. 493–499, 1988.

[44] E. Erturk, "Numerical solutions of 2d steady incompressible flow over a backward-facing step, part i: High reynlds number solutions," *Computers and Fluids*, vol. 37, pp. 633–655, 2008.

[45] D. M. Driver, H. L. Seegmiller, and J. G. Marvin, "Time-dependent behavior of a reattaching shear layer," *AIAA Journal*, vol. 25, no. 7, pp. 914–919, 1987.

[46] J. K. Eaton and J. P. Joghston, "A review of research on subsonic turbulent flow reattachment," *AIAA Journal*, vol. 19, no. 9, pp. 1093–1100, 1981.

[47] H. Le, P. Moin, and J. Kim, "Direct numerical simulation of turbulent flow over a backward-facing step," *Journal of Fluid Mechanics*, vol. 330, pp. 349–374, 1997.

[48] F. W. Roos and J. T. Kegelman, "Control of coherent structures in reattaching laminar and turbulent shear layers," *AIAA Journal*, vol. 24, no. 12, pp. 1956–1963, 1986.

[49] S. Bhattacharjee, B. Scheelke, and T. R. Troutt, "Modification of vortex interaction in a reattaching separated flow," *AIAA Journal*, vol. 24, no. 4, pp. 623–629, 1986.

[50] A. A. Mouza, M. N. Pantzali, and S. V. Paras, "Experimental and numerical study of backward-facing step flow," in *5th National Chemical Engineering Conference*, 2005.

[51] T. P. Chiang and T. W. H. Sheu, "Vortical flow over a 3-d backward-facing step," *Numerical Heat Transfer, Part A: Applications*, vol. 31, no. 2, 1997.

[52] P. G. Spazzini, G. Luso, M. Onorato, N. Zurlo, and G. M. Di Cicca, "Unsteady behavior of back-facing step flow," *Experiments in Fluids*, vol. 30, pp. 551–561, 2001.

[53] J. Tihon, J. Legrand, and P. Legentilhomme, "Near-wall investigation of backward facing step flows," *Experiments in Fluids*, vol. 31, pp. 484–493, 2001.

[54] J. Kostas, J. Soria, and M. S. Chong, "Partical image velocimetry measurments of a backward facing step flow," *Experiments in Fluids*, vol. 33, pp. 838–853, 2002.

[55] F. Scarano, C. Benocci, and M. L. Riethmuller, "Pattern recognition analysis of the turbulent boundary flow past a backward facing step," *Physics of Fluids*, vol. 11, no. 12, pp. 3808–3818, 1999.

[56] D. J. Weber and J. E. Danberg, "Correlation of mean velocity measurments downstream of a swept backward-facing step," *AIAA Journal*, vol. 30, no. 11, pp. 2701–2706, 1992.

[57] K. Sarker, M. Ali, and Q. Islam, "A numerical study on the physics of flow over a flat plate with backward facing step," in *10th International Conference on Mechanical Engineering*, 2014.

[58] S. Jovic and D. Driver, "Reynolds number effect on the skin friction in separated flow behind a backward-facing step," *Experiments in Fluids*, vol. 18, pp. 464–467, 1995.

[59] S. Thangam and C. G. Speziale, "Turbulent flow past a backward-facing step: A critical evaluation of two-equation models," *AIAA Journal*, vol. 30, no. 5, pp. 1314–1320, 1992.

[60] A. S. Neto, D. Grand, O. Metais, and M. Lesieur, "Large-edgy simulation of the turbulent flow in the downstream region of a backward-facing step," *Physical Review Letters*, vol. 66, May 1991.

[61] B. Panjwani, I. S. Ertesvag, A. Gruber, and K. E. Rian, "Large eddy simulation of backward facing step flow," No. N-7462.

[62] J. L. Aider and A. Danet, "Large-eddy simulation study of upstream boundary conditions influence upon a backward-facing step flow," *C. R. Mecanique*, vol. 334, 2006.

[63] C. Fureby, "Large eddy simulations of rearward-facing step flow," *AIAA Journal*, vol. 37, no. 11, pp. 1401–1410, 1999.

[64] J. C. Lin, "Review of research on low-profile vortex generators to control boundary-layer separation," *Progress in Aerospace Sciences*, vol. 38, pp. 389–420, 2002.

[65] B. G. Allan, "Flow-field measurement of device-induced embedded streamwise vortex on a flat plate," in *1st AIAA Flow Control Conference*, (St. Louis, Mo), pp. 1–16, June 2002.

[66] H. Babinsky, Y. Li, and C. W. Pitt Ford, "Microramp control of supersonic oblique shock-wave/boundary-layer interactions," *AIAA Journal*, vol. 47, no. 3, pp. 668–680, 2009.

[67] B. L. Storms and C. S. Jang, "Lift enhancement of an aircraft using a gurney flap and vortex generators," *AIAA Journal of Aircraft*, vol. 31, June 1994.

[68] J. L. Aider, J. F. Beaudoin, and J. E. Wesfreid, "Drag and lift reduction of a 3d bluff-body using active vortex generators," *Experiments in Fluids*, vol. 38, pp. 485–493, 2005.

[69] J. Javier, "Turbulent flows over rough wall," *Annual Review of Fluid Mechanics*, vol. 36, pp. 173–193, 2004.

[70] G. E. Karniadakis and K. S. Choi, "Mechanisms on turbulent motions in turbulent wall flows," *Annual Review of Fluid Mechanics*, vol. 35, pp. 45–62, 2003.

[71] Y. Peet, P. Sagaut, and Y. Charron, "Turbulent drag reduction using three-dimensional structured surfaces," *Journal of Fluids Engineering*, 2010.

[72] S. Tullis and A. Pollard, "The time dependent flow over v- and u-groove riblets of different sizes," *Physics of Fluids*, vol. 6, no. 3, pp. 1310–1314, 1994.

[73] V. A. Sandborn, "Aerodynamics - control of surface shear stress fluctuations in turbulent boundary layers," Tech. Rep. CER 80-81-VAS-46, Colorado State University, 1981.

[74] D. M. Rao and S. C. Mehrotra, "Flat-plate drag measurements with vortex generators in turbulent boundary layer," Tech. Rep. CR-172125, NASA, 1983.

[75] M. J. Walsh, "Riblets as a viscous drag reduction technique," *AIAA Journal*, vol. 21, no. 4, pp. 485–486, 1983.

[76] K. J. Moore, "Drag reduction in nature," *Annual Review of Fluid Mechanics*, vol. 23, pp. 65–79, 1991.

[77] I. Tani, "Drag reduction by riblet viewed as roughness problem," *Proc. Japan Acad.*, vol. 64, no. 1755, 2014.

[78] P. K. Kundu, I. M. Cohen, and D. R. Dowling, *Fluid Mechanics*. Elsevier, fifth ed., 2012.

[79] B. R. Munson, D. F. Young, and T. H. Okiishi, *Fundamentals of Fluid Dynamics*. John Wiley and Sons, fifth ed., 2006.

[80] H. Tennekes and J. L. Lumley, *A First Course in Turbulence*. The MIT Press, 1972.

[81] L. da Vinci, "Leonardo da vinci's illistration of the swirling flow of turbulence." https://www.royalcollection.org.uk, 2004.

[82] Y. A. Cengel and J. M. Cimbala, *Fluid Mechanics*. McGraw Hill, 2006.

[83] D. Coles, "The law of the wake in the turbulent boundary layer," *Journal of Fluid Mechanics*, vol. 1, no. 2, pp. 191–226, 1956.

[84] P. S. Klebanoff, "Characteristics ot turnulence in a boundary layer with zero pressure gradient," Tech. Rep. TR-1247, National Advisory Committee for Aeronautics, 1955.

[85] P. R. Spalart, "Direct numerical simulation of a turbulent boundary layer up to $re_\theta = 1410$," Tech. Rep. TM-89407, NASA, 1986.

[86] J. Kim, P. Moi, and R. Moser, "Turbulence statistics in fully developed channel flow at low reynolds number," *Journal of Fluid Mechanics*, vol. 177, pp. 133–166, 1987.

[87] S. B. Pope, *Turbulent Flows*. University Printing House , Camvrigde CB28BS, United Kingdom: Cambridge University Press, 2015.

[88] J. Westerwee, "Fundamentals of digital particle image velocimetry," *Meas. Sci. Technol.*, vol. 8, pp. 1379–1392, 1997.

[89] M. Raffel, C. E. Willert, S. T. Wereley, and J. Kompenhans, *Partical Image Velocimetry*. Springer, second ed., 2007.

[90] B. L. Smith and D. R. Neal, *Handbook of Fluid Dynamics*, ch. 48, pp. 2–7. 6000 Broken Sound Parkway NW, Suite 300, Boca Raton, FL 33487-2742: CRC Press, 2016.

[91] F. R. Menter, "Two-equation eddy-viscosity turbulenc models for engineering applications," *AIAA Journal*, vol. 32, no. 8, pp. 1598–1605, 1994.

[92] CD-adapco, *STAR-CCM+ User Manual*, (11.06.011) ed., 2016.

[93] F. M. Denaro, "What does finite volume-based implicit filtering really resolve in large eddy simulations?," *Journal of Computational Physics*, vol. 230, pp. 3849–3883, 2011.

[94] M. L. Shur, P. R. Spalart, M. K. Strelets, and A. K. Travin, "A hybrid rans-les approach with delayed-des and wall-modelled les capabilities," *Interanational Journal of Computational Fluid Dynamics*, vol. 29, pp. 1638–1649, 2008.

[95] J. H. Ferziger and M. Peric, *Computational Methods for Fluid Dynamics*. Springer, thrid ed., 2002.

[96] C. J. Obara, "Boundary-layer flow visualization for flight testing," Tech. Rep. N88-23742, NASA, 1986.

[97] P. B. S. Lissaman, "Low-reynolds-number airfoils," *Annual Review of Fluid Mechanics*, vol. 15, pp. 223–239, 1983.

[98] G. Biswas, M. Breuer, and F. Durst, "Backward-facing step flows for various expansion ratios at low and moderate reynolds numbers," *ASME Journal of Fluids Engineering*, vol. 126, pp. 362–374, 2004.

[99] J. C. M. Lin and L. L. Pauley, "Low-reynolds-number separation on an airfoil," *AIAA Journal*, vol. 34, no. 8, pp. 1570–1577, 1996.

[100] S. Yarusevych, P. E. Sullivan, and J. G. Kawall, "On vortex shedding from an airfoil in low-reynolds-number flows," *Journal of Fluid Mechanics*, vol. 632, pp. 245–271, 2009.

[101] Oklahoma State University High Performance Computing Center, "Learn about cowboy." https://hpcc.okstate.edu/, 2017.

[102] Pointwise, "Multi-block grids for axial turbines." http://www.pointwise.com/theconnector/March-2011/Gridding-an-Axial-Turbine-Video.shtml, 2011.

[103] Y. Deubief and F. Delcayre, "On coherent-vortex identification in turbulence," *Journal of Turbulence*, vol. 1, 2000.

[104] Y. Z. Liu, W. Kang, and H. J. Sung, "Assessment of the organization of turbulent separated and reattaching flow by measuring wall pressure fluctuations," *Experiments in Fluids*, vol. 48, pp. 771–789, 2010.

[105] D. M. Driver and H. L. Seegmiller, "Features of a reattaching turbulent shear layer in a divergent channel flow," *AIAA Journal*, vol. 23, no. 2, pp. 163–171, 1985.

[106] A. Pingstone, "Transaero b737-400 planform ei-cxk arp.jpg." https://simple.wikipedia.org/wiki/Boeing737, 2008.

[107] P. H. Cook, M. C. P. Firmin, and M. A. McDonald, "Aerofoil rae 2822: Pressure distributions, and boundaray layer and wake measurements," tech. rep., Royal Aircraft Establishment, 1977.

[108] P. G. Tucker, *Advanced Computational Fluid and Aerodynamics*. 32 Avenue of the Americas, New York, NY 10013-2473, USA: Cambridge University Press, 2016.

[109] L. Jacquin, P. Molton, S. Deck, B. Maury, and D. Soulevant, "Experimental study of shock oscillation over a transonic supercritical profile," *AIAA Journal*, vol. 47, pp. 1985–1994, September 2009.

[110] S. Raghunathan and S. T. McIlwain, "Further investigations of transonic shock-wave boundary-layer interaction with passive control," *AIAA Journal of Aircraft*, vol. 27, pp. 60–65, January 1990.

[111] S. Raghunathan and D. G. Mabey, "Passive shock-wave/boundary-layer control on a wall-mounted model," *AIAA Journal*, vol. 25, pp. 275–278, February 1987.

[112] M. R. Raham, M. I. Labib, A. B. M. T. Hasan, M. S. H. Joy, T. Setoguchi, and H. D. Kim, "Control of transonic shock wave oscillation over a supercritical airfoil," *Open Journal of Fluid Dynamics*, vol. 5, pp. 302–310, 2015.

[113] R. Bur, B. Corbel, and J. Delery, "Study of passive control in a transonic shock wave/boundary-layer interaction," *AIAA Journal*, vol. 36, pp. 394–400, March 1998.

[114] D. Brown, "Tracker video analysis and modeling tool." http://physlets.org/tracker/, 2017.

[115] B. H. K. Lee, "Self-sustained shock oscillations on airfoils at transonic speeds," *Progress in Aerospace*, vol. 37, pp. 147–196, 2001.

[116] S. Lee, E. Loth, and H. Babinsky, "Normal shock boundary layer control with various vortex generator geometries," *Computers and Fluids*, vol. 49, pp. 233–246, 2011.

[117] A. Alshabu and H. Olivier, "Unsteady wave phenomena on a supercritical airfoil," *AIAA Journal*, vol. 46, pp. 2066–2073, August 2008.

[118] D. S. Dolling, "Fifty years of shock-wave/boundary-layer interaction reseach: What next?," *AIAA Journal*, vol. 39, pp. 1517–1531, August 2001.

[119] M. Wu and M. P. Martin, "Analysis of shock motion in shockwave and turbulent boundary layer interaction using direct numerical simulation data," *Journal of Fluid Mechanics*, vol. 594, pp. 71–83, 2008.

VITA

Geoffrey Kibble

Candidate for the Degree of

Master of Science

Thesis: EXPERIMENTAL AND COMPUTATIONAL INVESTIGATION OF THE CONFORMAL VORTEX GENERATOR

Major Field: Mechanical and Aerospace Engineering

Biographical:

Personal Data: Born in Tulsa, Oklahoma on May 6th, 1992

Education:

Completed the requirements for the degree of Master of Science with a major in Mechanical and Aerospace Engineering at Oklahoma State University, Stillwater, Oklahoma in August, 2017.

Received the degree of Bachelor of Science with a major in Aerospace Engineering at Oklahoma State University, Stillwater, Oklahoma, USA in May, 2015.

Received the degree of Bachelor of Science with a major in Mechanical Engineering at Oklahoma State University, Stillwater, Oklahoma, USA in May, 2015.

Presentations

Kibble, G (Submitted). "Aerodynamic Investigation and Characterization of the Conformal Vortex Generator". 2017 AIAA AVIATION Forum, Denver, CO.

Kibble, G. (Novemver, 2016). "Aerodynamic Impact of an Aft-Facing Slat-Step on High-Re Airfoils". 69^{th} APF Division of Fluid Dynamics, Portland, OR.